A PARAMETRIC EVALUTION OF CARBON NANOTUBE SYNTHESIS FROM ALUMINA PARTICLES

A Thesis

presented to

the Faculty of the Graduate School

at the University of Missouri-Columbia

In Partial Fulfillment

of the Requirements for the Degree

Master of Science

---

by

JIN LI

Dr. Matthew Maschmann, Thesis Supervisor

MAY 2015

The undersigned, appointed by the dean of the Graduate School, have examined the thesis entitled

A Parametric Evaluation of Carbon Nanotube Synthesis from Alumina Particles

Presented by Jin Li,

a candidate for the degree of Master of Science,

and hereby certify that, in their opinion, it is worthy of acceptance.

_____

Professor Matthew Maschmann

_____

Professor Jian Lin

_____

Professor Tommi A. White

ACKNOWLEDGEMENT

Foremost, I would like to express my sincere gratitude to my advisor and committee chair, Dr. Matthew Maschmann, who shared with me a lot of his expertise and insights during our research. Throughout this period, he provided lots of good ideas and sound advice, which is of tremendous help and encouragement to me. Without his guidance and persistent help this thesis would not have been possible.

I would also sincerely thank Professor Jian Lin and Professor Tommi A. White for serving on my committee and for their time and efforts to help me in innumerable ways.

I would also like to use this chance to thank Dr.Tommi A. White and Thomas Lam from EMC, and Cherian J. Mathai Cherian from Center for Nano/Micro Systems and Nanotechnology, Dr. Hao Li and Qingsong Yu from MAE department for their great help and caring they provided.

Finally, I extend the warmest thanks and appreciation to my parents who have always supported me in my endeavors, Miss Jie Tang who always given me encouragement and good advice to follow my dreams and Miss Haixin Shao who gives me love in last 4 years. You are my source of strength and spirit of belonging the shoulder I am standing on.

Table of Contents

LIST OF FIGURES

LIST OF TABLES

ABSTRACT

Carbon nanotubes (CNTs) are a new material which was first discovered in 1991, and they have generate huge activities in most science and engineering areas due to their unprecedented electrical, thermal, and mechanical properties. These properties make CNTs ideal, not only for a wide range of applications but also as a test bed for fundamental science.

Alumina particles are used as supports for CNTs. CNTs are synthesized by floating catalyst chemical vapor deposition (FCCVD). Two different sizes of alumina particles are used as support, and 4 different surface application are employed with each size of alumina. Each of the 8 different alumina-CNTs sample configurations were subjected to multiple analysis techniques to characterize the CNT yield with respect to CNT morphology, density, morphology, and diameter distribution. The techniques used include scanning electron microscopy (SEM), transmission electron microscopy (TEM), thermo gravimetric analysis (TGA) and Raman spectroscopy.

The CNTs are also used as strain sensors and oil capture devices. The alumina-CNTs demonstrate excellent linearity, stability, and fast piezoresistive response to uniaxial strain. Similar alumina-CNT structures may have potential in flexible electronics and distributed sensing networks. The alumina-CNTs also demonstrate the ability to scavenge approximately 50x their own mass in oil while floating on a water surface. The oil content is burned, and the alumina-CNT material may be reused. These applications demonstrate the potential for the adoption of high-volume CNT growth from powder substrat.

Chapter 1-Introduction

1.1 Introduction

Since their first discovery in 1991[1], carbon nanotubes (CNTs) have generated significant interest in many science and engineering areas due to their unprecedented electrical, thermal, and mechanical properties. There is no previous material which has displayed the combination of superlative mechanical, thermal and electronic properties attributed to them, such as the elastic modulus measured for individual MWNTs is reaching a high number of 1 TPa and a tensile strength of 100 GPa [2]; and also MWNTs can carry currents of up to 10^9 A/cm^{-2} [3] with an effective nanotube thermal conductivity of 2×10^2 W/m K along the tube axis [3]. These properties make CNTs candidates for a wide range of applications and a test bed for fundamental science. There are two main categories of CNTs. One is single-walled nanotubes (SWNTs), which consist of a single sheet of graphene rolled seamlessly to form a cylinder with diameter of order of 1 nm and length of up to centimeters [4]. Multi-walled nanotubes (MWNTs) consisting of two or more concentric cylinders separated by a lattice spacing of 0.35 nm, similar to the basal plane separation in 3-D graphite. MWNTs normally have diameters from 2 to 100 nm. During the last several decades, CNTs have been among the most researched areas in material science. These molecular-scale carbon tubes are the strongest material known with remarkable electronic properties, and potential application in medicine [5], energy storage [6], biotechnology [7] and a wide range of other fields [7].

1.11 Carbon Nanotube Structure

Carbon nanotubes have a cylindrical structure consisting of one or more graphene sheets. Figure 1.1 shows a schematic representation of how both SWCNTs and MWCNTs may be represented as joined graphene sheets, though the figure does not represent the synthesis process of CNTs.

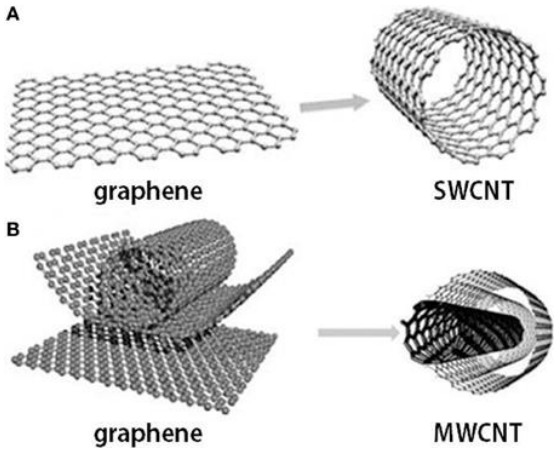

Fig. 1.1 SWCNT and MWCNT structure [8]

The structure of a SWCNT may be mapped to a graphene sheet based on its chiral vector, C, which joins two atomic positions on a graphene sheet.

$$\vec{C} = n\vec{a} + m\vec{b}$$

Here, *a* and *b* represent the lattice vectors of graphene lattice and *n* and *m* represent the integer multiples of each lattice vector that define the perimeter of a CNT, where and $n \geq m$. The tubular structure is produced by rolling up the graphene sheet in the direction of the chiral vector and connecting the atomic sites specified by the chiral vector. Note that the length of the chiral vector represents the perimeter of the SWNT formed by the rolling process.

A coordinate (n, m) is used to identify the chiral index each CNT. Each pair of integers represents a possible CNT tube structure. Figure 1.2 shows graphene layers with atoms labelled using (n, m) coordinate and 2-D lattice unit vectors.

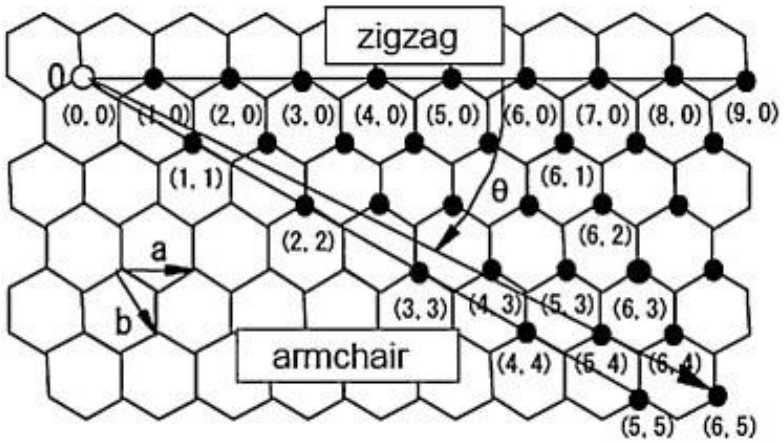

Fig. 1.2 A graphene lattice may be used to represent the chirality of SWNTs using the chiral indices (n, m). Here, n and m represent integer multiples of the 2-D graphene lattice unit vectors shown [8].

Within this, SWCNTs may be classified into three types in terms of symmetry along the axis as shown in Figure 1.3 The first type is (n, n) CNTs, as also called armchair CNTs, where the sp^2 bonding (C-C bonding) perpendicular to the tube axis have an armchair shape as shown. The second type SWCNT is (n, 0) CNT, named as zigzag CNTs for the carbon–carbon bonding perpendicular to the tube axis have a zigzag shape. The third type of SWCNT it is known as a chiral CNT, as they are neither an armchair shape CNT nor zigzag CNT.

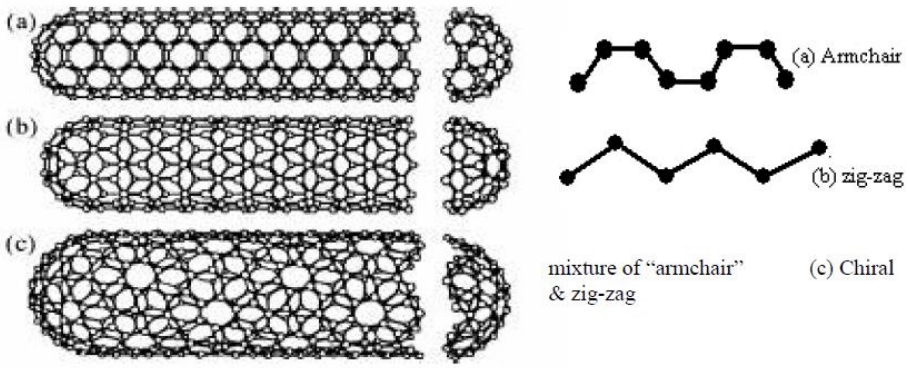

Fig. 1.3 Drawing of (a) (n, n) armchair CNTs, (b) (n, 0) zigzag CNTs, and (c) (n, m) chiral CNTs.[8]

1.12 Electrical Properties

The unique electrical properties of carbon nanotubes are one of advantages which attract the most exciting and widely studied interest. One intriguing feature of CNTs is that the small diameter that makes possible interesting quantum effects, electronic and magnetic properties. Depending on their chirality and SWNT tube diameter, nanotubes could be either semi-conducting or metallic materials. When the difference in the chiral indices of n-m is a multiple of three, the CNT is metallic; when the difference n-m is not a multiple of three, the CNT is a semiconductor. Therefore, two-thirds of SWNTs are semiconducting, while one-third are metallic. Metallic tubes may be used for electrical interconnects [9] or as electron tunneling transistors [10]; while semi-conductors are used to produce diodes [11], p-n junctions [12], and field-effect transistors (FETs) [13]. For semi-conducting CNTs, its band gap is inversely proportional to the diameter and ranges from 0 to 1eV [14]. SWCNT FETs have demonstrated ballistic electronic transport at room temperature and are IBM expects to utilize SWCNT FET technology by the year 2020 [15].

1.13 Mechanical Properties

The excellent mechanical properties are an additional motivator that CNTs become the most exciting and interesting nanosize material in research. As a tubular structure rolled up by graphene sheet, the sp^2-bounding(C-C bonds) presents exceptional strength against any distortion or torsion no matter in direction in-plane or out of the plane [16]. This property enables CNT could be used as highly elastic and high strength material.

Experimental measurement of the mechanical properties of individual carbon nanotubes such as Young's modulus and tensile strength is quite challenging due to their extremely small dimensions. The first CNTs Young's modulus experimental data was obtained by isolating a carbon nanotube and measuring the amplitude of its intrinsic thermal vibration in a transmission electron microscope (TEM) [17]. At the free ends of carbon nanotubes, the thermal vibration was a function of temperature and Young's modulus. The nanotube is assumed behaving as a straight cantilever rod with one end fixed and the other vibrating. By this experimental measurement, an average Young's Modulus value of 1.8TPa was obtained.

Because a diameter difference exist between every chiral vector of SWNTs, the mechanical properties of CNTs would also be differently. For small diameter CNTs, such as SWCNT or double-walled carbon nanotubes (DWCNTs), mechanical properties may be calculated approximately by treating these CNTs as a straight rod or thin rod. However for multi-walled carbon nanotubes (MWCNTs), the influence of diameter cannot be ignored, shell theory must be employed. Using "tight-binding" molecular dynamic methods, total

energy calculation combining with measurements resulted in accurate estimation of the modulus of elasticity. Normally, this estimation will give a result in range of 1TPa and 5 to 10% tensile strain before failure [18].

Table 1.1 provides approximate mechanical properties for different materials. Although the values of Young's modulus and tensile strength may be different if tested by different experiment, from these approximate values we still could comparison the properties between these carbon and steel.

Table 1.1 Mechanical Properties of Different Materials [19]

Material	Young's Modulus (GPa)	Tensile Strength (GPa)	Density (10^3kg/m3)
MWCNT	1,200	150	2.6
SWCNT	1,054	75	1.3
SWCNT Bundle	563	150	1.3
Graphite (in-plane)	350	2.5	2.6
Steel	208	0.4	7.8

Individual carbon nanotubes (CNTs) have been long well known to have exceptional mechanical, electronic, photonic, and optical properties, which could provide important applications for both nanoscale devices and macroscopic applications. For macroscopic applications there is a need to assemble these CNTs into yarns and sheets at commercially acceptable costs, while minimizing the properties degradation in going from individual CNT characteristics to those of the yarns and sheets. The production of large populations of aligned CNTs creates a continuous film, often called CNT forests. CNT forests (also called CNT carpets) superficially resemble bamboo forests, except that the CNT ‘‘trees’’ in these forests can be over 50,000 times longer than their diameter, and this very high aspect ratio is useful for optimizing properties[20].

Comparing with a single CNT, CNT forests have a reduced stiffness. Normally a CNT yarn spun from a CNT forests has a diameter of 5-10 μm, when tasted in a tow, or bundle, of 6000 filaments, it has a tensile strength of 5.67 GPa and a tensile modulus of 0.276 TPa [21]. However when SWCNT is tested, it has a tensile strength of 13-53 GPa and a tensile modulus of 1-5 TPa [22-24]. SWCNT has a higher strength to weight ratio in the axial direction comparing with carbon fibers, which is up to four times greater [25].

Mechanical properties of CNT forests depend on the CNT length, diameter and surface density. Currently the process of nanoindentation is being explored as a means of determining the mechanical properties of vertically aligned carbon nanotube (VACNT) forests. Under indentation, each CNT can be modeled as a cantilevered beam subjected to deflection from the indenter tip. The resistance to indentation is the result of the cumulative bending of the VACNTs. In the indentation test, a hard tip is pressed into the sample with

a known load for a short time. Hardness for nanoindentation is defined as the ratio of maximum load to the residual indentation area. Using beam theory, the effective bending stiffness is determined by fitting the mechanical model to the indentation force-penetration curves. Nanoindentation provides a method to characterize the mechanical properties of CNT forests. Typical modulus values of CNT forests range from 0.9TPa to a value of 5TPa [23].

1.2 Introduction to Chemical Vapor Deposition

The controlled synthesis of CNTs with a large scale and high quality is the basis for further investigation. It is well known that arc-discharge [26], laser ablation [27], and chemical vapor deposition (CVD)[28] are the three major methods for the synthesis of CNTs. CVD is currently the most popular method of synthesis CNTs. In this process, thermal decomposition of a hydrocarbon vapor is achieved in the presence of a metal catalyst. Hence, it is also known as thermal CVD or catalytic CVD. For different purposes, many kinds of CVD have been explored, such as floating catalyst CVD (FCCVD) [29], water assisted CVD [30], oxygen assisted CVD [31], hot-filament CVD (HFCVD) [32], microwave plasma CVD (MPECVD)[33], radiofrequency CVD (RF-CVD) [34] and etc. Figure 1.3 gives most of current methods for synthesizing carbon nanotubes.

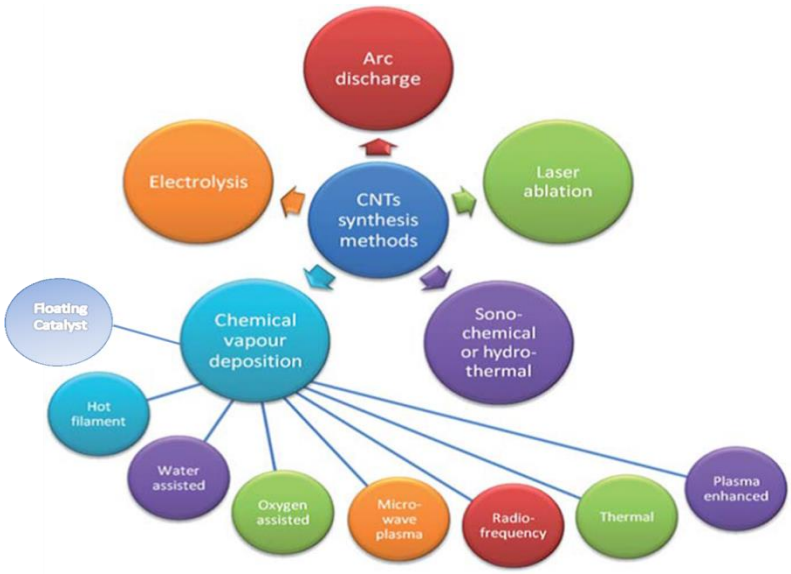

Fig.1.4 Current methods of synthesis carbon nanotubes [28]

Traditional CVD method of synthesizing CNTs include a tube furnace reactor in which a hydrocarbon gas is flowed into a heated tube, Catalyst material (typically a transition metal such as Fe, Co, Mo or Ni) is typically deposited on a growth substrate such as silicon and set in the center of the processing tube. The hydrocarbon gas decomposes, and carbon from the hydrocarbon gas diffuses into the catalyst particles at sufficiently high temperature (600—1200℃). CNTs grow on the catalyst in the reactor, and are collected when the system is cooled down to room temperature. Figure 1.4 shows a schematic diagram of the experimental set-up used for synthesizing CNTs by CVD method in its simplest form.

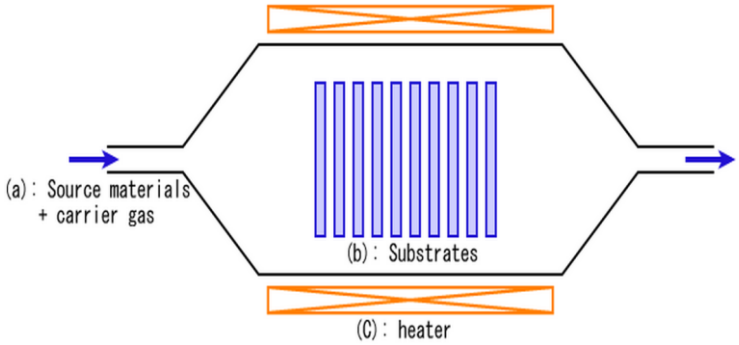

Fig. 1.5 Schematic of experimental set-up for synthesizing CNTs by CVD [28]

Comparing to other synthesis methods, CVD is a simple and economic technique for synthesizing CNTs at low temperature and ambient pressure. Although arc- and laser-grown CNTs have a better crystallinity comparing to the CVD-grown CNTs, CVD offers a better yield and lower cost. And, when it comes to structure control or CNT architecture, CVD may be the only answer. What is more, CVD is versatile. The hydrocarbons used in CVD could originate from diverse sources (solid, liquid or gas), and it is compatible with numerous substrates. The wide parameter space afforded by CVD allows CNT growth in a variety of forms, such as powder, thin or thick films, aligned or entangled, straight or coiled nanotubes, or a desired architecture of nanotubes on predefined sites of a patterned substrate.

1.21 Carbon Nanotubes Growth Mechanism

Although it is already more than 20 years from their first discovery, the mechanism of CNTs growth is still an active area of research [35]. Several research groups have proposed several possibilities based on the reaction conditions and post deposition product analyses; however, they are often contradicting. Nevertheless, one of CNT growth

mechanism has been widely-accepted which is generally outlined as follows [35]. Hydrocarbon vapor will firstly decomposed into carbon and hydrogen species when in contact with the "hot" metal nanoparticles; hydrogen gas is carried downstream and carbon gets dissolved into the metal. The dissolved carbon will crystallize in the form of a cylindrical graphene lattice after reaching the carbon-solubility limit in the metal at that temperature, having no dangling bonds and hence energetically stable.

There are two general growth mechanism observed experimentally. When metal has an acute contact angle with the substrate, the catalyst–substrate interaction is weak, hydrocarbon decomposes on the top surface of the metal, while carbon diffuses down through the metal. A CNT precipitates out across the metal bottom, pushing the metal particle off the substrate. The CNT continues to grow longer and longer if the catalyst remains catalytically active. Once the metal is fully covered with excess carbon, its catalytic activity ceases and the CNT growth will stop. This is known as "tip-growth model [36]." Figure 1.5 (a) shows four steps of this progress.

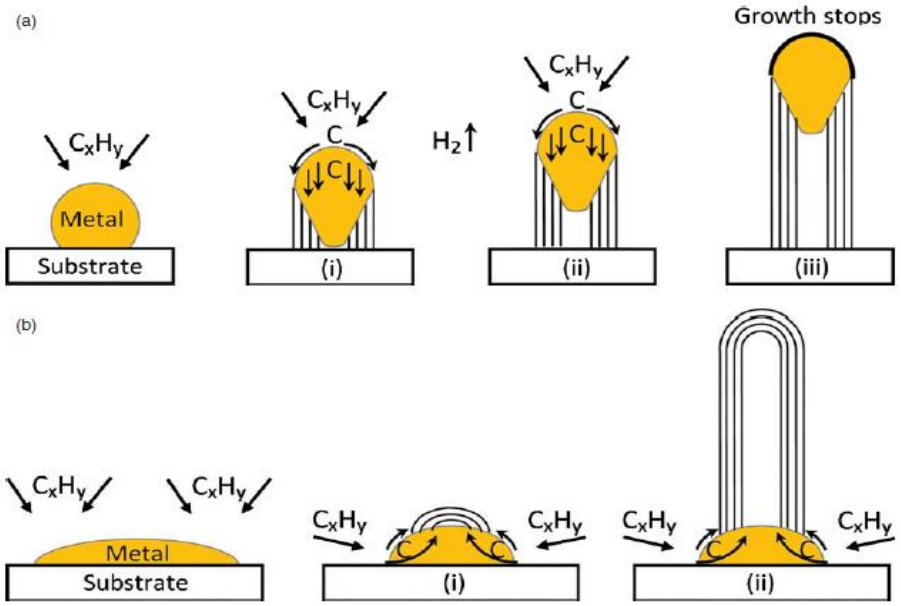

Fig 1.6 Widely-accepted growth mechanisms of CNTs: (a) tip-growth model, (b) base-growth model [36]

In the other case, (Fig. 1.5 (b)) on the contrary to tip-growth case, metal has an obtuse contact angle with the substrate and the catalyst–substrate interaction is strong. The initial hydrocarbon decomposition and carbon diffusion takes place similar to that in the tip-growth case, but the CNT precipitation fails to push the metal particle from the growth substrate. Thus the CNT grows up with the catalyst particle rooted on its base; hence, this is known as "base-growth model."

1.3 Carbon Nanotube Sensors

The development of new micro scale materials appropriate for distributed sensing and measurement is an important and growing topic engineering research. The small size and unique properties of carbon nanotubes provide valuable attributes amenable to broad

sensing applications. For example, the stiffness and nanoscale diameter of CNTs make them ideal tips for atomic force microscopy (AFM). This potential is first recognized by Smalley and his colleagues [37], and improved by Lieber group [38]. Following these pioneering studies, notable progress has been made in the production of nanotube AFM tips. After that many impressive images have been obtained due to these probes [39]. Interest in using CNT as gas sensing has also grown steadily since the pioneering studies done by Zettle and Dai group since 2000 [40]. The very large surface area to volume of CNTs are exploited in these sensors. In addition, functionalization and doping with catalysts, CNTs could be functionalized with chemical agents to sense a diverse range of gases. Nanotube-based sensors can operate at room temperature, where as conventional solid state sensors, which normally work begin at 400℃ [41].

Using of CNTs in biosensors has also attracted much interest as application in gas sensing. Significant research has been done on micro scale electrochemical biosensors employing nanotube electrodes. These sensors offer significant advantages over traditional electrodes [42]. These kinds of sensors often offer a superior minimum detection limit and a very small detection time. Lots of these sensor are already available in commercial market is also another prove that these CNTs-based sensors would gather more attention both from research and application.

1.31 Gas Sensors

Gas sensing is one area where CNT properties may be uniquely exploited. Due to their extremely high surface-to-volume ratio and hollow structure, CNTs are an ideal material for gas molecules adsorption and storage. CNTs electronic properties have been

demonstrate that it is sensitive to the exposed environment due to gas molecule adsorption. Several research groups have used SWCNTs to sense NH_3 [43], after functionalized tubes with poly (ethylene imine) [43] and connected to titanium and/or gold pads. It was found that functionalized SWCNTs experienced a much greater change of resistance upon exposure to NO_2 than other tubes, equipping CNTs greater sensitivity as sensor. This was attributed to electron transfer between the attached molecules and the valence band of semiconducting SWCNT [44]. It was also used to sense NO_2 by functionalized SWCNT [45]. Figure 1.7 shows these fast response and high sensitivity and selectivity progress [46].

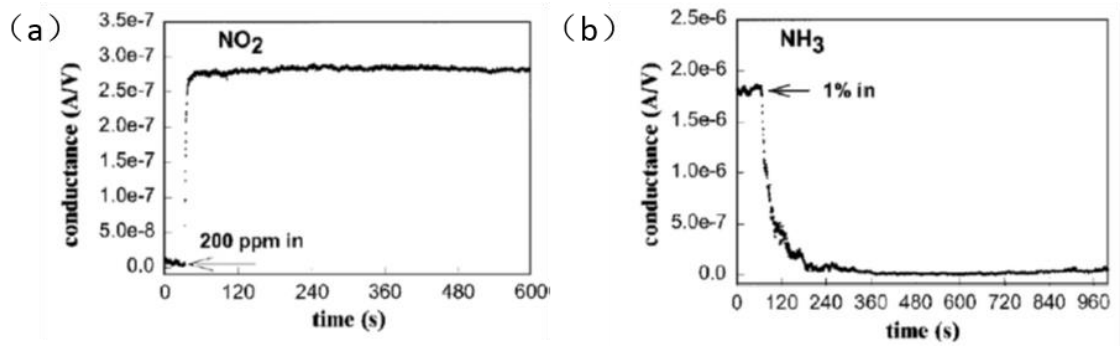

Fig 1.7 Electrical response of a semiconducting SWNT to gas molecules. Conductance (under Vg = +4 V) versus time in a 200-ppm NO2 flow (a). Conductance (under Vg = 0 V) versus time recorded with the same S-SWNT sample in a flow of Ar containing 1% NH3 (b) [43].

1.32 Biosensors

CNTs have already been used to sensing many biological markers. CNTs' fast response, high sensitivity, and relatively simple fabrication combined with the small size, economy, stability, could provide a cost-effective point-of-care testing tool and a new method for high-throughput screening, especially the SWCNT. CNTs may serve as attractive electrode materials, utilizing their high surface areas and conductivities. Lots of

studies are now using CNT-containing electrodes, and in many cases, CNTs electrodes displayed characteristics that are equal or superior to that of conventional electrodes [47]. Various methods have been used to make these kind electrodes such as simply mixing the nanotubes with a binder [48], or coating onto a glassy carbon electrode [49] to replace or complement existing electro materials such as glassy carbon [50] or precious metals [51]. It is reported that the real-time detection of single viruses, small molecules, and proteins is possible with biosensors that use carbon nanotube transistors as the active transducer.

1.33 Physical Sensors

CNTs are also considered to measure physical phenomena such as pressure and flow rate as "nanobalances" for its unique electronic and mechanical properties. Ultra-long CNT blocks could act as pressure or strain sensors. Functionalize these vertically aligned CNTs as freestanding films, it was proved that the feedback signal is strongly dependent on the stress or stain applied to nanotubes, and these kind sensors exhibit reversible electrical conductivities and a compressive strain response. Using CNTs as flow sensors would be possible only if electricity could be generated by passing a liquid over CNTs, this idea is first put forward by Král, Petr, and Moshe Shapiro [52]. Their calculation suggests that nanotube would induce an electron flow along the walls of tubes in the same direction as the liquid flow when the liquid is a polar liquid as water or NH_3. This effect is announced to be experimentally demonstrated by Ajay Sood of Indian Institute of science in Bangalore [53].

CNT forests or vertical aligned CNT (VACNT) are also used for physical sensing especially in flow sensing or force sensing. Inspired by the diversity of hair sensors utilized

by natural organisms, multiple artificial hair sensor (AHS) designs have been developed and lots of materials are used in AHS (also known as force sensitivity resistors (FSRs)) such as carbon black-loaded polyurethane [54], doped silicon strain gauges [55, 56], and a carbon nanotube (CNT)-loaded PDMS [57]. CNT forests, due to its low mass density and high sensitivity to compressive loading become an attractive mechano-electric sensing element for small unmanned air vehicles (SUVAs) application [58]. In 2012, Maschmann and Ehlert [58] reported the use of CNT array-coated glass microfiber as AHS device (Figure 1.7). In their experiment, three CNT arrays of various height were subjected to multiple compression tests, including quasi-static, dynamic, and creep tests. The CNT arrays exhibited a nonlinear resistance response to compressive loading, with maximum sensitivity between approximately 0.1–0.4 kPa [58]. A rapid response time on the order of 10ms is observed for each of the arrays. These preliminary electromechanical results demonstrate the high sensitivity, repeatability, and rapid response time of CNT arrays, and indicate that CNT arrays may be a viable transducer for airflow sensitive AHS devices.

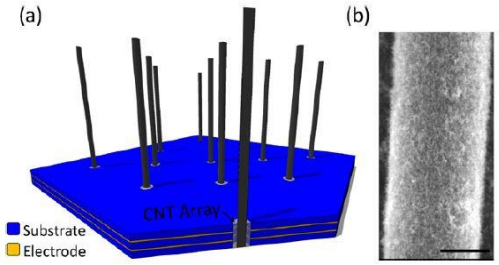

Fig 1.8 (a) Notional schematic of proposed artificial hair sensor array with CNT array electromechanical transduction element. (b) SEM micrograph of a CNT-coated carbon fiber synthesized using the same CNT growth parameters as used for the planar silicon substrates represented in this work. Scale bar = 5μm[58].

Other interesting applications of CNTs are also been reported. In 2010, Takeo Yamada [59] and his group introduced a stretchable carbon nanotube strain sensor for

human-motion detection. Basing on the high deformability of SWCNT films results from its fiber structure and other SWCNT properties, this kind human motion detection has realized a novel strain sensor that can measure and withstand strain up to 280%, with high durability (10,000 cycles at 150% strain), fast response (delay time, 14 ms) and low creep (3.0% at 100% strain) [59]. These important features allow the material to be used to precisely monitor large-scale and rapid human motion, as was demonstrated by embedding various strain sensors into clothing worn over the skin then using it to detect movement, typing, breathing and phonation (speech). Basing on thin film CNT networks sensitive to pH and its conductive, transparent and flexible backbone structure, a new CNT network pH sensor is reported by K. Martti [60] and tested. This kind CNT based pH sensor allows a determination of pH values ranging from pH 1 to 13 by its excellent performance in terms of linearity, selectivity, stability and fast response. The easy method of preparation, in addition to a clever design and the great potential of various polymers for many applications, open up a wide range of CNTs sensor applications and offer enormous potential in the upcoming field of plastic electronics.

1.4 Synthesis Carbon Nanotubes on Powders

To promote the production and purity of CNTs, high amount of work have been done to understand the role of supports in CNTs growth. Previous work is highly concentrated on understand the role of catalyst metal particles or their compounds uniformly dispersed on some special supports. Today, significant research is centered on the role of CNT catalyst supports. As has been proved, the support plays an important role of influencing the activity of catalyst. The previously reported supports have included

$CaCO_3$ [61], Al_2O_3 [62], MgO [63,64], SiO_2[65,66], CNTs [67], zeolite [68], mesoporous molecular sieves[69] and minerals[70]. The interaction between the supports and catalyst metal affects the aggregation tendency of catalyst particles at elevated growth temperature, and also, this aggregation tendency could be used and adjusted to prepare CNTs with a uniform diameter [71].

The results of CNTs growth with the same catalyst but on different types of supports suggest that substrates with larger surface areas, such as alumina and silica, will promote CNT nucleation and growth, high surface area allows the carbon source atoms to diffuse readily to the metal catalyst particles. However, maximizing the surface area is not the only reason for using nanoparticles as heterogeneous catalysts. The role of the supports include: (a) to disperse the active phase, (b) to prevent sintering of catalyst, and (c) to improve mechanical strength.

To understand the mechanism of the formation of nanotubes and the role of the catalyst support with the relation of the state of the metal in the CCVD production of MWNT, K. Hernedi [72] tested a great variety of catalyst supports (silica gel, zeotype materials, alumina, etc.) with different pore diameter and proved that both Co- and Fe-containing samples are good catalysts in the generation of MWNT from acetylene via CCVD and only those catalyst particles who deposited on the external surfaces of porous support could take part in the catalytic carbon nanotube formation.

Calcium carbonate ($CaCO_3$) was firstly reported as a novel catalyst support for the synthesis of MWCNTs in 2003 by K. Hernedi [72] also, where the conventional $CaCO_3$ was impregnated with metallic salts using ammonia to keep a constant pH-value. In their

experiment, using $CaCO_3$ results in an efficient selective formation of CNTs in catalytic growth and enables simple one-step purification without perceivable damage of the CNT structure , they also shows the large-scale production (100 g/day) of MWCNTs is possible by using $CaCO_3$ support in a rotary-tube oven. To improve the average carbon yield of CNTs growth on $CaCO_3$, Jipeng Cheng from Zhejiang University [73] change the conventional $CaCO_3$ to nanocrystalline $CaCO_3$, and found that the smaller size of the $CaCO_3$ support led to a much higher yield of CNTs than previously reported by K. Hernedi. In their experiment, they also proved that among all the catalysts supported on nano-$CaCO_3$, Fe-Co/$CaCO_3$ catalyst is the most active one, and growth temperature can affect the activity of catalytic metals and the disintegration of $CaCO_3$ support. The purification can be performed in one step, reaching as high as 95 wt% without any structural destructivity. These results open the door for formation of CNT-based composites and raise hope for a large-scale and low-cost synthesis of CNTs suitable for industrial application.

Alumina micro particles are also selected as supports for CNT synthesis, which is first reported in 1999 by Alan M. Cassell [74]. They found that alumina is a superior catalyst support material over silica partly due to stronger metal-support interactions on the alumina. In their experiment, a novel Al_2O_3-SiO_2 hybrid support material is synthesized by sol-gel to further increase the yield of SWNTs. The alumina phase in the hybrid support retains its chemical characteristics without being fully covered by the silica phase. The highest yield of SWNTs was achieved with a Fe/Mo bimetallic catalyst supported on the new type of Al_2O_3-SiO_2 hybrid material. They found that, in the CVD growth of nanotubes, the active metal catalytic species, metal-support interactions, resistance of the catalyst to

sintering and the chemical, and physical nature of the support dictate the yield, purity, and quality of the nanotubes [75].

Micrometric alumina particles has been used by Delong He [76] and his group to support MWCNTs growth. The hybrid structures are obtained by in situ grafting carbon nanotubes (CNTs) on spherical Al_2O_3 particles using an easy chemical vapor deposition method, without any pre-patterned catalyst treatment. The CNT organization, which is strongly dependent on the diameter, length, and area number density yields to three distinct architectures: "short-dense-homogeneous", "six-branch" and "urchin-like" [76]. In their program the influence of specific characteristics of Al_2O_3 on hybrid structures is also discussed. No more work is found focus on the fundamental mechanism of alumina particles as a support in CNTs growth

1.5 Motivation of This Work

This work focuses on understanding the mechanism of CNTs grown on readily-available alumina powders a for high volume CNT growth. The application of the powder onto substrates was performed by numerous means to vary the particle density on a silicon support. Parametric variations between application technique and particle sizes were examined to determine their influence on the overall CNT yield. CNTs were synthesized on commercially available alumina powders of different nominal particle sizes (50 nm and 10 μm). Because the alumina particles offer a significant surface area from which CNT

growth could initiate, these alumina powders could provide a means for high-volume and inexpensive production of loose CNT powder materials. To demonstrate the application of the CNT products, the material is tested as a strain sensing material and as an oil absorbent.

Chapter 2 Experiment and Procedure

2.1 Sample preparation

2.11 Carbon Nanotube Forest Support Substrate

As previously stated, many materials may be used as a support substrate for synthesizing CNTs. Typical materials include planar crystalline substrates, particularly silicon, structural microfibers (such as glass and carbon microfibers), and powders to a much lesser extent. The composition of the substrate determines many aspects of carbon nanotube growth. In particular, the interactions between the catalyst particle and substrate surface energy determine the catalyst particle size and density [77]. For example, the use of alumina as a thin buffer layer on silicon substrate has been studied extensive and has been shown to produce a greater areal density of CNTs of smaller diameter than silicon dioxide. Many oxide materials are compatible with CNT synthesis, including included $CaCO_3$ [61], Al_2O_3 [62], MgO [63,64], SiO_2[65,66], CNTs [67], zeolite [68], mesoporous molecular sieves[69] and minerals[70]. While most substrates are rigid and composed of a regular geometry, powder materials offer a very large surface area to volume ratio and may be used to produce freeform CNT forests in bulk. Further, powder materials are readily available, reasonably inexpensive, and are compatible with ceramics processing techniques.

Many ceramics powders could be used as catalyst support. This study utilizes different nominal grain sizes of alumina powder. To perform a parametric study, two size of powder are chosen 50 nm and 10 μm. The 50 nm alumina powder is a commercial product of Buehler. The nominally 10 μm alumina powder is from Aldrich Chemical Company, Inc, and has a purity of 99.8%.

To provide a rigid support for the powder materials, polished silicon prime wafers with a native oxide were employed. While thermally oxidized silicon wafers support CNT synthesis on the oxidized surface, a native oxide film will not support CNT growth. The silicon was prepared by dicing a 4 inch diameter wafer into strips that were approximately 2 x 2.5 cm in length. The rigidity and planarity of silicon wafer allowed for simple powder surface preparation. Further, the polished surface of silicon allows for easy removal of CNTs from the substrate.

2.12 Procedure of Sample preparation

Multiple techniques were used to deposit powders on silicon wafers for CNT growth. Techniques included dry application of powder, masked tape casting, dip coating, and spin coating of alumina powder solutions. These application techniques deposited different thicknesses and densities of powder to the silicon substrate. To decrease the surfaces tension influence of liquid (20℃, water-air γ=72.86 $mN \cdot m^{-1}$; ethanol-air, γ= 22.39 $mN \cdot m^{-1}$), ethanol is used in alumina solution rather water. The ratio in alumina solution of alumina to ethanol is 25% by volume. The size of silicon we used in each is a rectangle with size no large than 2.5cm×2.5cm, as shown in figure 2.1.

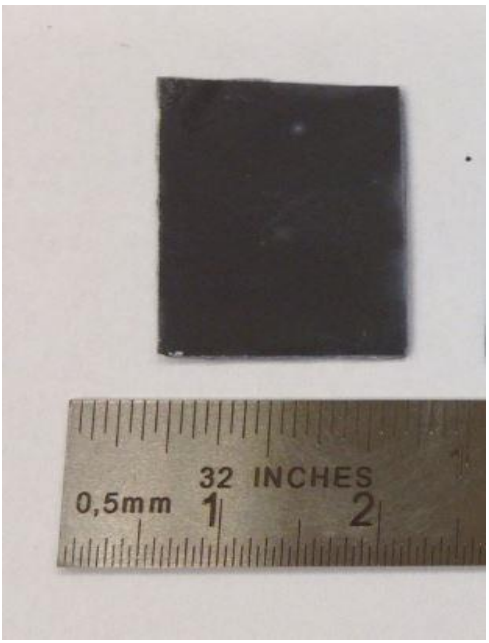

Fig. 2.1 Pure silicon wafer with natural oxide support for alumina powders

Dry powder application deposited the least powder on the silicon surface. Dry powder application is the simplest way of forming a powder-coated surface. To prepare a dry powder sample, the powder was first sprinkled on a clean silicon surface. Excess powder was removed with compressed air. While most of the alumina powder was removed with the compressed air, a layer of powder remained attached to the substrate, as shown by SEM images. Significantly more 50 nm alumina powder particles remained on the surface relative to the 10 μm powder.

Spin coating involved adhering the silicon wafer in the center of a custom-made centrifugal spinning device consisting of a variable power supply, a 3,000 RPM electronics fan, and a custom enclosure. The fan is made by Cooler Master, Inc, with model number E255988-CF. This home-made spin casting machine has been shown to produce uniform coating layers of photoresist [77]. Alumina solution is applied to the center of the silicon

surface. The fan is then turned on at full speed for 30 seconds. With centrifugal force, the solution is removed and an alumina surface is formed. Because the solution is non-uniform, consisting of powder particles and ethanol, the resulting coating is not as completely uniform.

Dip coating involved dipping a silicon wafer into the alumina solution and then removing it from the solution perpendicularly. Excess solution collected and drained off of the trailing edge of the substrate by gravity. The ethanol in the solution-coated portion of the substrate evaporated in quiescent air, leaving behind the alumina powder. Because of gravity, the alumina deposition was non-uniform, with most alumina deposited along the draining surface of the substrate. The bottom-most 0.3 cm of the draining end of the substrate was cut off by razor blade to keep the dip coating surface relatively uniform.

The tape casting method used a relatively thick application of the alumina solution to the silicon surface. A mechanical blade oriented a fixed displacement above the substrate is passed over the solution at a constant speed. The slurry of powder and ethanol is formed to a uniform height. In this method a razor blade is used to form a uniform alumina film on silicon. A single sheet of cellophane tape was place on the of silicon wafer to serve as a mask to contain the alumina and ethanol slurry. After a drop of the alumina solution was dropped on the silicon wafer; the razor blade is used to remove all the slurry that is higher than the thickness of the cellophane tape. After the ethanol evaporated, the tape was removed.

Each of the four surface forming mechanisms were incorporated using powders of 50 nm and 10 μm alumina. Optical images of the four surfaces are listed below in figure

2.2 & figure 2.3.

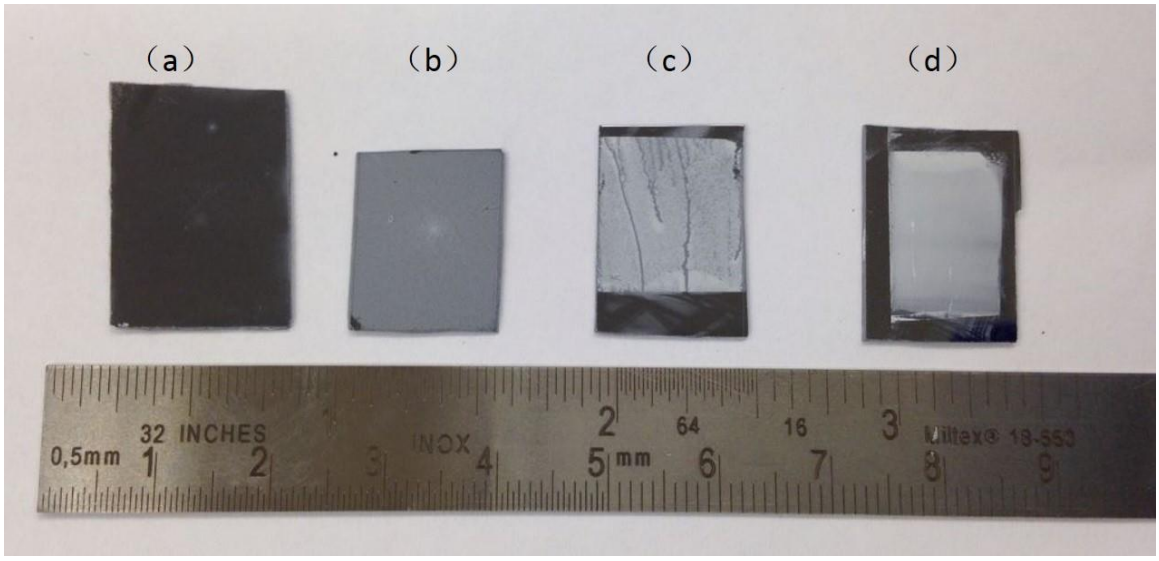

Fig. 2.2 50 nm Alumina powders on silicon wafers deposited by (a) dry powder application, (b) spin coat application, (c) dip coat application, (d) tape casting application.

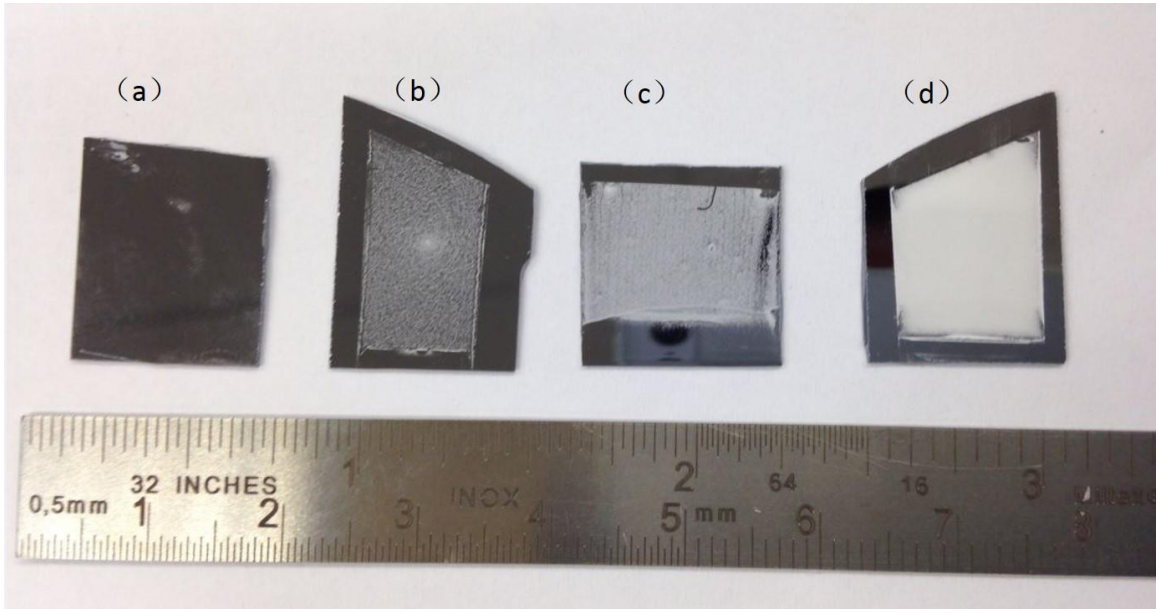

Fig. 2.3 10µm alumina powders on silicon wafers deposited by (a) dry adhesion, (b) spin coating, (c) dip coating, and (d) tape casting application

2.2 Synthesis Carbon Nanotubes

2.21 Procedure of synthesis carbon nanotubes

The method we use in our parametric study of synthesis CNTs on powder is floating catalyst chemical vapor deposition (FCCVD). Floating catalyst chemical vapor deposition was first used to produce CNT forests by H. M. Chen [78] in 1998. In this method, ferrocence ($C_{10}H_{10}Fe$) is used as catalyst precursor. Ferrocence powder is dissolved in an organic solvent (typically xylenes) at ratios set by the experiment need. The ferrocene/xylene solution is then introduced into the heated tube furnace to facilitate the CNT growth. The solution vaporizes and decomposes at low temperature (xylenes will boil at aapproximately 140 °C [79], while ferrocene will volatilize at 249 °C [80]) to form atomic iron and then agglomerates into iron clusters or nanoparticles (NPs). These iron particles will be transported through the reaction tube by flowing background gas (Ar). H_2 gas is supplied to reduce oxidized Fe into metallic Fe for catalysis. Note that CNT growth occurs on the processing tube itself throughout the heated region of the furnace. Because the catalyst is introduced in the vapor phase, it is distributed throughout the reaction tube; not just on the substrate of interest residing in the center of the tube.

The details of the chemicals used in these experiments are as follows. Xylene (C_8H_{10}) is a product of ALORICH Chemistry, the molecule weight is 106.17 g/mol, and purity is equal or more than 98.5%. Ferrocene ($C_{10}H_{10}Fe$). The ratio of xylene and ferrocene could be changed as the synthesis requires, but all of the samples we made for

this program are in the ratio of 10 wt.% ferrocene in xylenes. Figure 2.4 gives the details of real experiment equipment we used in our experiment.

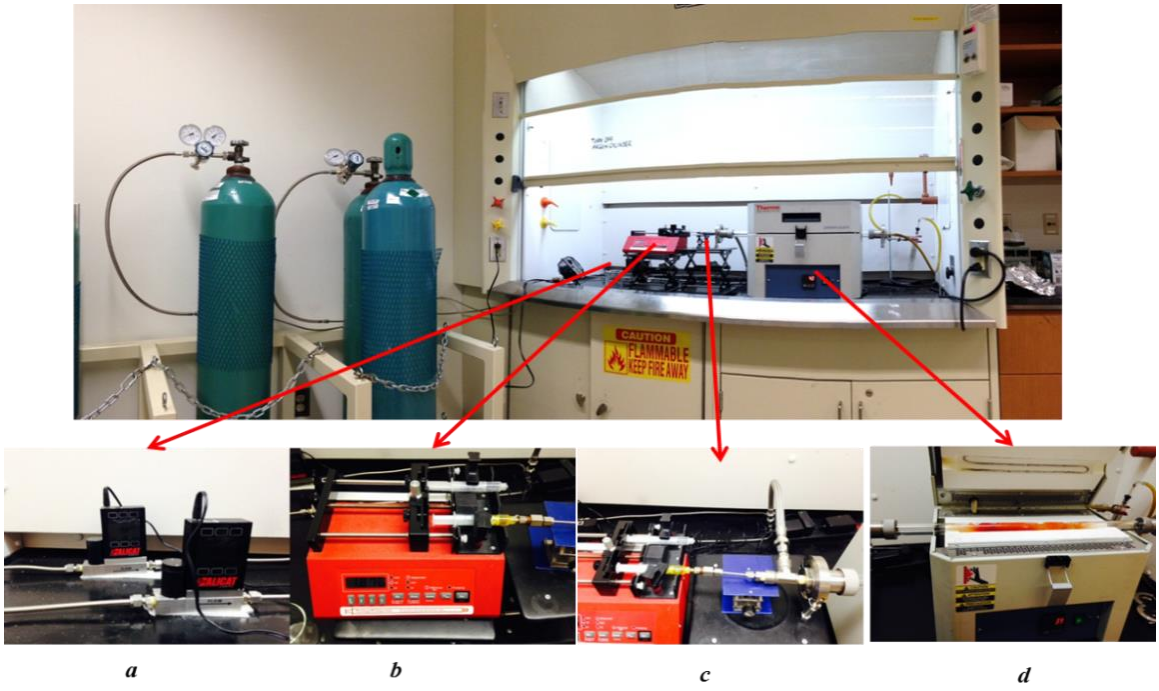

Fig. 2.4 Diagram of equipment used to synthesis carbon nanotubes using FCCVD in this program, (a) mass flow controllers, (b) syringe pump, (c) mixture of gas and ferrocence, (d) tube furnace and quartz tube.

As we can see from this figure, several equipment is connected together forming this FCCVD-CNTs synthesis system. All the detail information of equipment are supplied below.

(a) Mass flow controllers

The mass flow controllers (MC Series by Alicat Scientific, LLC.) are used to control volumetric flow rate of gas used during CNTs growth. Argon and hydrogen are used in our synthesis progress. Argon is used as an inert carrier gas, and hydrogen is to reduce iron oxide catalyst nanoparticles to metallic iron. Mass flow is changed by

mass flow controllers through all the progress of CNTs synthesis, mass flow rate consistent during the progress of heating and CNT growth.

(b) Syringe pump

The syringe pump we used is NE-4000 Double Syringe Pump by New Era Pump Systems Inc. The syringe pump used here is pumping the xylene/ferrocence solution into the tube furnace through a 1/8" stainless steel injection rod. There are three stages of injection during a CNTs growth experiment. The first stage is required to rapidly fill the length of the injector tube with 0.8 mL just prior to the initiation of CNT growth such that the solution nearly fills the initially voided injector tube length. This stage occurs when furnace researching temperature of 700℃ and requires 0.8 mL volume. This procedure occurs just before initiation of CNT growth because a portion of the injector tube resides in the heated zone of the furnace. Charging the injector tube with the solution before furnace heat up would lead to significant unwanted vaporization of solvent prior to the CNT growth stage. After the furnace reaches a temperature of 750℃, the second pumping stage corresponding with CNT nucleation and growth begins. In this stage, the pumping rate slowly pumps the xyelene/ ferrocence solution at a rate of 1 mL/hr or 2 mL/hr during the whole CNTs growth. The third pumping process is a withdraw progress after CNT growth stops. When CNTs growth time is finished, the hydrogen gas and ferrocence injection will be stopped. The directionality of the syringe pump is reversed after CNT synthesis, and all the liquid inside the pump tube is withdrawn back into the syringe.

The syringe pump is controlled from a microcontroller based system which drives a step motor, allowing a large range of pumping rates configured to the inside diameter of the loaded syringe. The syringes are driven from a drive-screw and mechanism.

(c) Tube furnace

The tube furnace used for CNT forest synthesis is a 1-inch diameter furnace (model of TF55030A), manufactured by Thermo Fisher Scientific. The furnace uses a type K thermocouple, mounted at the middle span of the tube furnace, for temperature feedback. Heating cycles are input using temperature set points and prescribed segment times. An on board microprocessor automatically optimizes control parameters during furnace operation. A maximum operating temperature of 1100℃ with an energy efficient moldatherm insulation make it suitable for high interior-exterior temperature differential.

There are three heating stages of CNTs synthesis in our program. They include: (I) temperature ramp from ambient to CNT synthesis temperature, (II) constant temperature CNTs growth, and (III) cool down. The typical ramp time to a growth temperature of 750^{o}C was 15 minutes.

(I) Sample preparation and CVD processing

Powder samples were prepared in the manners discussed in chapter 2.1. The nominal the ratio of ferrocence to xylene was 10% by weight. The ferrocence and xylene components were placed into a beaker and using and dispersed using ultrasonic mixing for about 2 minutes. After placing the powder silicon wafer in the center of tube furnace, the

tube furnace was connected to the inlet gasses and bubbler by flanges. Argon gas was flowed at a rate of 0.500 slpm (standard liter per minute), and then hydrogen was introduced at 50.0 sccm (standard cubic centimeter per minute). The tube furnace heating program was then initiated, allowing a ramp time of 15 minutes to the growth temperature of 750℃. Once the temperature of furnace reached 700℃, the syringe pump was primed by injecting 0.8 mL solution into evacuated injection tube.

(II) CNTs growth process

After the furnace temperature researched 750℃, CNTs growth was initiated. The gas mass flow remained the same as heating up progress. The ferrocence solution was injected at a rate1ml/hr. CNTs growth occurred once the ferrocene solution was introduced into the processing tube. The growth time was typically 1 hour, unless otherwise stated.

(III) Cool down process

After the growth time is completed, the furnace heating is ceased, and the temperature decreases. The hydrogen gas flow was then ceased, and the argon flow rate was decreased to 0.100 slpm. Samples were removed when the furnace temperature reached room temperature. Images of the CNT products can be seen in Figures 2.5 & 2.6.

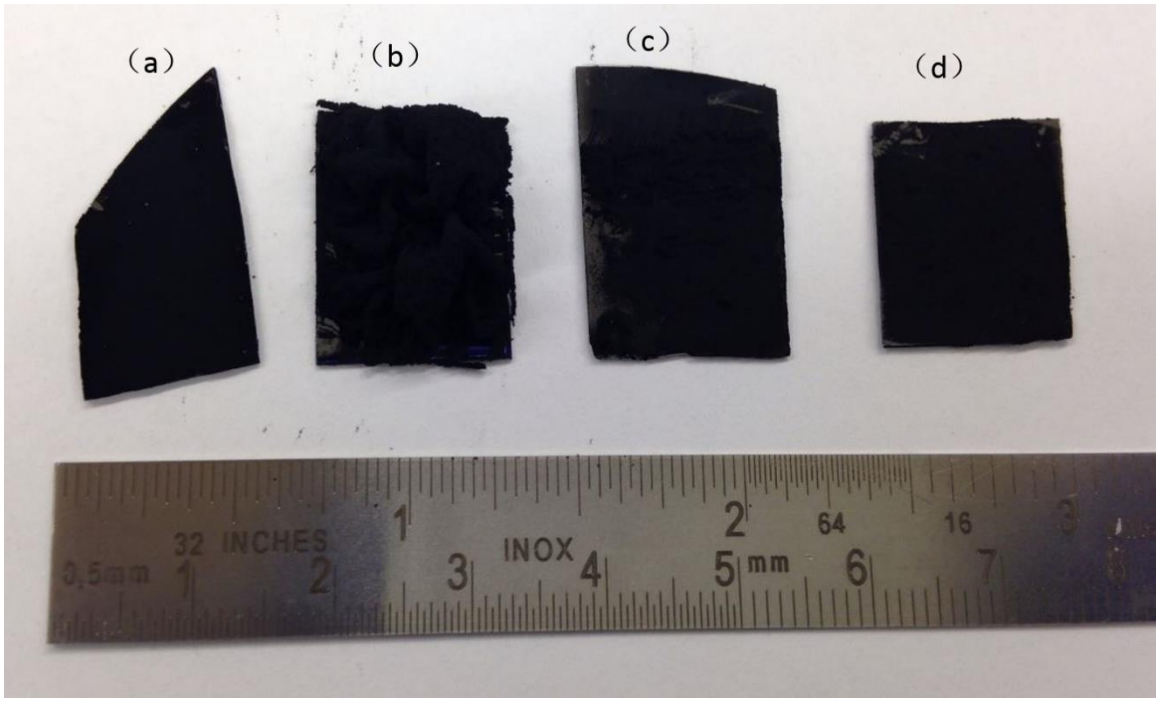

Fig. 2.5 CNTs grown from 50 nm alumina particles supported on silicon wafers. The powder was applied by (a) dry adhesion, (b) spin coating, (c) dip coating, and (d) tape casting.

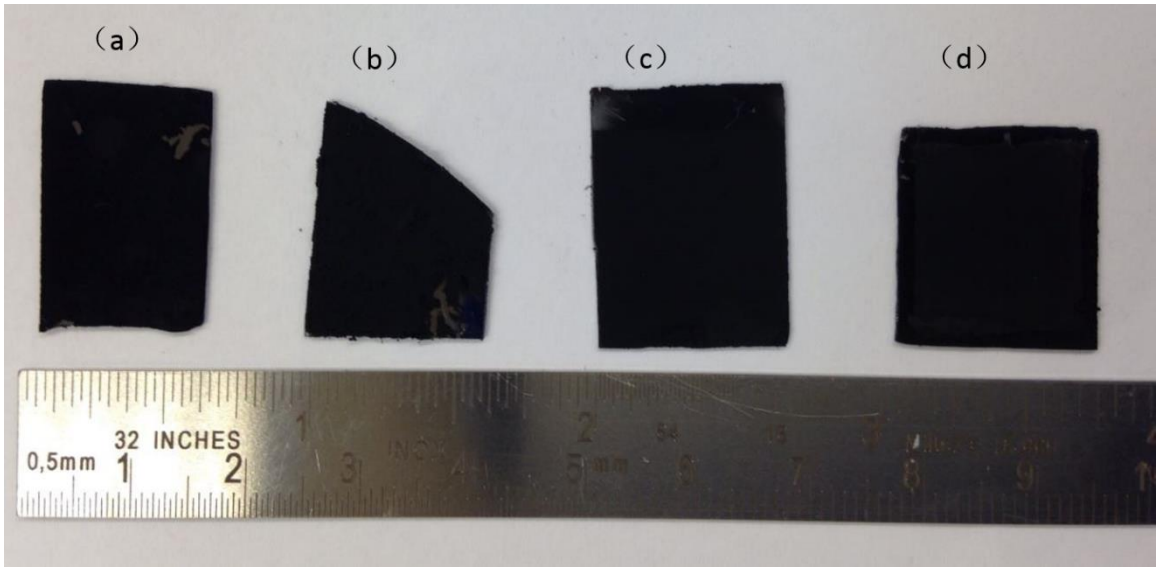

Fig. 2.6 CNTs grown from 10 mm alumina particles supported on silicon wafers. The powder was applied by (a) dry adhesion, (b) spin coating, (c) dip coating, and (d) tape casting.

2.3 SEM and TEM

2.31 Scanning Electron Microscope

Scanning Electron Microscope (SEM) is a powerful instrument for imaging of fine structures of materials and nanoparticles fabricated by the nanotechnology. There are lots of intrinsic advantages of SEM such as minimal sample preparation, high analysis throughput, high resolution (down to 1 nm in modern instruments), intuitive image interpretation, and relatively low setup cost. All of these contribute to the importance of SEM nowadays as it is already being the workhorse used in present nanotechnology. The SEM has a large depth of field, which allows more of a specimen to be in focus at one time. All of these advantages, as well as the actual strikingly clear images, make the scanning electron microscope one of the most versatile materials characterization tools in research today.

In our program, SEM is also a basic research tool used to expand our vision on CNTs grown on alumina powders. Since both powders and CNTs are all nanosize material, the substrate—alumina should be scanned before and after growth. By comparing the images before and after growth and the difference procedure of surface preparation, some conclusions such as the influence of growth time, growth temperature could be obtained with SEM images. High resolution SEM images would also tell us the length of CNTs, area density and etc.

Two SEM instruments are used in this work, each located in Electron Microscopy Core (EMC) at the University of Missouri-Columbia. These instruments include Hitachi

S4700 and FEI Quanta 600 FEG. An image of the Hitachi S4700 Scanning Electron Microscope (SEM) is shown below and equipment specifications are listed.

Fig 2.7. Hitachi S4700 Scanning Electron Microscope (SEM)

An image of the FEI Quanta 600 FEG Extended Vacuum Scanning Electron Microscope (ESEM) is showing below and equipment specifications are listed.

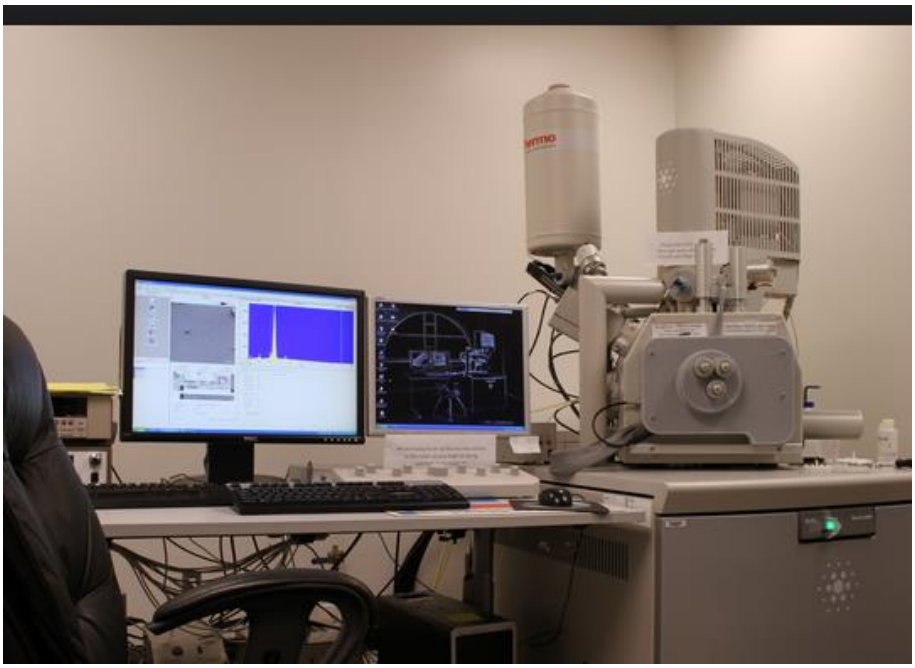

Fig 2.8 FEI Quanta 600 FEG Extended Vacuum Scanning Electron Microscope (ESEM)

2.32 Transmission electron microscopy

To understand the internal structure of the CNTs synthesized, it is necessary to use transmission electron microscopy (TEM). This technique has the advantage of higher magnification than SEM. By using TEM, it is possible to effectively image down to atomic scale. The high resolution of TEM not only could offer the information of diameter of CNTs from different or different surface film but also the layers information of graphite sheets. Comparing to SEM, the increased resolution from TEM is primarily due to a higher accelerating voltage of the electron gun; which decreases the electron wavelength and helps the electron beam penetrate through material layers. Accelerating voltages in TEM are typically in the range of 100 to 400kV.

The FEI Tecnai F30 Twin HRTEM is a 300kV field emission gun (FEG) high resolution TEM/STEM which was installed in May 2012 in University of Missouri-Columbia. The microscope has a Twin objective lens with a spherical aberration (Cs) of 2.0 mm. With its 300 kV acceleration voltage and its Schottky field emission source, this instrument provides outstanding stability, ease-of-use and high-resolution performance in TEM/STEM imaging and microanalysis [81].

Phase contrast of TEM allows for lattice imaging, a powerful technique that allows one to view single layer of CNTs. Phase contrast occurs when electrons of different phases interact with one another and form an image. By passing multiple electron beams through a sample, multiple lattice images are formed and can be combined to obtain a complete picture of the atomic structure.

Samples scanned by TEM should be no thicker than a few hundred nanometers. For all the samples grown on 50 nm alumina powders, they satisfy this requirement, but for CNTs samples grown on 10um alumina powders, they are much bigger then hundred nanometers. To solve this problem, an ultrasonic mixer is used to separate the powders and CNTs. Short CNTs are produced by ultrasonic and dispersed in ethanol, they will be placed on an amorphous carbon grid before putting into TEM. An image of The FEI Tecnai F30 Twin HRTEM is showing below and equipment specifications are listed.

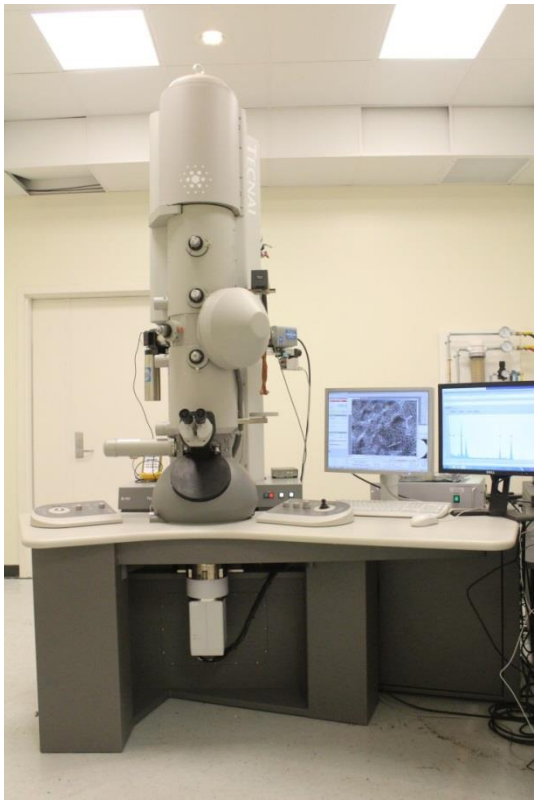

Fig 2.9 The FEI Tecnai F30 Twin HRTEM

2.4 Thermo-gravimetric analysis

Thermogravimetric analysis (TGA) is an analytical technique used to determine a material's thermal stability and its fraction of volatile components by monitoring the weight change that occurs as a specimen is heated. The measurement is normally carried out in air or in an inert atmosphere, such as helium or argon, and the weight is recorded as a function of increasing temperature. Sometimes, the measurement is performed in a lean oxygen atmosphere (1 to 5% O_2 in N_2 or He) to slow down oxidation. In addition to weight changes, some instruments also record the temperature difference between the specimen and one or more reference pans (differential thermal analysis, or DTA) or the heat flow into the specimen pan compared to that of the reference pan (differential scanning

calorimetry, or DSC). The latter can be used to monitor the energy released or absorbed via chemical reactions during the heating process. In the particular case of carbon nanotubes, the weight change in an air atmosphere is typically a superposition of the weight loss due to oxidation of carbon into gaseous carbon dioxide and the weight gain due to oxidation of residual metal catalyst into solid oxides.

TGA is one method used to characterize the purity of carbon nanotubes. It is well documented that amorphous carbon burns at a lower temperature (400°C) than graphitic carbon [82]. After this initial weight loss, as temperature keeps rising, a second weight change will occur as the graphitic carbon comprising the CNT walls oxidizes and converts to CO_2. If a high amount of amorphous carbon or other non-crystalline carbon is present, appreciable weight loss should occur around 700°C. It is difficult to identify by visual inspection of the weight loss as a function of temperature if there are multiple temperatures where appreciable weight loss occurs. Taking the derivative of the weight as a function of temperature makes it easy for identification of the temperature where weight loss occurs.

In order for the instrument to remain relatively stable before oxidation occurs, over 1 mg of material should be contained inside the hanging sample pan-a platinum metal pan with accurate weight (Figure 2.10), normally the weight should be more than 1.5 mg to keep the accuracy of TGA analysis result. If too little initial mass is in the system significant fluctuations in the measured data, are observed. After the CNT array has been entirely burned away, the remaining mass should theoretically be the catalyst particles and their support. Normally, the total mass of all of the residual catalyst particles will be very small, most likely on the order of a few micrograms. The sensitivity of the instrument should always be verified and reported if necessary [82].

Fig 2.10. TGA Metal Sample Pan

In our program, the TGA analysis is used to tell the mass difference of CNTs grown on different powders and the influence of surface preparation progress. The mass left over on the platinum pan would be iron metal and alumina powder used as CNTs support. All CNTs and powder were removed from the silica support using a razor blade. The TGA equipment we used is Thermogravimetric Analyzer Models Q50by TA Instruments-Waters LLC. Figure 2.11 shows the whole system of thermal gravimetric analyzer.

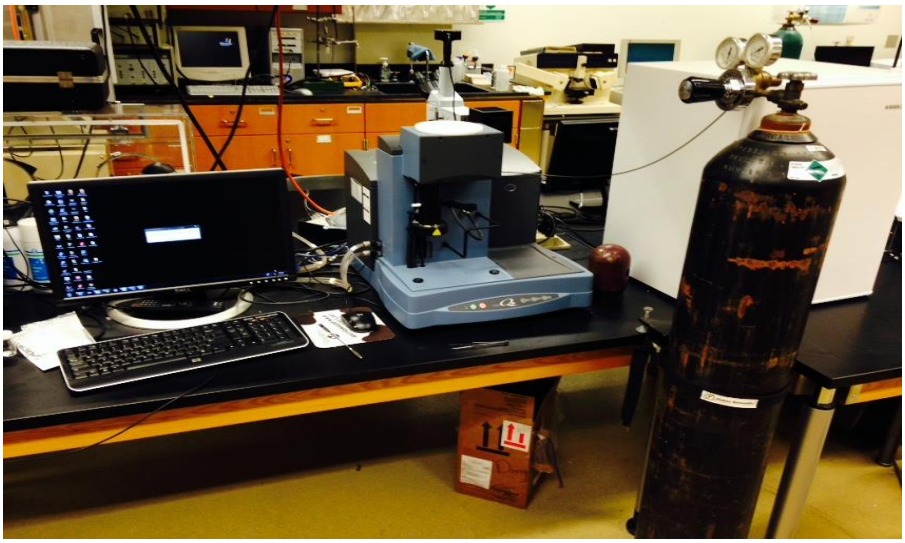

Fig 2.11. Thermogravimetric Analyzer Models Q50

2.5 Raman Spectroscopy

Raman spectroscopy is the most common spectroscopic mean for assessing molecular motion and fingerprinting species while coming to CNTs. It is a popular technique for determining the diameter distribution, chirality, purity, and architecture of CNTs [83]. Experimentally the technique is relatively simple. A typical spectrum of a sample of MWCNTs is shown below in figure 2.12 and the main features are as follows.

(1) A low-frequency peak (<200cm^{-1}), assigned to the symmetry radial breathing mode (RBM) of single-walled or double-walled CNTs. The frequency of the peak depends on the diameter of the tube, as discussed below.

(2) A strong feature at around 1340 cm^{-1}, called D line, assigned to disordered graphitic material.

(3) A group of peaks in the approximate range 1550—1600 cm^{-1} labelled the G band. In graphite, the G band exhibits a single peak at 1582 cm^{-1} related to the tangential mode vibrations of C atoms.

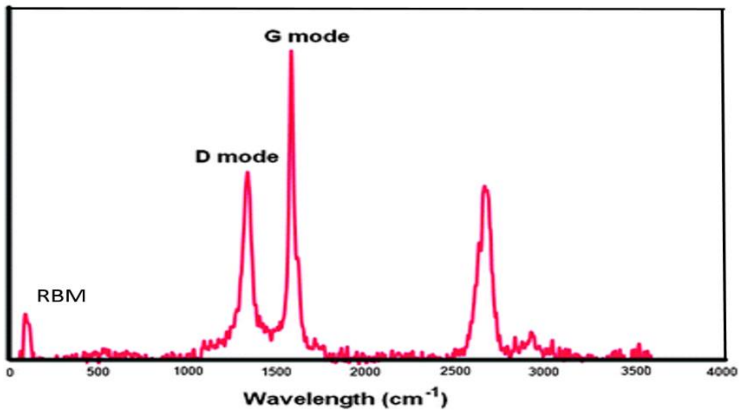

Fig 2.12. Raman spectrum from a CNT sample [83]

D band

The D (or disordered carbon) band is a longitudinal optical (LO) phonon mode and is known as the disordered or defect mode. The D band is present in all carbon allotropes, including sp^2 and sp^3 amorphous carbon. In CNTs, this band is activated from the first-order scattering process of sp^2 carbons by the presence of in-plane substitutional hetero-atoms, vacancies, grain boundaries, or other defects, and by finite-size effects. All of these characteristics lower the crystal symmetry of the quasi-infinite lattice.

When observed in MWCNTs, the D band has been generally viewed as a defect in the tubes. The quality of a sample has often been evaluated using the D/G band intensities. The D-band width for CNTs is generally 10 to 20 cm^{-1}.

G Band

The G (or graphitic carbon) band is a tangential shear mode of carbon atoms that corresponds to the stretching mode of the C=C bond in the graphite plane. The G-band in CNTs involves an optical phonon modes between the two dissimilar carbon atoms in a unit cell. It is known to originate from sp^2 carbon sites present in the sample [84--86]. This band essentially represents the ν(C=C) stretching vibration of all pairs of sp^2 atoms in the ring. The G band is, therefore, highly sensitive to strain effects in sp^2 nano-carbons and can be used to probe any modification to the flat geometric structure of graphene.

In simple graphite, a single mode is normally observed at 1580 cm^{-1}. In CNTs this mode transforms into two modes as a result of the confinement of wave-vectors along the circumference [87]. The frequency of the high-energy branch G^+ does not vary with

diameter, whereas the lower energy branch G^- becomes softer for smaller diameter CNTs. One of the more intriguing aspects of CNTs is that they can be either metallic or semiconducting with variable and direct band gap. Vasconcelos [18] and coworkers showed that metallic tubes are easily recognized by the broad and asymmetric line shape of the G^- band. The frequency downshift of the G^- band is particularly strong for metallic tubes, with downshifts of greater than 100 cm^{-1} for smaller diameter tubes, whereas the G^+ frequency remains essentially constant with diameter for metallic and semiconductor tubes. The most dramatic features of the G-band spectra are the characteristic differences between the G-band spectra for metallic and semiconducting nanotubes.

RBM Mode

The most prominent Raman features in CNTs is the radial breathing modes (RBMs). The RBM mode is specific to CNTs and presents the isotropic radial expansion of the tube. The RBM frequency is inversely proportional to the diameter of the tube, making it an important feature for determining the diameter distribution in a sample. RBM bands are a useful diagnostic tool for calculating the presence of CNTs in a sample. RBM modes are typically active for SWNTs or few-walled CNTs.

Since the RBM mode is not present in other carbon material, it is always used to confirm the presence of CNTs. It is located between 75 and 300 cm^{-1} from the excitation line, and is associated with the symmetric movement of carbon atoms in the radial direction. The relationship between the RBM frequency and the nanotube diameter gives as [88]:

$$\omega_r(\mathrm{cm}^{-1}) = 224(\mathrm{cm}^{-1})/d_t \text{ nm}$$

D and G bands intensity ratios

The ratio of the intensities of D and G bands is a good indicator of the quality of bulk samples. Similar intensities of these bands indicate a high quantity of structural defects. MWCNT spectrum is the one which shows the lowest ratio, consequently higher quantity of structural defects due to its multiple graphite layers. Both SWCNT and DWCNT show higher differences in intensities of D and G bands. The ratio between D and G band and the RBM and its relation to the diameter distribution are very important factors allowing one to distinguish between three types of nanotubes with a single analysis.

The ratio of intensity of D/G bands is a measure of the defects present on graphene structure. The G band is a result of in-plane vibrations of sp^2 bonded carbon atoms whereas the D band is due to out of plane vibrations attributed to the presence of structural defects. By comparing the I_D/I_G, the amount of disorder in CNTs could be easily be computed.

Chapter 3 Results and Discussion

Each of the 8 different alumina-CNTs sample configurations (4 catalyst deposition techniques and 2 nominal particle sizes) were subjected to multiple analysis techniques to characterize the CNT yield with respect to CNT morphology, density, morphology, and diameter distribution. The techniques used include scanning electron microscopy (SEM), transmission electron microscopy (TEM), thermo gravimetric analysis (TGA) and Raman spectroscopy.

SEM images provide the structural morphology of the alumina particles after application to the silicon substrate and after CNT synthesis from the. EDS elemental mapping in SEM allows clear demarcation of alumina particles and CNT products. High resolution TEM images provide information about the CNT walls and (inner and outer) diameters, and with TEM EDS mapping, elements in the composite material could be easily detected. TGA is a useful analysis technology to determine a material's thermal stability and its fraction of volatile components. Raman spectroscopy interrogates the vibrational properties and electronic structures of CNT, particularly for characterization of CNT diameters, and relative quality of the samples. With all these analyses applied, the properties of CNTs grown on alumina particles are better understand.

After a thorough characterization of CNTs grown on alumina particles, the CNTs are used as sensors and oil capture device. The demonstrations of using CNTs grown on alumina particles proves the alumina-CNTs great potential for sensing with excellent performance in terms of linearity, selectivity, stability and fast response, open up a wide range of CNTs sensor applications and offer potential in the upcoming field of flexible

electronics. The reusable CNTs oil capture provide a new environment-friendly oil capture device with great capture ability by weight which maybe also create a new area where high-volume CNTs are greatly welcomed. Because of the relatively high iron content that remains in the CNT core after synthesis, the CNTs may be manipulated on a fluid surface using magnetic fields.

3.1 SEM Analysis

CNT forests were grown from alumina powders dispersed on silicon substrates by various mechanisms, resulting in varying powder deposition morphologies. To understand the mechanism of CNT growth on powders, powders before growth and after CNT growth were analyzed using a scanning electron microscope (SEM). SEM is a type of electron microscope that produces images of a sample by scanning it with a focused beam of electrons. The electrons interact with atoms in the sample, producing various signals such as secondary electron, backscattered electron and X-rays. These signals contain information about the sample's surface topography and composition. The SEM used here is FEI Quanta 600 FEG Extended Vacuum Scanning Electron Microscope.

Two nominal sizes of alumina particles were examined—50 nm alumina powders and 10 μm alumina powders. Four different application methods were used to produce different alumina powder densities on the silicon substrate. These techniques include dry powder application, spin coating, dip coating, and tape casting. Each application technique was used for each nominal powder size as we talked in chapter 2, resulting in 8 distinct samples.

Figure 3.1-3.8 show SEM images for 8 different powder application techniques.

3.11 SEM analysis of powder dispersion on silicon substrates

50 nm Powder Applied Using Dry Adhesion

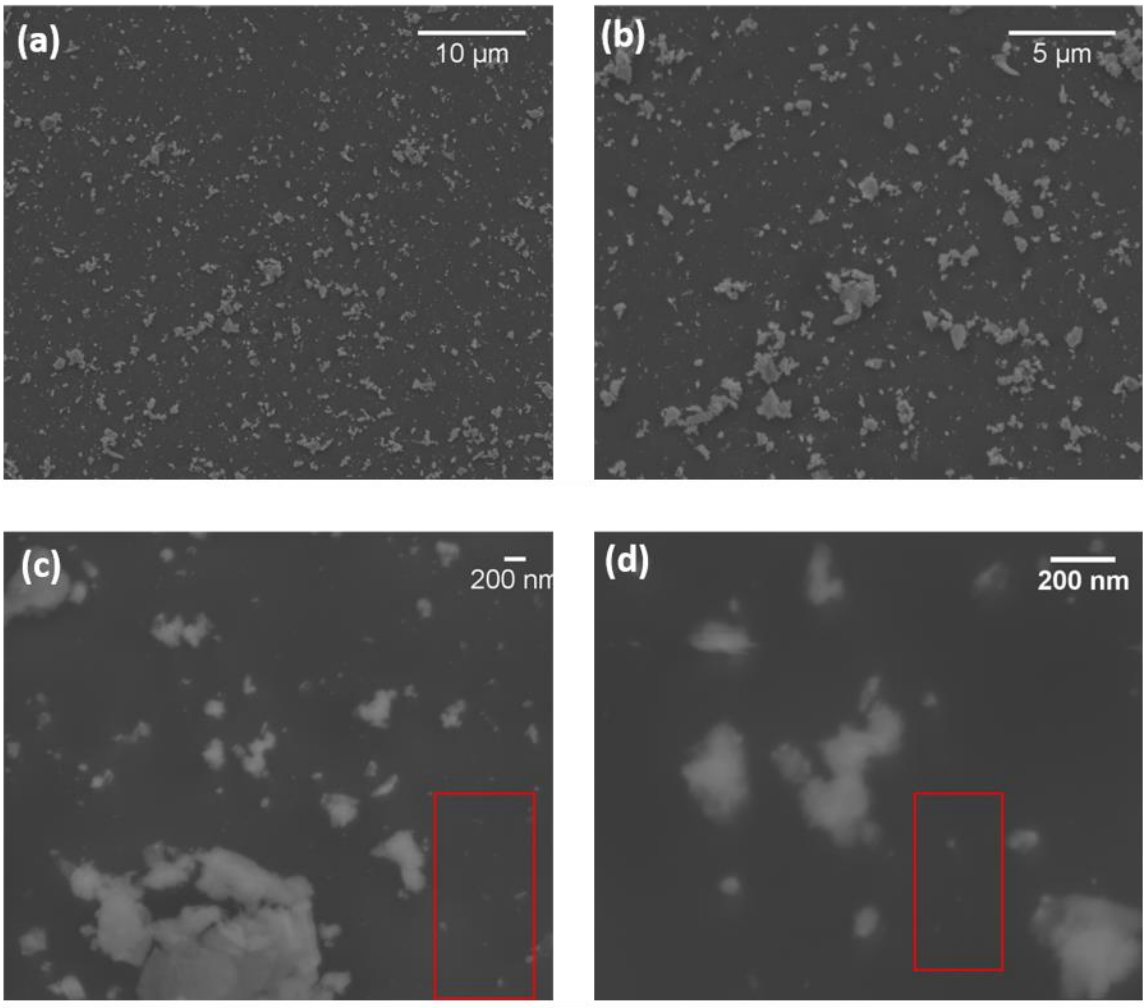

Fig 3.1 Representative SEM images of 50 nm alumina powder on silicon wafers, prepared by dry powder application. Particles are adhered to silicon by van der Waals force. Particle density is relatively sparse, with large regions of bare silicon. Note that the 50 nm particles form larger agglomerations ranging from 100's of nanometers to microns in size. Red box in (c) (d) shows small size alumina particles on silicon.

The 50 nm alumina particles applied by the dry adhesion technique are uniformly dispersed on the silicon substrate, as observed in Fig. 3.1. Particles adhere to the substrate

by van der Waals force alone. Particle agglomerates in excess of 50 nm are commonly observed and generally vary in size between 100 nm to approximately 3 μm. The agglomerates are held together by Van der Waals force, which may be expressed as

$$F_{VdW} = -\frac{A \cdot R}{12\delta^2}$$

Where A is the Hamaker constant (assumed to be 1x 10^{-19} J) [89], R is the particle radius, and δ is the separation distance between particles (measured from the perimeter of the particles). If we assume that each particle is a 50 nm diameter sphere, and a separation distance of 100 nm, the resulting van der Waals force is 2 x 10^{-12} N. By comparison, the weight of the particle imposed by gravity assuming a particle density of 4,000 kg/m^3 is only 2.5 x 10^{-18} N, 6 orders of magnitude less than the van der Waals force. Therefore, the van der Waals force for 50 nm diameter particles is quite significant, while the gravitational force is orders of magnitude less. Note that the van der Waals force will vary as R, while the weight of a particle will vary as R^3. While the alumina particle coating observed by SEM is relatively uniform, the density of particles is the lowest of the application techniques.

50 nm Powder Applied Using Spin Coating

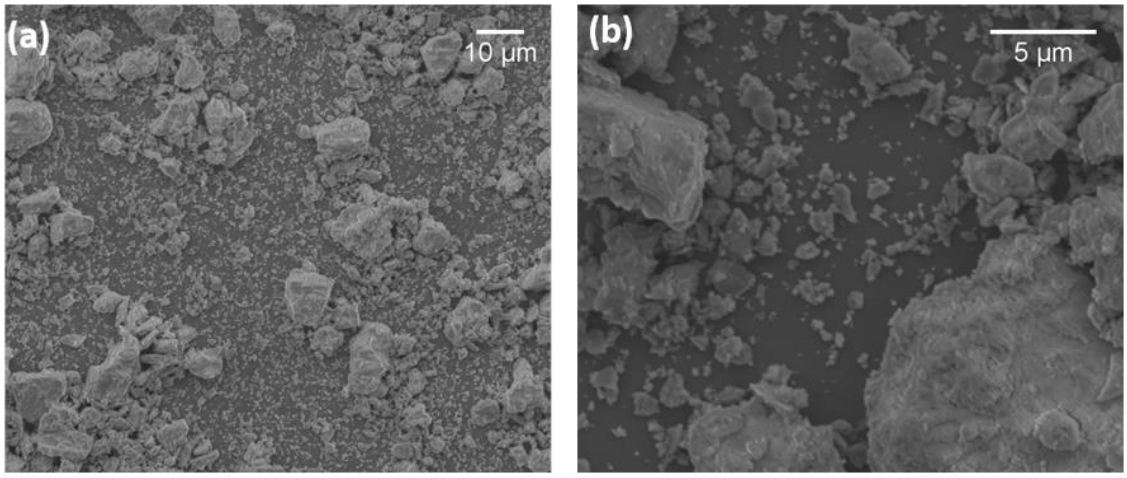

Fig 3.2 Representative SEM images of 50 nm alumina powders applied by spin coating from an ethanol solution onto silicon. The agglomerated particles range in size from 100's of nanometers to greater than 10 µm and are more densely populated than the particles applied by dry adhesion.

The 50 nm alumina particles applied by the spin coating technique are uniformly dispersed on the silicon substrate, as observed in Fig. 3.2. The large size of alumina particles agglomerated in this technique when all the powders are mixed with the ethanol solution and are likely further densified by surface tension forces during solvent evaporation. The agglomerated particles range in size from 100 nm to greater than 10 µm and are more densely populated than the particles applied by dry adhesion. Some alumina particles are also observed in spin coating application and the size could be small as 50 nm. No wide-spread region of densely populated, continuous particle agglomerates are found on the surface. Rather, most of the surface is covered by the agglomerated particles.

50 nm Powder Applied Using Dip Coating

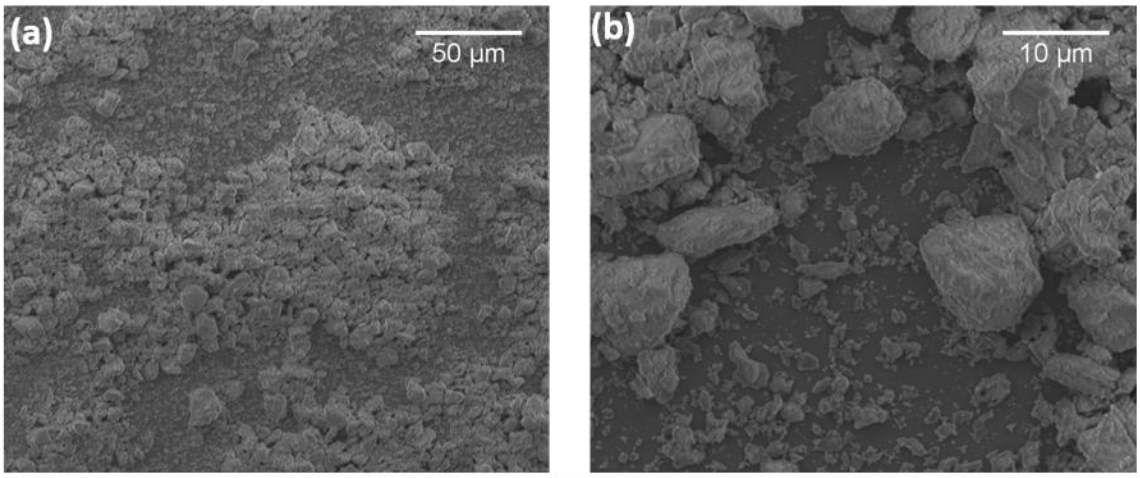

Fig 3.3 Representative SEM images of 50 nm alumina powder applied by dip coating from an ethanol solution onto silicon wafers. Large regions of densely populated, continuous particle agglomerates fill a large fraction of the surface. Discrete agglomerated particles ranging from 100's of nanometers to 10's of microns are also observed.

The 50 nm alumina particles applied by the dip coating technique form a nearly continuous coating on the silicon substrate, as observed in Fig.3.3. Particles agglomerates in this technique are thought to form when all the powders are mixed with the ethanol solution and during subsequent solvent evaporation. These agglomerated particles are discrete on the silicon wafer and the size of particles range from 100 nm to 10 µm. Single small size of particles as 50 nm are also observed on silicon surface. Except these, large regions of densely populated, continuous particle agglomerates fill a large fraction of the surface are also observed in this application. The particles density is slightly higher than the application of spin coating and much higher than the dry adhesion.

50 nm Powder Applied Using Tape casting

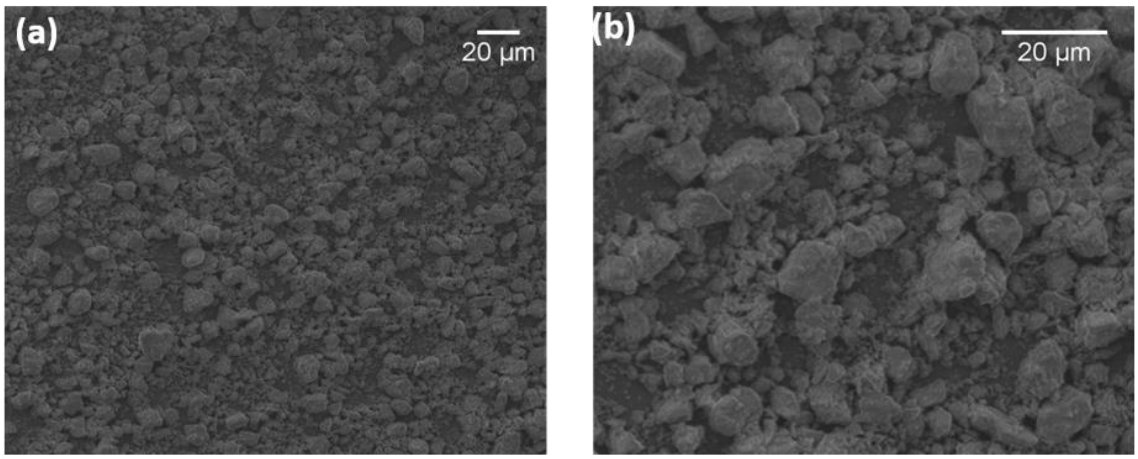

Fig 3.4 Representative SEM images of 50 nm alumina particles applied to a silicon wafer by tape casting. Nearly uniform populations of large alumina agglomerates cover the silicon surface. Agglomerated particle sizes are most commonly 1 – 20 microns in size.

The 50 nm alumina particles applied by the tape casting technique densely coat the silicon substrate, as observed in Fig.3.4. As observed, more large alumina particle agglomerates are formed in this technique since all the powders are mixed with the ethanol solution. Agglomerated particle sizes most commonly ranging from 1 μm to 20 μm. And also, small size particle as 50 nm still exist and lied between the agglomerated ones. Higher density of agglomerated particles are left on the silicon and nearly uniform populations of large alumina agglomerates cover the silicon surface which also indicates that the density of particles are the highest in all the 4 different applications.

The SEM images of these 50 nm alumina particles surface applications shows the details of how alumina particles distributed on the silicon wafers. The dry powder adhesion application are quite different from the other 3 "wet" application in both particle size and particle density since it is the van der Waals force that adhere the particles on the silicon and adhere particles together. Because no solvent is used, surface tension from evaporating solvent is not present to further densify particle agglomerates. The spin coating, dip coating

and tape casting application are all using ethanol solution as dispersing agent. A higher density of alumina particles were deposited on silicon wafer than dry adhesion application and agglomerate particles are all observed, the size ranging from 1μm to 20 μm. Some small alumina particles as small as 50 nm existed between the gap of these agglomerate particles. Tape casting gives the highest powder density and nearly uniform populations of large alumina agglomerates cover the silicon surface.

10 μm Powder Applied Using Dry Powder

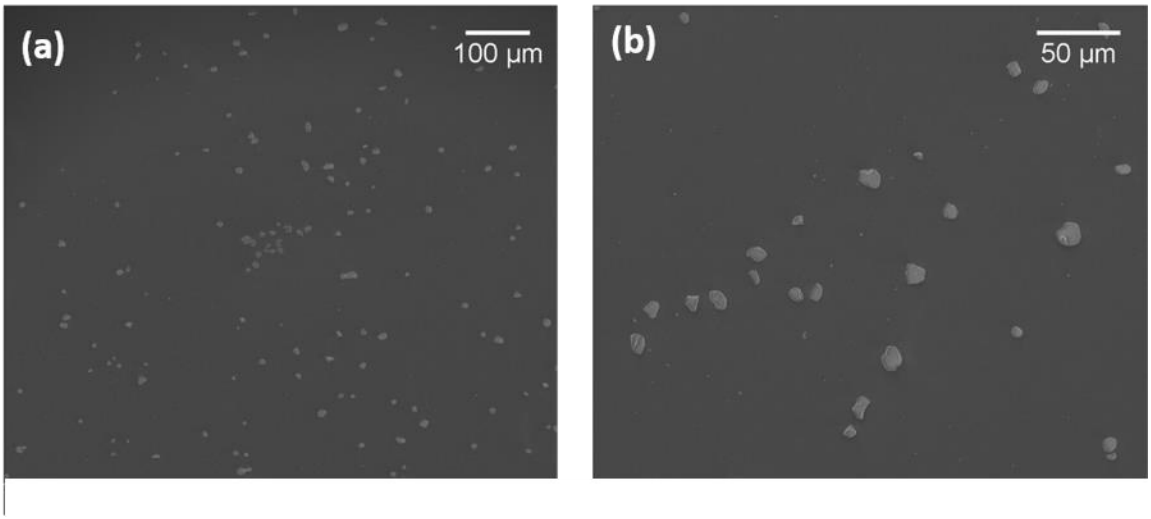

Fig 3.5 Representative SEM images of 10μm alumina powder on silicon wafers applied by dry adhesion. Only a sparse amount alumina powder is found, with no observed agglomerated particles.

As we could observed in the SEM images, there is significantly fewer 10 μm alumina particles left on the silicon wafer after dry adhesion. The density of particles dispersed on the silicon substrate applied by the dry adhesion technique is much less than that obtained 50 nm dry powder application, as observed in Fig. 3.5. Many of the 10 μm particles form irregular platelets intermixed with jagged and irregularly shaped particles that look similar to gravel. Only a sparse amount alumina powder is found, with no observed agglomerated particles. Same as 50 nm dry powder application, particles adhere

to the substrate by van der Waals force alone. The particles stick on silicon wafer by van der Waals force, which may be expressed as

$$F_{VdW} = -\frac{A \cdot R}{12\delta^2}$$

Where *A* is the Hamaker constant (assumed to be 1x 10^{-19} J), *R* is the particle radius, and δ is the separation distance between particles and silicon wafer. If we assume that each particle is a 10 μm diameter sphere, and a separation distance of 10 nm, the resulting Van der Waals force is 4 x 10^{-10} N. Because the particles are not spherical in morphology, the computed force will overestimate the anticipiated van der Waals force. By comparison, the weight of the particle imposed by gravity assuming a particle density of 4,000 kg/m^3 is 2 x 10^{-11} N, similar to the van der Waals forceis less than the weight. Therefore, the van der Waals force for 10 μm diameter particles is less significant. The 10 μm alumina particles will agglomerate significantly less than 50 nm alumina particles. Similarly, the force pinning the particles to the planar substrate is a factor of two greater than the force between particles Fewer 10 μm particles are adhered to the silicon substrate based on a similar argument.

10 µm Powder Applied Using Spin Coating

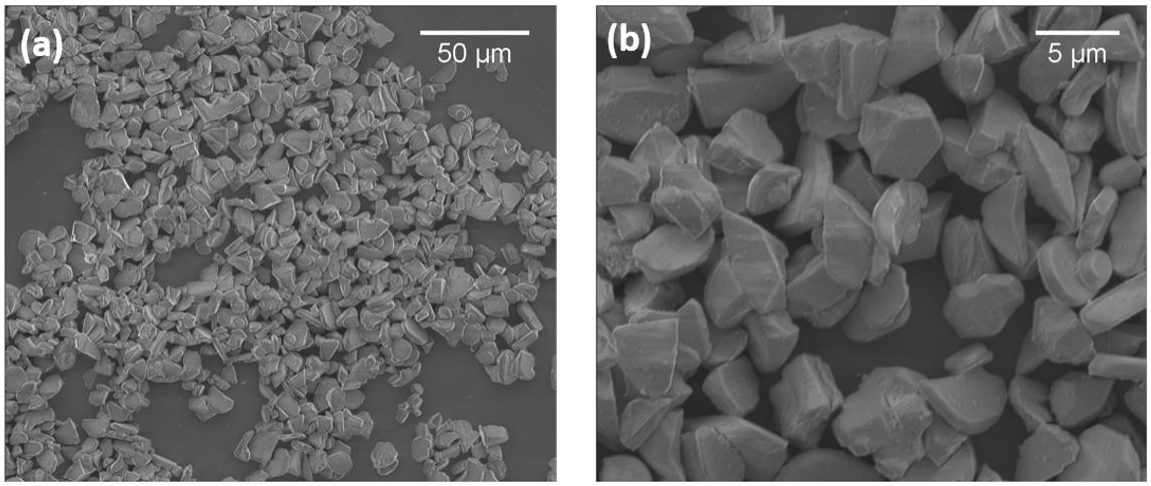

Fig 3.6 Representative SEM images of 10µm alumina powder applied to silicon by spin coating from an ethanol solution. A large density of powder is found, with a thickness of generally 1-2 particle layers.

The 10 µm alumina particles applied by the spin coating technique are more densely dispersed on the silicon substrate relative to the dry application, as observed in Fig.3.6. Although ethanol solution used as dispersing agent, little particle agglomeration is observed, which is different than observations when using 50 nm size particles. Particles generally form 1-2 layers.

10 μm Powder Applied Using Dip Coating

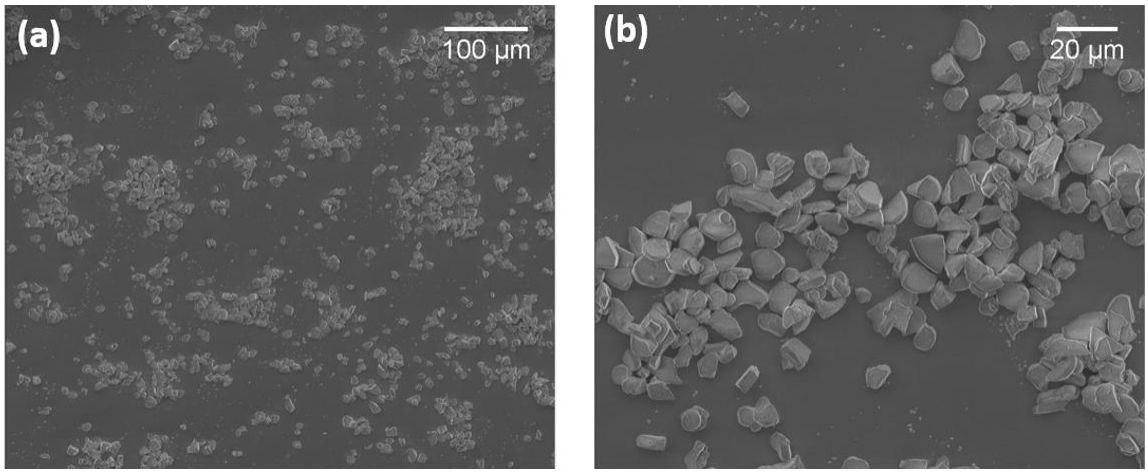

Fig 3.7 Representative SEM images of 10μm alumina powder applied to silicon by dip coating from an ethanol solution. The density of powder is less than that observed for spin coating, with a thickness of generally 1-2 particle layers.

The 10 μm alumina particles applied by the dip coating technique are dispersed on the silicon substrate in regions of relatively high density separated by regions of little or no particle deposition, as observed in Fig.3.7. Similar to the 10 μm spin coating surface application, there is no particle agglomerate together observed, which is different from what we get in 50 nm size particles. The density of powder is less than that observed for spin coating, with a thickness of generally 1-2 particle layers.

10 µm Powder Applied Using Tape Casting

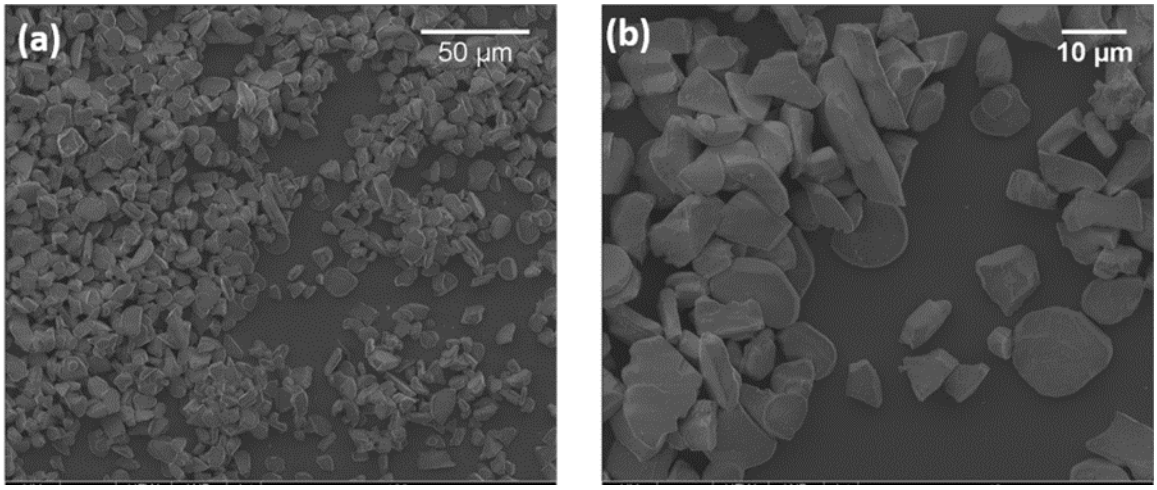

Fig 3.8 Representative SEM images of 10µm alumina powder applied to silicon by the tape casting method. Particle density is high, with relatively uniform coverage. The film thickness is generally a few particle layers.

The 10 µm alumina particles applied by the tape casting technique are relatively uniformly dispersed on the silicon substrate, as observed in Fig.3.8. The particle density is greater than that observed for the 10 µm spin coating and dip coating surface application, as expected with the tape casting technique. The uncoated regions between regions of high density particle occupation are much smaller than the dip coating application. The film thickness is several particle layers thick and appears to be greater than that observed in the other deposition techniques.

From the 10 µm alumina particle SEM images, significant differences are observed relative to the 50 nm particle morphology. Many of the 10 µm alumina particles are shaped like relatively thin platelets shape with two large and flat surfaces. Particles agglomeration is not observed in 10 µm particles which may be due to the fact that van der Waals force is much smaller than the particle weight.

The particle distribution density for both particle sizes could be ranked from low to the highest as dry powder application, dip coating, spin coating and tape casting. Whether it is the 10 μm alumina powders or 50 nm alumina powders, dry powder application gives the lowest powder density on silicon wafer while tape casting application give the highest density. Comparing with 50 nm dry powder application and 10 μm dry powder application, 50 nm dry powders give a higher density because of its smaller size and higher van der Waals force with silicon wafer.

3.12 SEM analysis of CNT forests grown from alumina powder

CNTs are grown on each of the 8 powder size and application technique application combinations as showingn bow. All the CNTs are grown using the floating catalyst chemical vapor deposition (FC-CVD) method. The catalyst solution is ferrocence ($C_{10}H_{10}Fe$) dissolved in xylenes at a ratio of 10% wt. The growth temperature is 750℃ and growth time is 1 hour. To better understand the mechanism of CNTs grown on powders and the sturctures of CNTs on powders, all the 8 different samples are scanned by SEM. Note that the silicon substrate with native oxide itself does not support robust CNT growth, so the CNTs observed are a direct result from growth originating from the alumina powder alone.

CNT Growth from 50 nm Alumina Powder Applied by Dry Adhesion

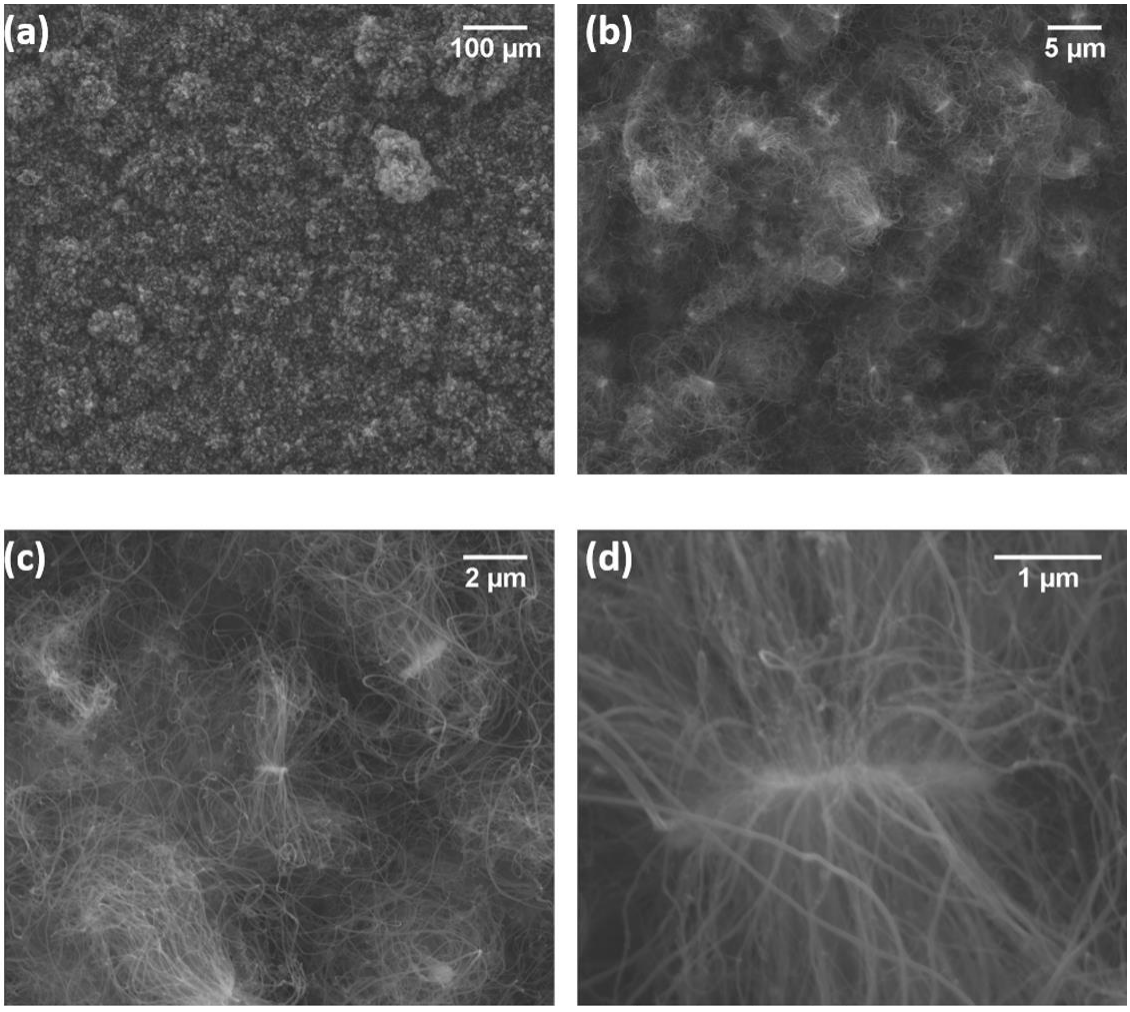

Fig 3.9 Representative SEM images CNTs grown from 50 nm alumina powder dispersed by the dry adhesion method. CNTs are observed to grow from powder aggregates from every surface. (a) Colonies of CNTs are observed to originate uniformly from the substrate. (b) CNT forests originate from alumina aggregate particles, pushing the alumina particles upward away from the substrate. (c-d) The high density of CNTs from each aggregate particle is more clearly observed at greater magnification.

CNT Growth from 50 nm Alumina Particles Applied by Spin Coating

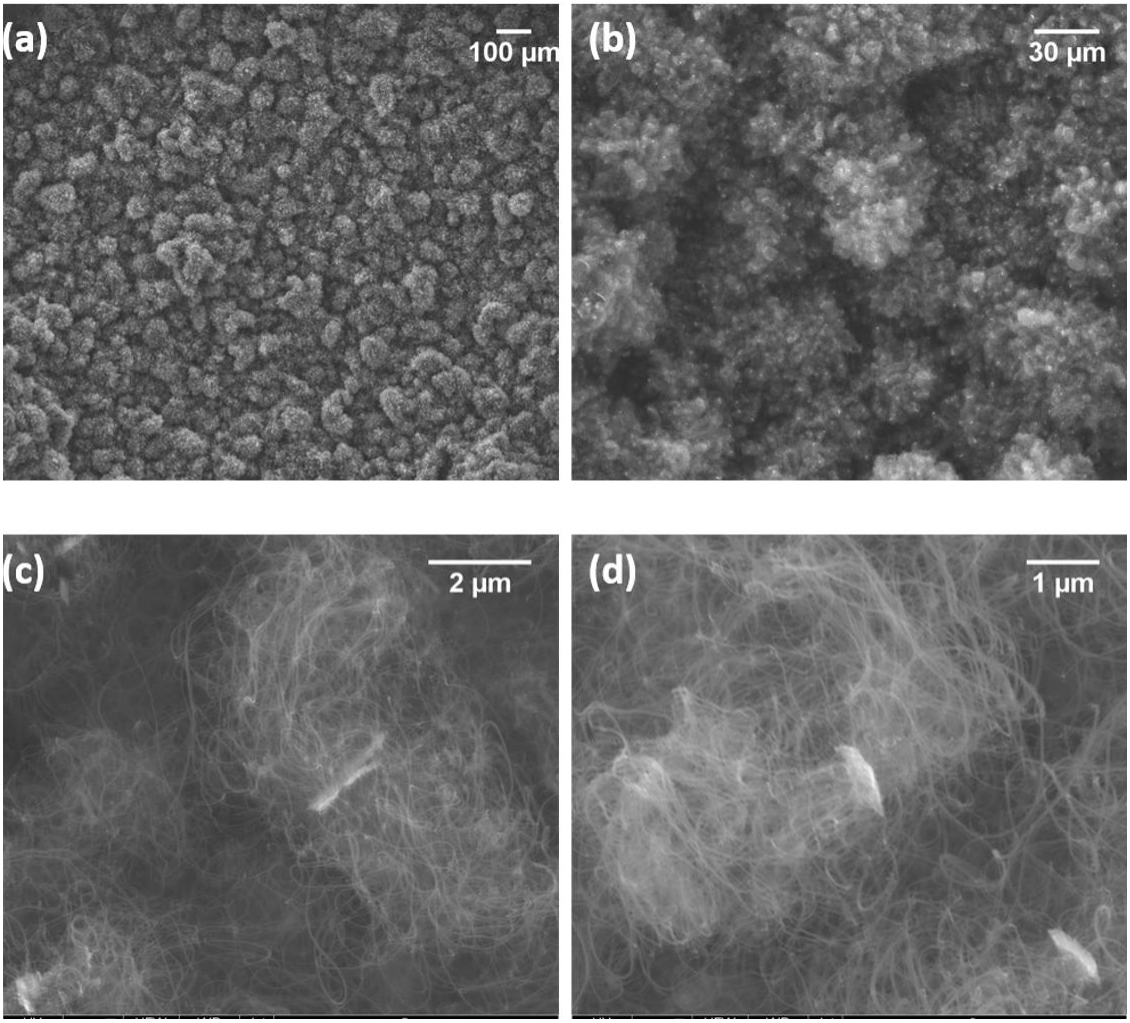

Fig 3.10 Representative SEM images CNTs grown from 50 nm alumina powder dispersed by the spin coat method. (a) Densely populated CNT colonies of various heights are observed. (b) CNT colonies originate from alumina particles. (c-d) High magnification images show that the alumina particle agglomerates form thin platelets with a representative size between 1-2 microns.

CNT Growth from 50 nm Alumina Particles Applied by Dip Coating

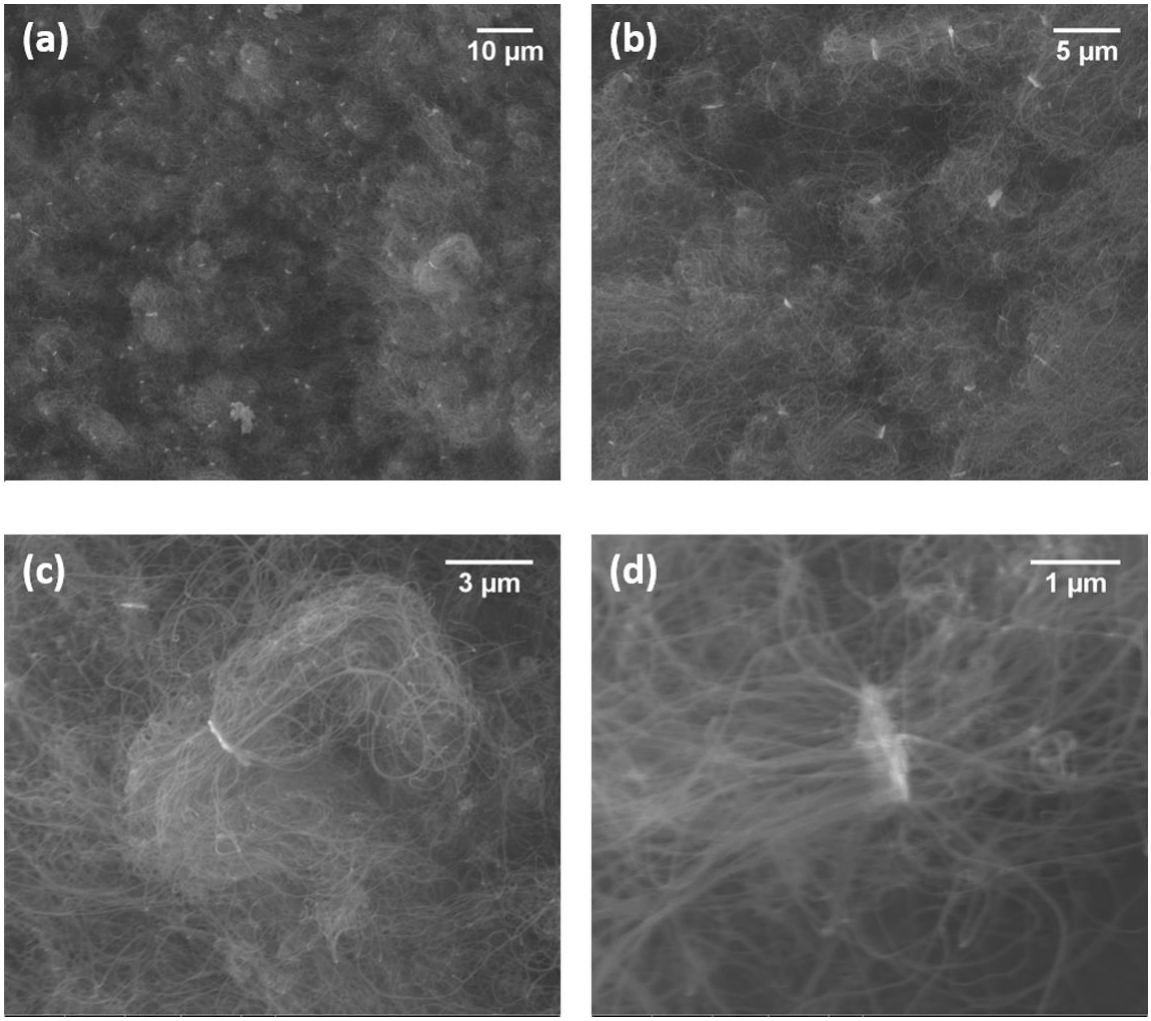

Fig 3.11 Representative SEM images CNTs grown from 50 nm alumina powder dispersed by the dip coat method. (a) Densely populated CNT colonies are observed. (b) CNT colonies originate from aggregated alumina particles. (c-d) High magnification images show that the alumina particle agglomerates form thin platelets with a representative size between 1-2 microns.

CNTs Growth from 50 nm Alumina Particles Applied by Tape Casting

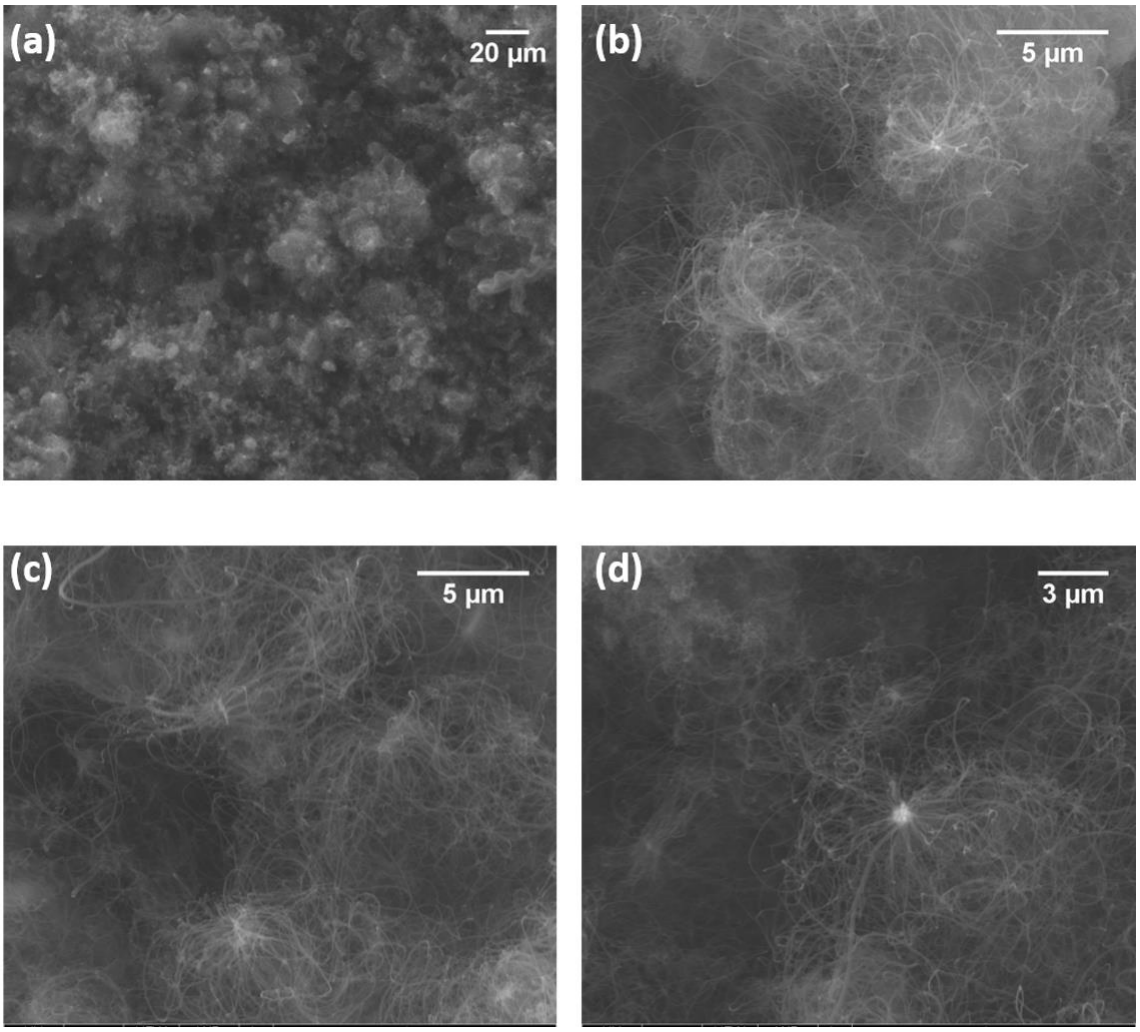

Fig 3.12 Representative SEM images CNTs grown from 50 nm alumina powder dispersed by the tape casting method (a) where densely populated CNT colonies are observed. (b) CNT colonies originate from aggregated alumina particles. (c-d) High magnification images show that the alumina particle agglomerates form thin platelets with a representative size between 1-2 microns.

SEM images of 50 nm alumina-CNTs are shown in Fig. 3.9-3.12. CNTs fill the entire substrate after growth, with non-uniform height. From the SEM images we could find that the alumina particles are lifted from the silicon substrate during the CNTs growth.

Numerous CNTs are synthesized from each alumina particle. Small-diameter alumina particles and larger particle agglomerates particles are observed after CNT synthesis, though alumina particle agglomerates are generally 2 μm or smaller. The CNT colonies are densely populated. In high magnification images we could find that every surface of an alumina particle support CNT growth. In many instances, the alumina particle agglomerates form thin platelets with a representative size between 1-2 microns. The length of each CNT could not be directly measured in the SEM images because of the complex 3-D nature of the growth, but could be estimated that most CNTs have a length between 10-20 μm.

It is difficult to distinguish between CNTs grown from the different alumina application techniques by SEM. For each powder application method, CNTs grow from agglomerated alumina particles. The agglomerated alumina particles tend to form thin platelets with a characteristic width of approximately 1-2 μm. CNTs grow from all surfaces of the particle, propelling the alumina particle away from the substrate. It is difficult to ascertain if substrate-bound alumina particles exist and if they support CNT growth, although most CNTs seem to originate from observed alumina particle agglomerates that are lifted from the silicon support substrate. In this mechanism the CNT forests form a shape that fan out from a central particle to form a shape similar to a galaxy where alumina particles are the center, and CNTs grow around each particles.

SEM EDS of 50 nm Alumina-CNTs

In SEM, Energy Dispersive Spectroscopy (EDS) is a tool that identifies the elements present in a sample by analyzing the X-rays generated by the interaction between

the electron beam of the SEM and the sample. Since X-rays are only generated from the area of the surface excited by the small electron beam, spectra of individual areas or particles can be obtained. Spectral information can therefore be generated for an entire field of view by scanning the beam, providing an elemental map. This elemental mapping technique allows us to immediately visualize the chemical landscape in our CNT samples. With EDS mapping, the element in our alumina-CNTs are distinguished and mapped below in Figure 3.13--3.15.

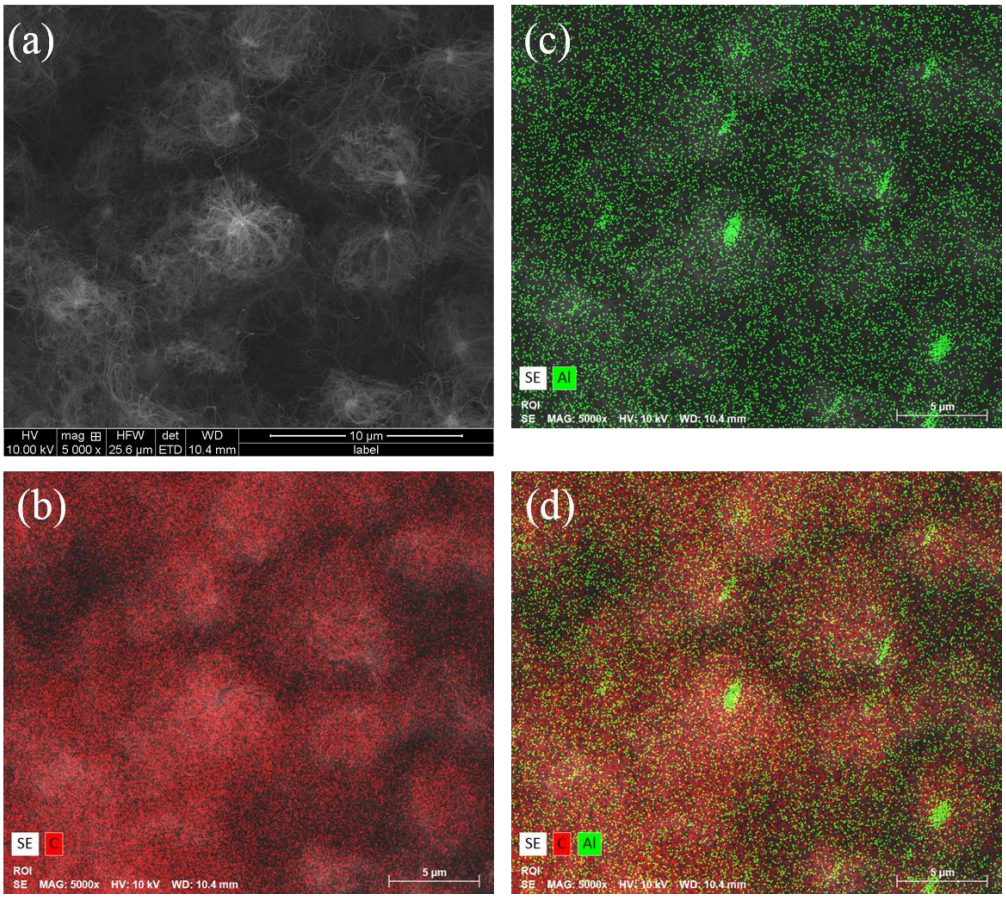

Fig 3.13 EDS mapping image of 50 nm alumina-CNTs (a) SEM images before EDS mapping. (b) carbon mapping of whole image; (c) aluminum mapping of whole image; (d) carbon and aluminum mapping of whole image. The regions of alumina particles and CNTs could be clearly distinguished in the map.

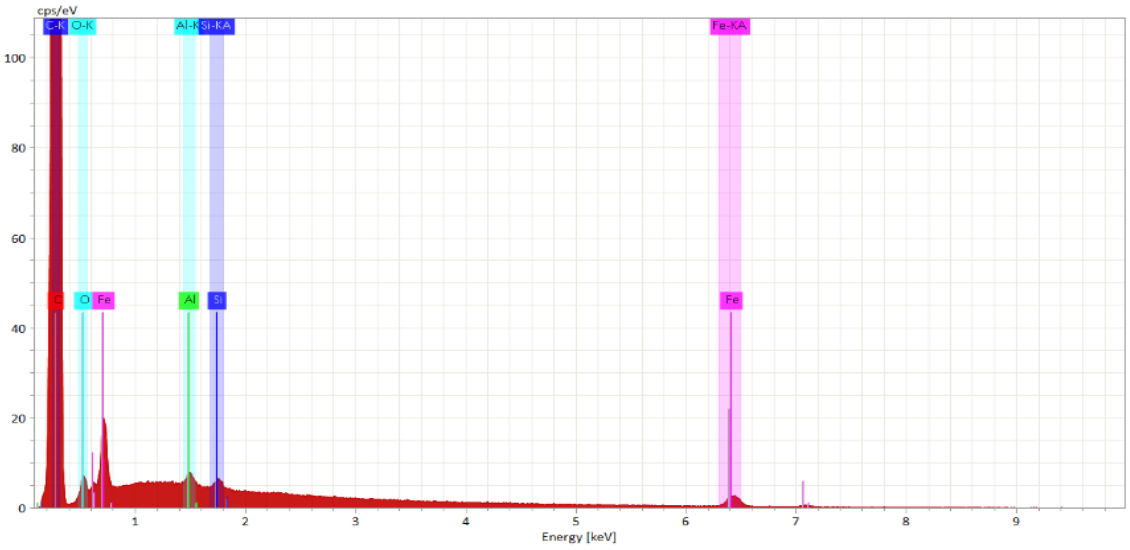

Fig 3.14 EDS spectra of the area scanned in fig 3.13. Carbon (from CNTs) and aluminum (from alumina particles) are clearly present on the sample. Additionally, Fe and Si are observed from the catalyst particles and support substrate, respectively.

In Fig 3.13 & 3.14, an area of horizontal field width (HFW) 25.6 µm are scanned and mapped by SEM EDS. From Fig 3.14(a), 10 alumina-CNTs colonies were observed. The SEM EDS shows the carbon mapping in Fig 3.14(b) and aluminum mapping Fig 3.14(b). Background levels of aluminum is found in trace concentrations everywhere in this area, but 10 distinct locations with high concentrations of alumina are observed that correspond to alumina support particles. The background aluminum is likely from the alumina-CNTs underlying the bottom layer. Combining the carbon mapping and aluminum mapping together, shown in Fig 3.14(d), the alumina-CNTs structure could be clearly distinguished, which is a shape similar to a galaxy where alumina particles are the center, and CNTs grow around each particles.

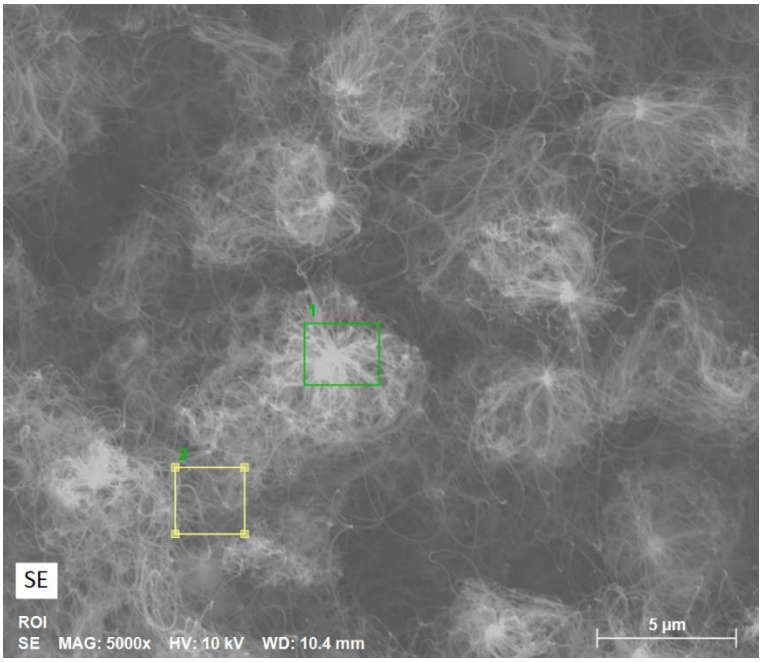

Fig 3.15 SEM image of alumina-CNTs and the spot where is be scanned is marked as area 1 and area 2.

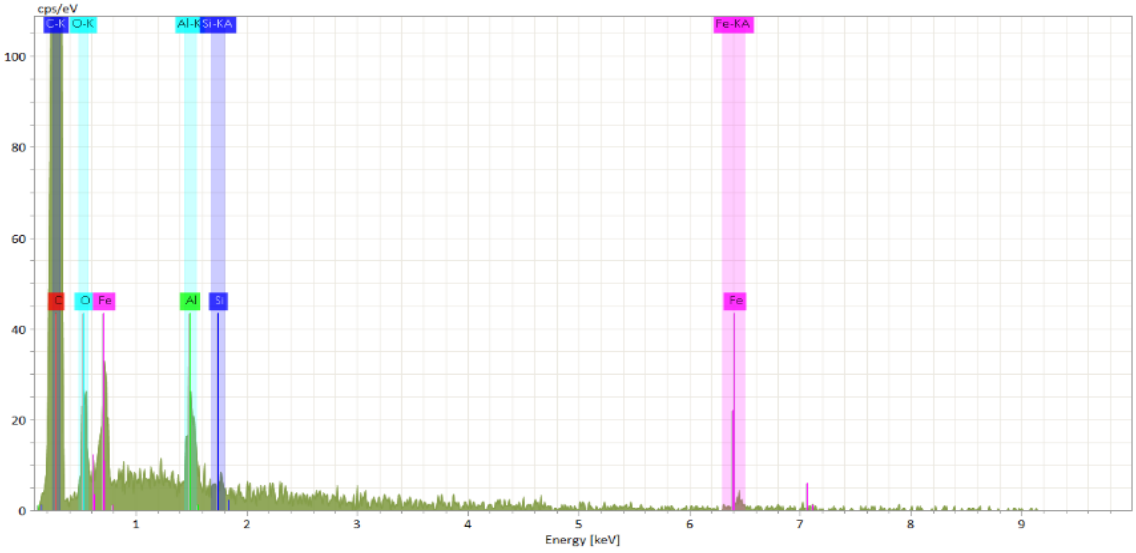

Fig 3.16 EDS spectra of area 1 (containing CNTs and a bright particle). A high concentration of both carbon and aluminum are observed in this area.

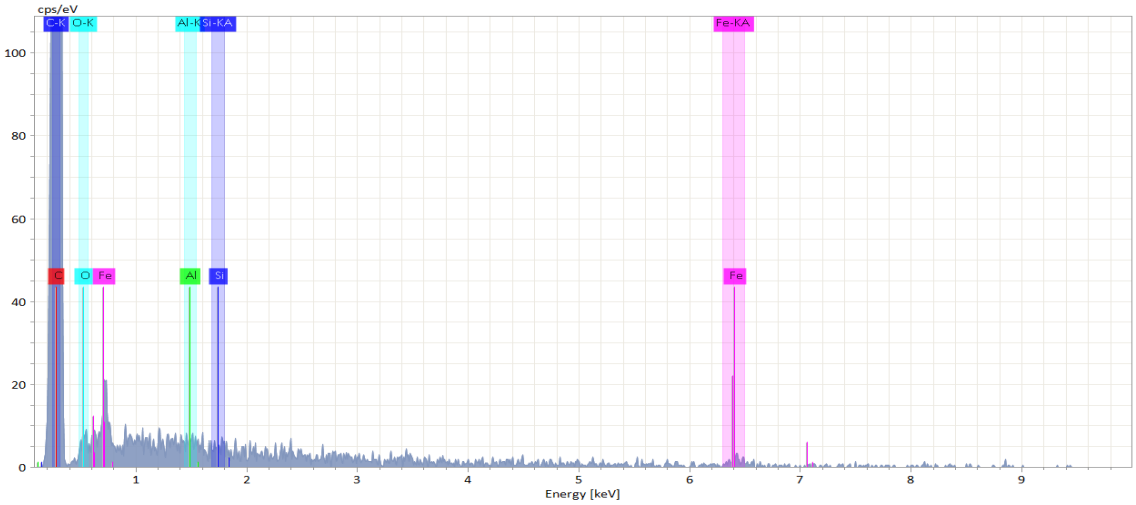

Fig 3.17 EDS spectra of area 2 (CNT area). A high carbon concentration is found with only background levels of aluminum.

Figure 3.16 & 3.17 shows the EDS spectra collected from area 1 and area 2 in Fig 3.15. Area 1 represents a region near the alumina particle from which CNT growth is supported. Area 2 is away from the support particle in a region of high-density CNT growth. Region 1 shows a high concentration of both aluminum, carbon, and oxygen. Aluminum and oxygen originate from the alumina support particle, while carbon is from CNTs. In region 2, no alumina particle is observed. In this region, an obvious decrease of aluminum and oxygen is observed relative to area 1. Iron is present in both area 1 and area 2 since it is the CNT catalyst. Traces of silicon originate from the support substrate.

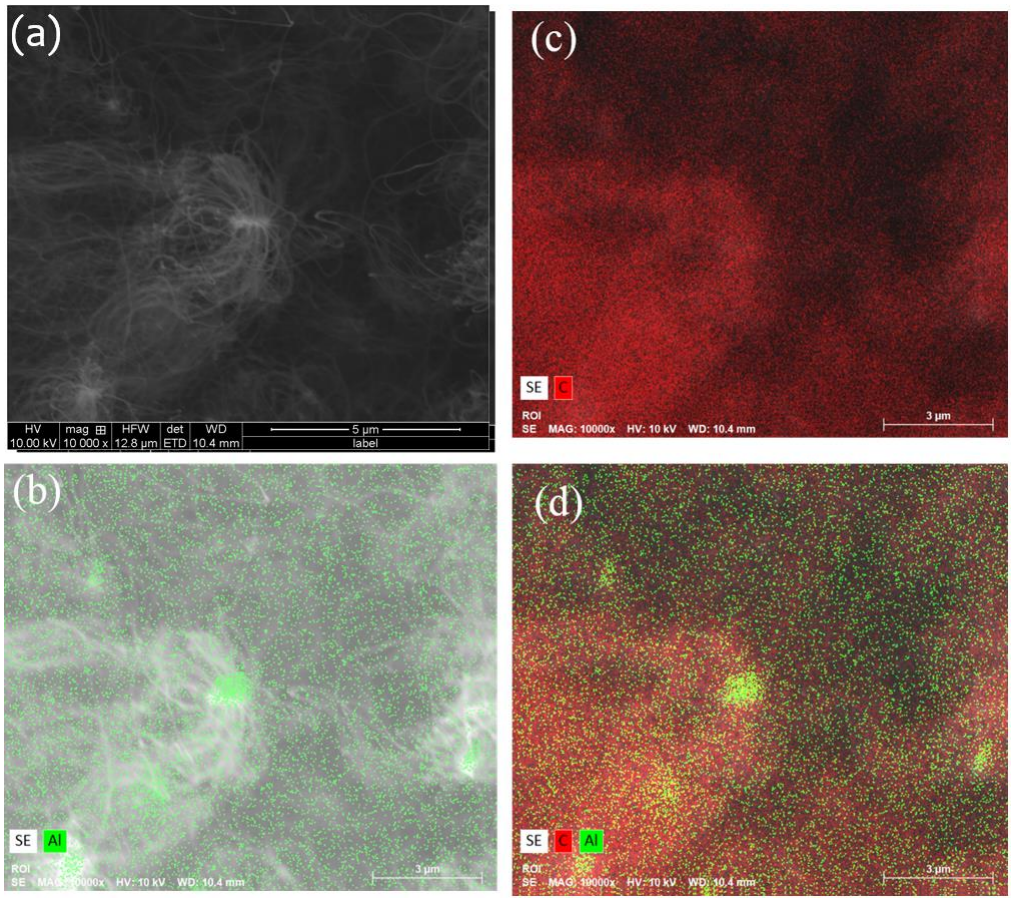

Fig 3.18 EDS mapping image of a single 50 nm alumina-CNTs colony (a) SEM images before EDS mapping. (b) Carbon mapping of whole image. (c) Aluminum mapping of whole image.(d) Carbon and aluminum mapping of whole image. The shape alumina-CNTs could be distinguished in the map.

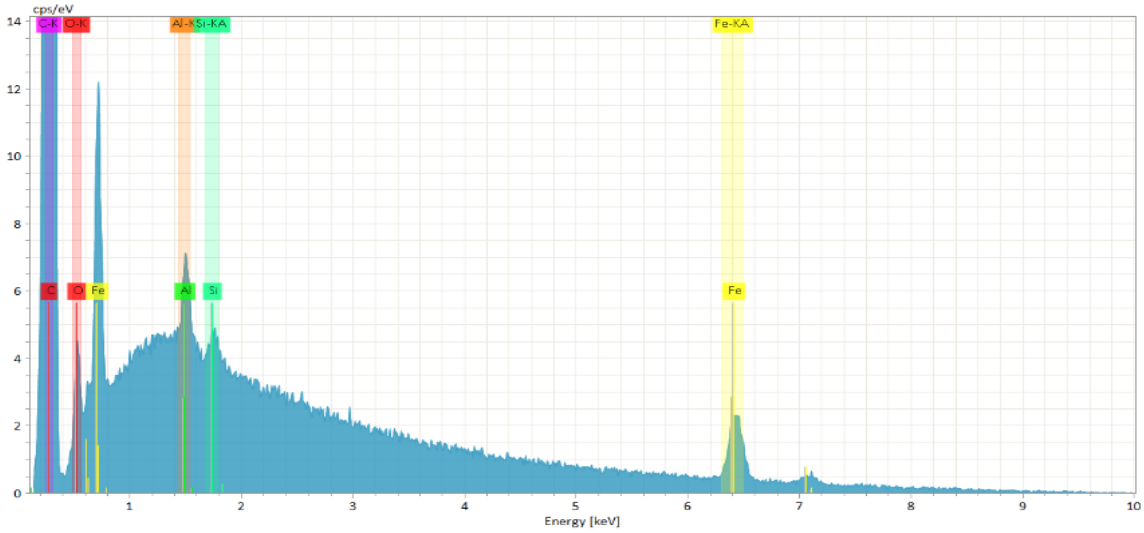

Fig 3.19 Overall spectra of the area scanned in Fig 3.18. The concentration of carbon and aluminum are clearly observed.

Fig 3.18 and 3.19 show the EDS mapping and spectra of a single 50 nm alumina-CNTs colony. The shape and structure of a single 50 nm alumina-CNTs were clearly shown by the EDS mapping the carbon and aluminum element in Fig 3.18 (b) and (c). The overall spectra of this area shows a high carbon, aluminum, and iron content which correspond to the carbon nanotubes, support, alumina, and the catalyst, respectively.

CNT Growth from 10 μm Alumina Particles Applied by Dry Adhesion

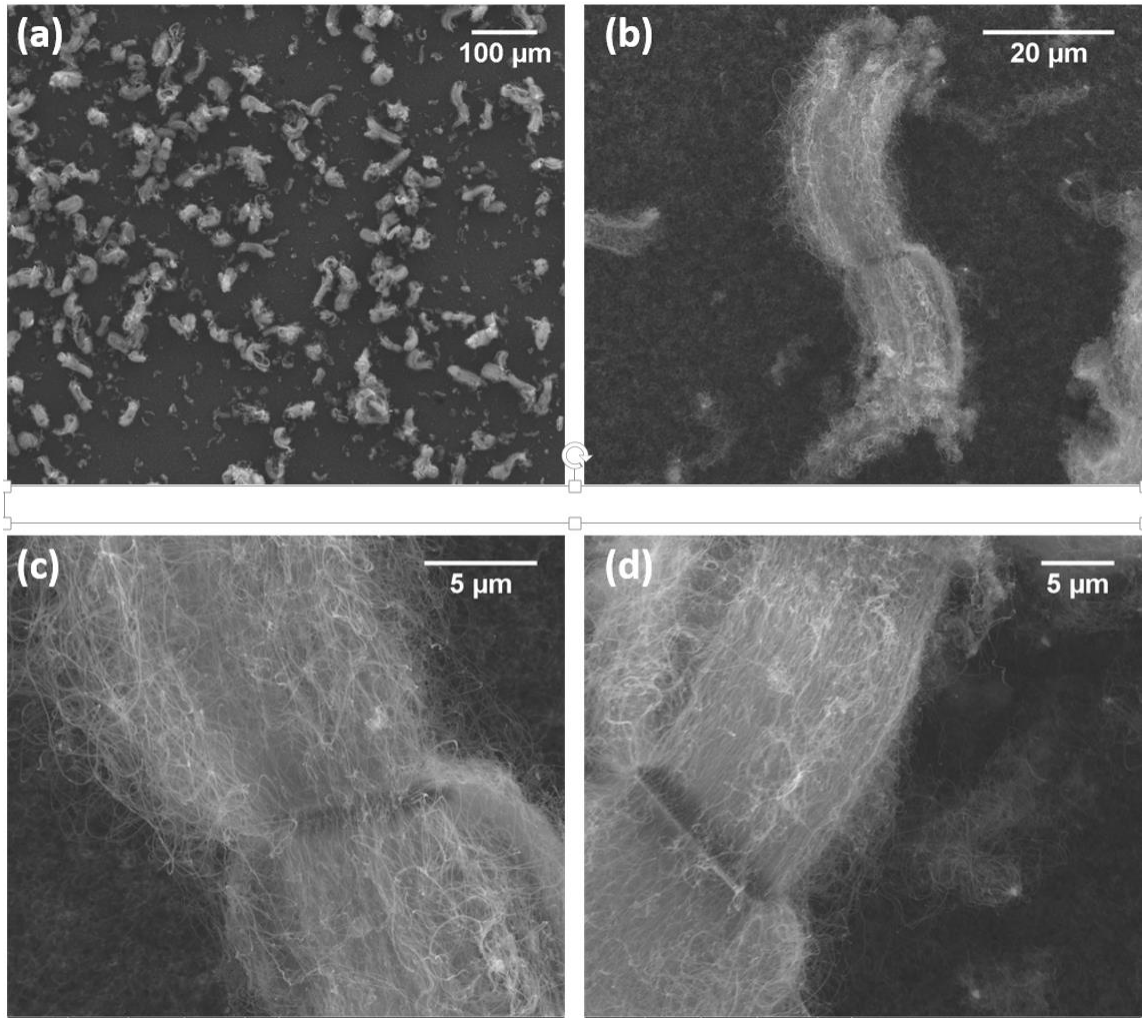

Fig 3.20 Representative SEM images CNTs grown from 10 μm alumina powder dispersed by dry adhesion (a) Sparse clusters of CNT growth are observed on the silicon substrate. (b) CNT forests originate from the isolated alumina particle along preferred orientations. (c-d) High magnificent images show the relatively high density of small-diameter CNTs originating from the central alumina particle.

CNT Growth from 10 μm Alumina Particles Applied by Spin Coating

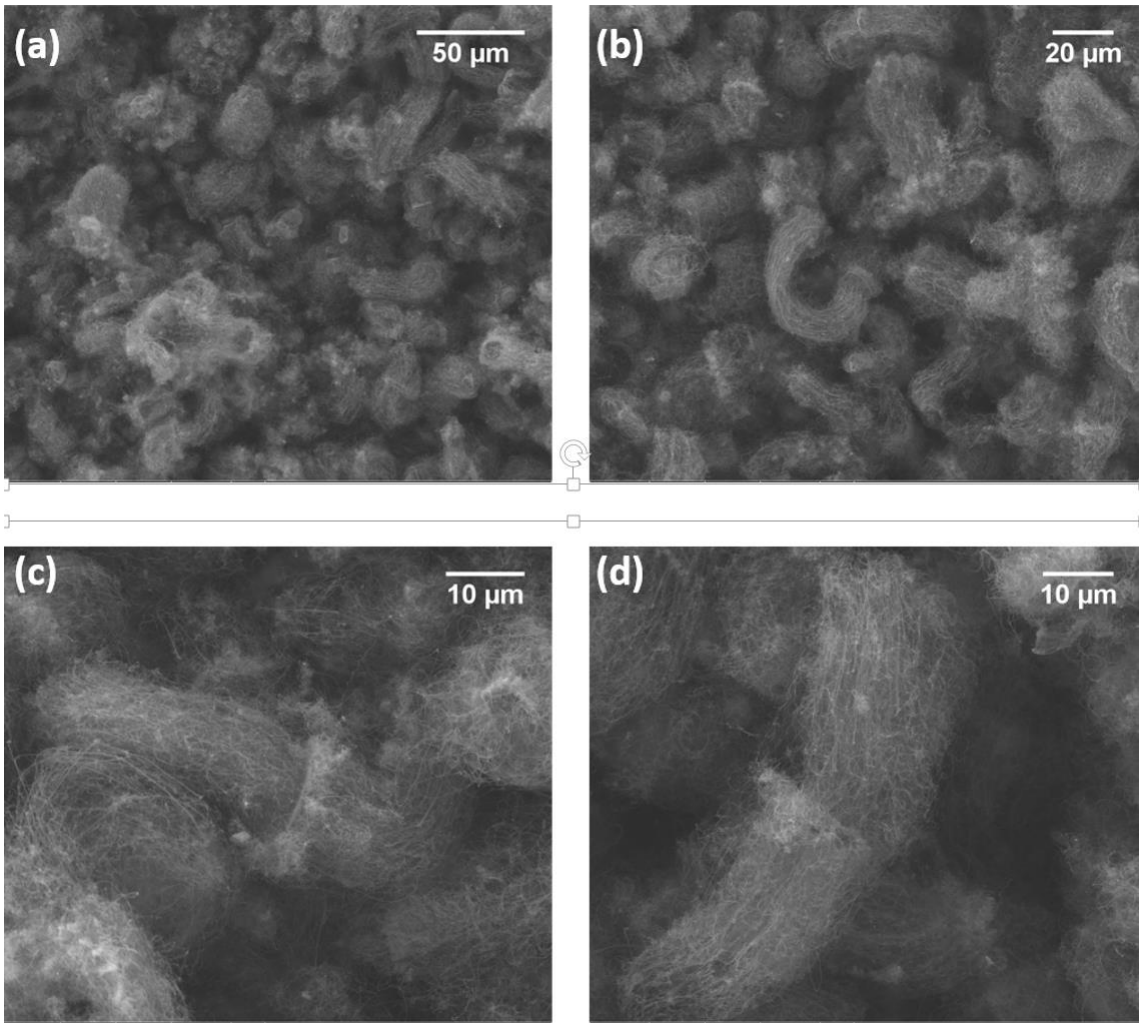

Fig 3.21 Representative SEM images CNTs grown from 10 μm alumina powder dispersed by spin coating. (a-b) A high density of oriented CNT forest clusters are observed residing on the silicon substrate (cd) High magnification images show the general alignment and density of CNTs originating from the central alumina particle.

CNT Growth from 10 μm Alumina Particles Applied by Dip Coating

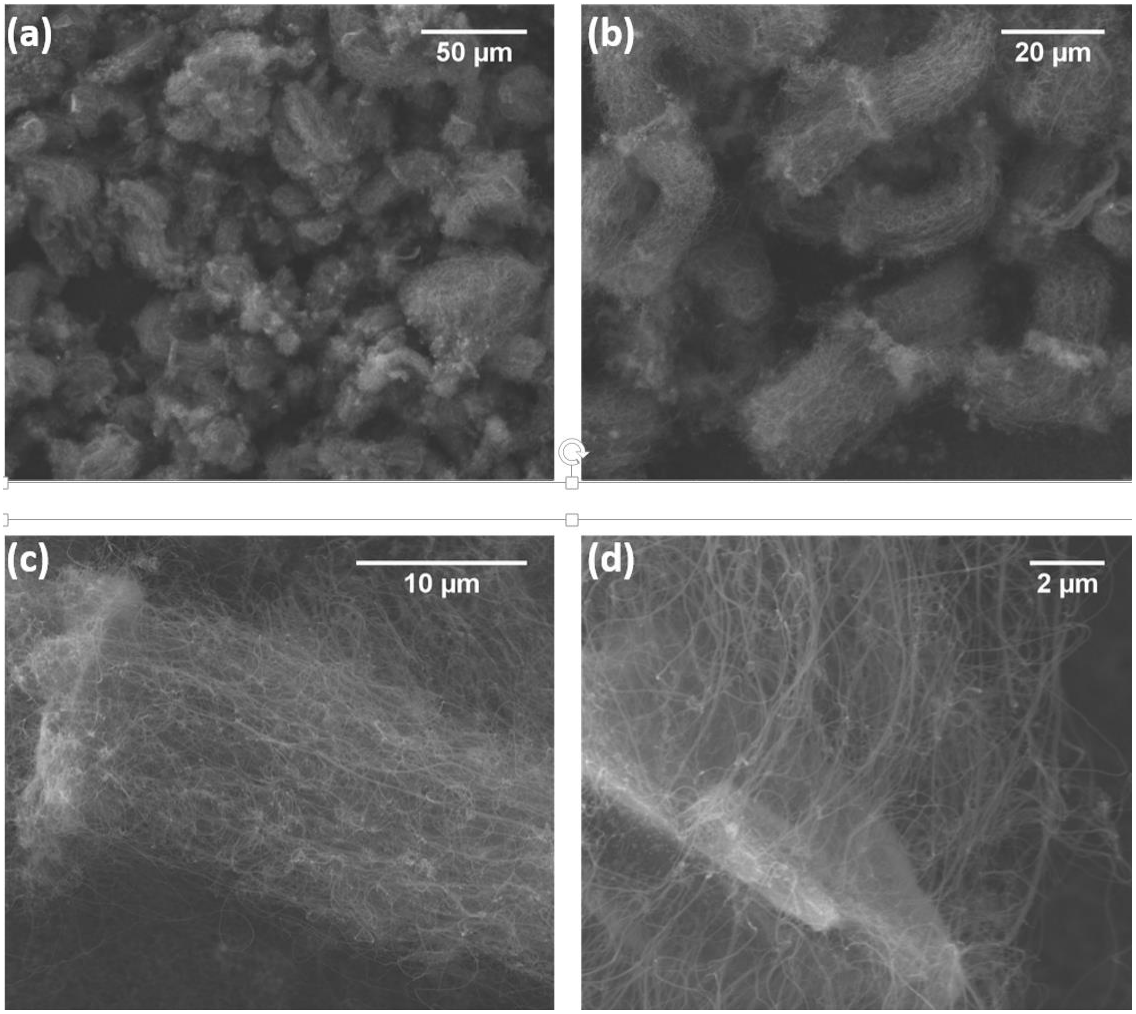

Fig 3.22 Representative SEM images CNTs grown from 10 μm alumina powder dispersed by dip coating. (a-b) Low magnification shows a high density of highly aligned CNT colonies, which each colony originating from a central particle. (c-d) High magnification images reveal that CNTs originate from all faces of the alumina particle, including the thin edges.

CNT Growth from 10 μm Alumina Particles Applied by Tape Casting

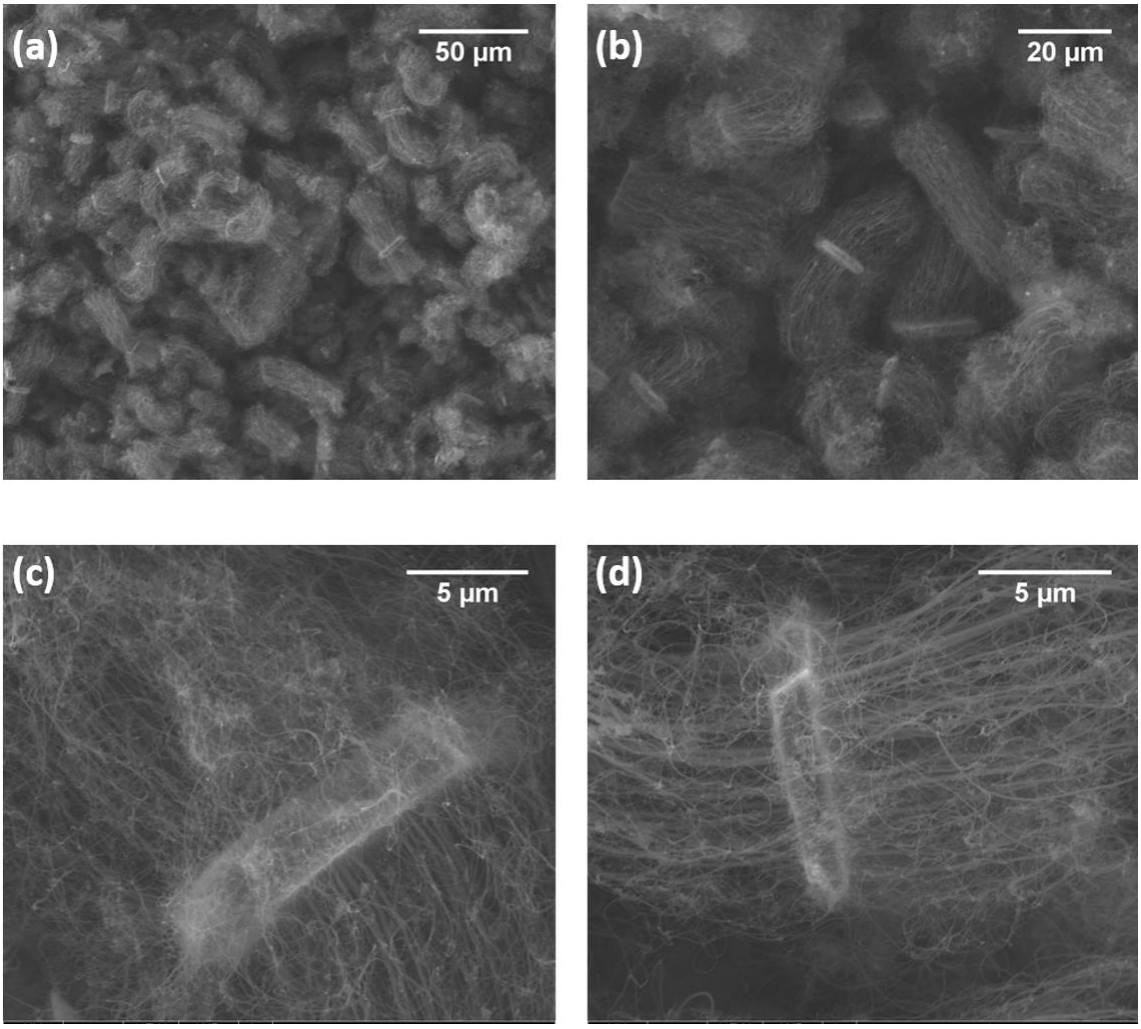

Fig 3.23 Representative SEM images CNTs grown from 10 μm alumina powder dispersed by tape casting. (a-b) Low magnification shows a high density of highly aligned CNT colonies, which each colony originating from a central particle. (c-d) High magnification images reveal that CNTs originate from all faces of the alumina particle, including the thin edges.

SEM images of 10 μm alumina-CNTs are shown in Fig. 3.20—3.23 from the dry powder, dip coating, spin coating, and to tape casting surface application techniques. Similar to the 50 nm alumina particles, the alumina particles are displaced during the CNTs growth. Unlike the 50 nm alumina particles, individual alumina particles (rather than

particle agglomerates) support CNTs growth. Alumina-CNT clusters are distributed at a high density on the silicon. In low magnification images we could see that most CNTs originate from the two large, flat surfaces of each alumina platelet, with a CNT length of 20—30 μm in both side of alumina platelet. The high magnification images show that CNTs originate from all faces of the alumina particle, including the thin edges.

Compared to the 50 nm alumina-CNTs, the CNT forests growing from the 10 μm alumina particles have a different morphology. Although CNTs grow on all the surface of alumina particles, the 10 μm alumina particles have two large and relatively flat surfaces that are 10 times longer than the width of the particle. As most of aligned CNTs grow normal to the two large surfaces, the 10 μm alumina-CNTs have a shape of caterpillar which is a long and narrow with a length of 40—60 μm and width of 10 μm. From the 10 μm dry powder application, we could see that each alumina particle supports CNTs growth, but for other three surface applications, it is hard to tell if all alumina particles uniformly support CNTs growth since some alumina particles are hidden under the surface.

EDS mapping of 10 μm alumina-CNTs

SEM EDS mapping is applied to the 10 μm alumina-CNTs colonies, results are shown in figures below.

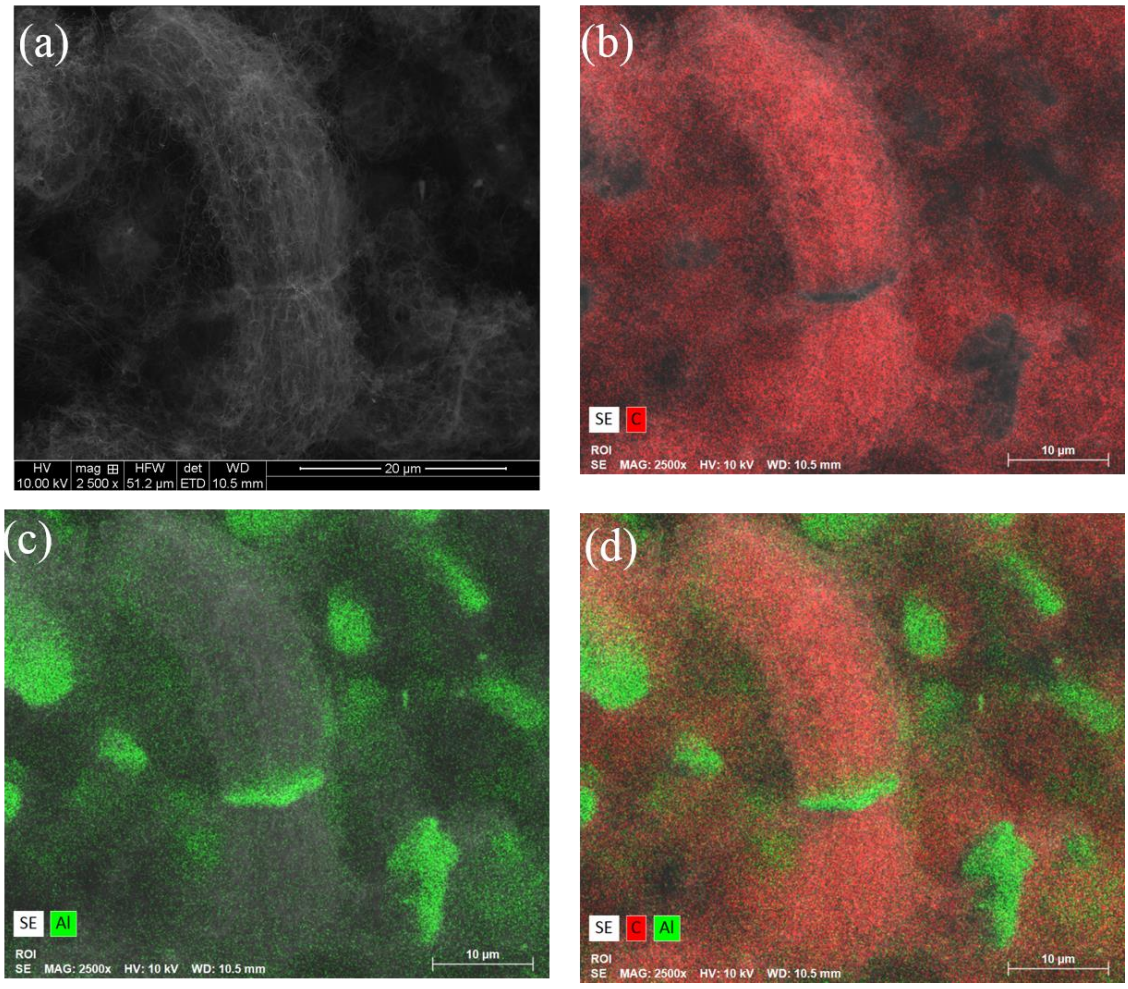

Fig 3.24 EDS mapping image of a 10 μm alumina-CNTs colony (a) A10 μm alumina-CNTs colony SEM image before EDS mapping. (b) Carbon mapping of whole image. (c) Aluminum mapping of whole image. (d) Carbon and aluminum mapping of whole image. The shape of the alumina CNTs could be distinguished in the map.

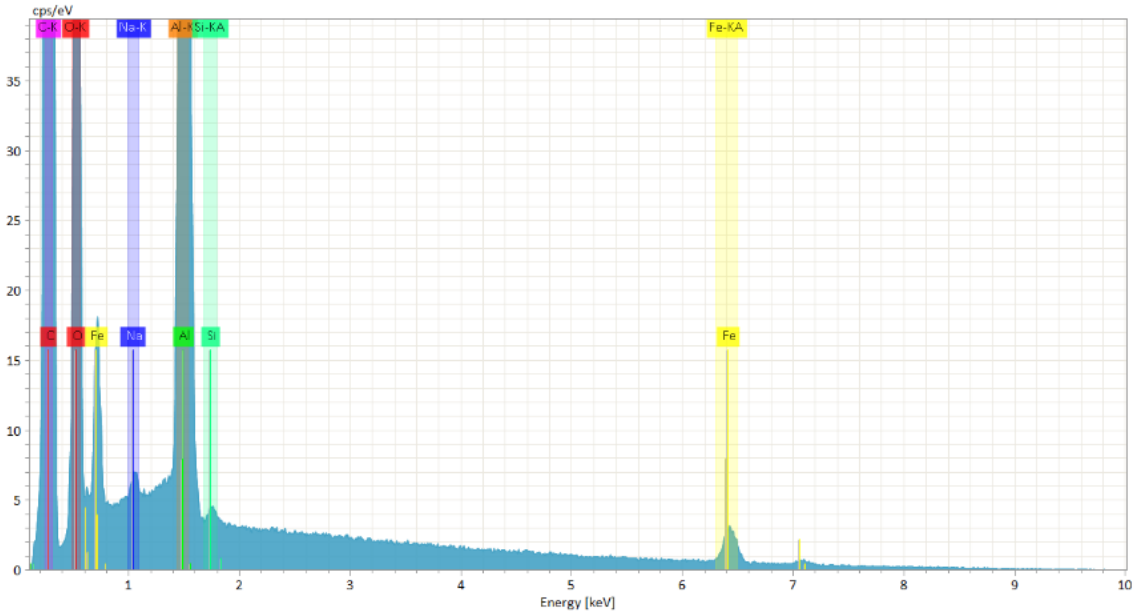

Fig 3.25 Overall EDS spectra of area shown in Fig 3.24

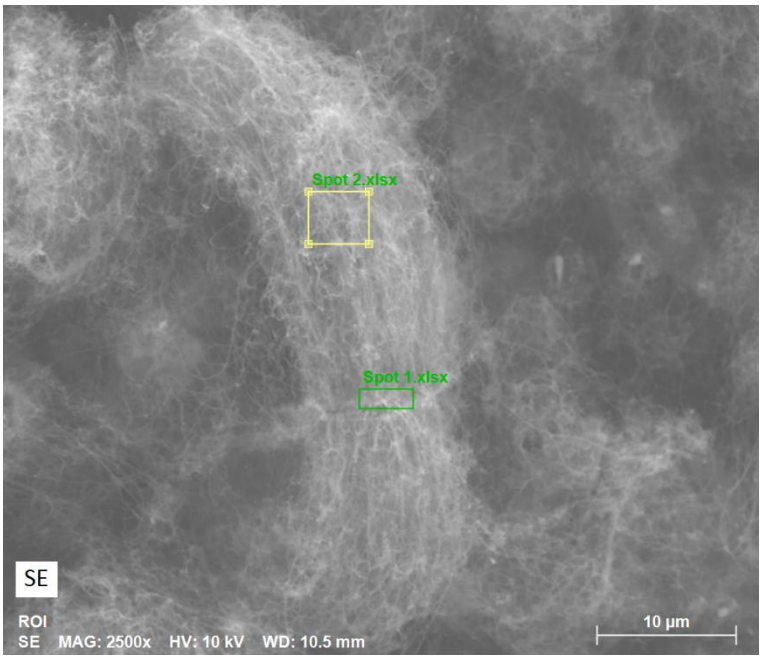

Fig 3.26 SEM image of alumina-CNTs. EDS spectra were obtained in area 1 and area 2.

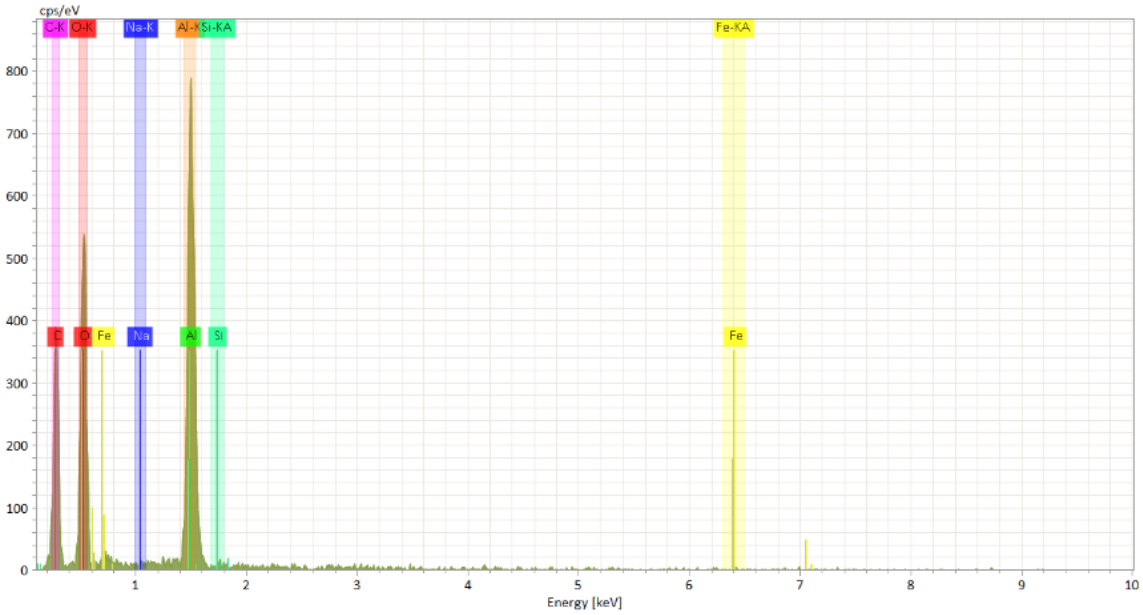

Fig 3.27 EDS spectra of area 1. High aluminum and carbon concentration were shown in this area.

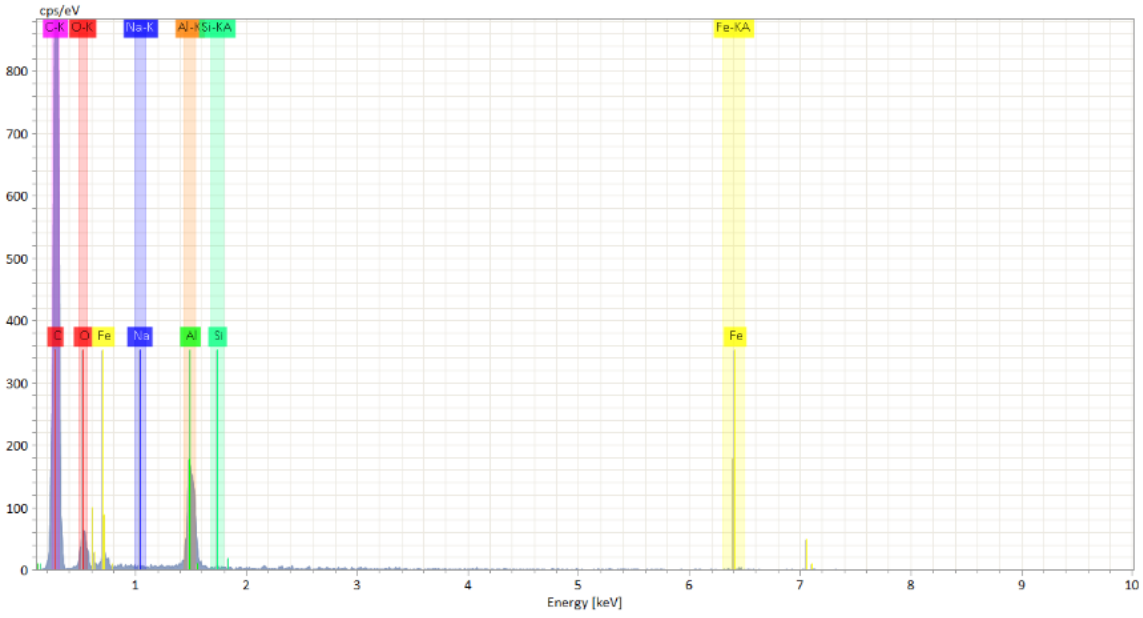

Fig 3.28 EDS spectra of area 2. High carbon and aluminum concentration were found in this area, although carbon is found in significantly higher concentration.

EDS mapping and spectra is applied to a single 10 μm alumina-CNT colony and shown in Fig 3.24 to Fig 3.28. The mapping shows the distribution of carbon and aluminum in a single 10 μm alumina-CNTs colony. The EDS spectra of spot 1 and spot 2 in Fig3.26 are also provide information the organization of the CNT forests about the central alumina support particle. Fig 3.24 shows that alumina particles found in the middle of the CNT colonies have a similar structural appearance as the bare particles before CNTs growth. A alumina-CNTs structure could be draw out, which is a shape similar to a caterpillar where alumina particles are the center, and CNTs grow around each particles with a long and wide shape. Concentrated alumina spot was found in the background area, which means more alumina-CNT particles reside behind the central colony which are difficult to observe by SEM alone. Aligned CNTs are grown on the small alumina platelet with a length of 30 μm. From Fig 3. 26—3.28, the spectra of area 1 and are 2 demonstrate that area 1 has a high alumina concentration while area 2 has lower alumina concentration with high carbon concentration. EDS mapping provides a powerful tool to distinguish the population of alumina and CNTs in the CNT colonies.

3.2 TEM Result

Transmission electron microscopy (TEM) is a microscopy technique in which a beam of electrons is transmitted through an ultra-thin specimen, interacting with the specimen as it passes through. An image is formed from the interaction of the electrons transmitted through the specimen. TEMs are capable of imaging at a significantly higher resolution than light microscopes, owing to the small de Broglie wavelength of electrons.

This enables to examine fine detail—even as small as a single column of atoms, which is thousands of times smaller than the smallest resolvable object in a light microscope. TEM used here is FEI Tecnai F30 G2 Twin Microscope with Operating voltages of 100kV to 300 kV and magnification range from 100kX - 440 kX.

TEM allows for the viewing of the internal details of CNTs, such as the hollow structure and the embedded iron particle used as the catalyst. Only dry powder application alumina-CNTs are scanned in TEM. Information about the diameter and width of CNTs wall are obtained from these images.

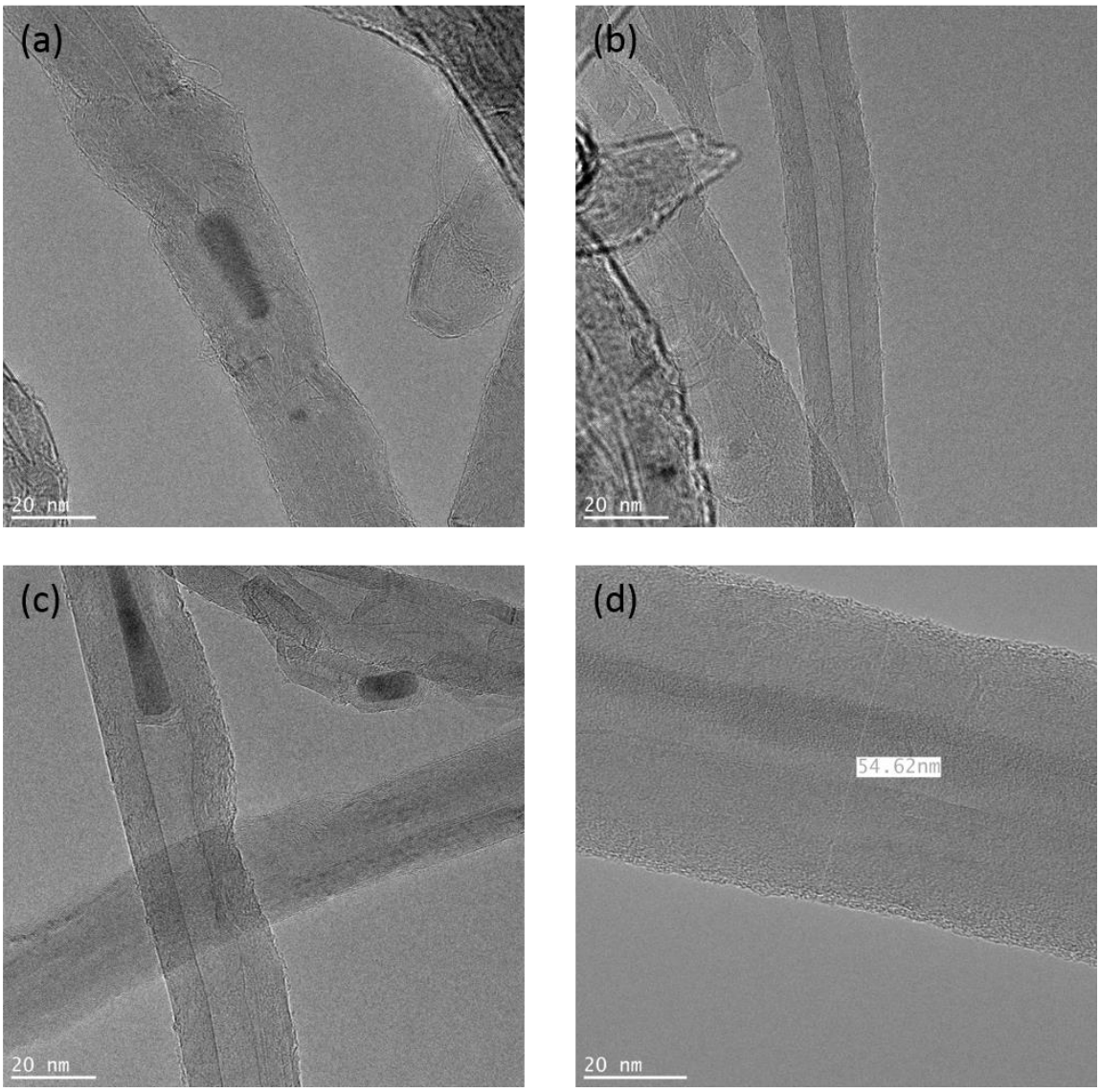

Fig 3.29 TEM image of CNTs produced from 50 nm alumina particles, (a), (c) Iron catalyst were found inside the CNTs tube, (b) shows the CNTs are multi-walled CNTs. (d) The diameter of a single large-diameter CNT is measured and is found to be 54.62 nm.

TEM images of CNTs grown from 50 nm alumina particles are shown in Fig 3.29. As we could see in images, the CNTs synthesized are generally mutli-walled CNTs. No single-walled CNTs or double-walled CNTs were found in these TEM images. Iron catalyst may be found inside CNTs, which manifests as dark particles inside the hollow structure

of CNTs. From these images of CNTs we could also find that the diameter of CNTs are not uniform, the diameter ranges from 20 nm to 60 nm.

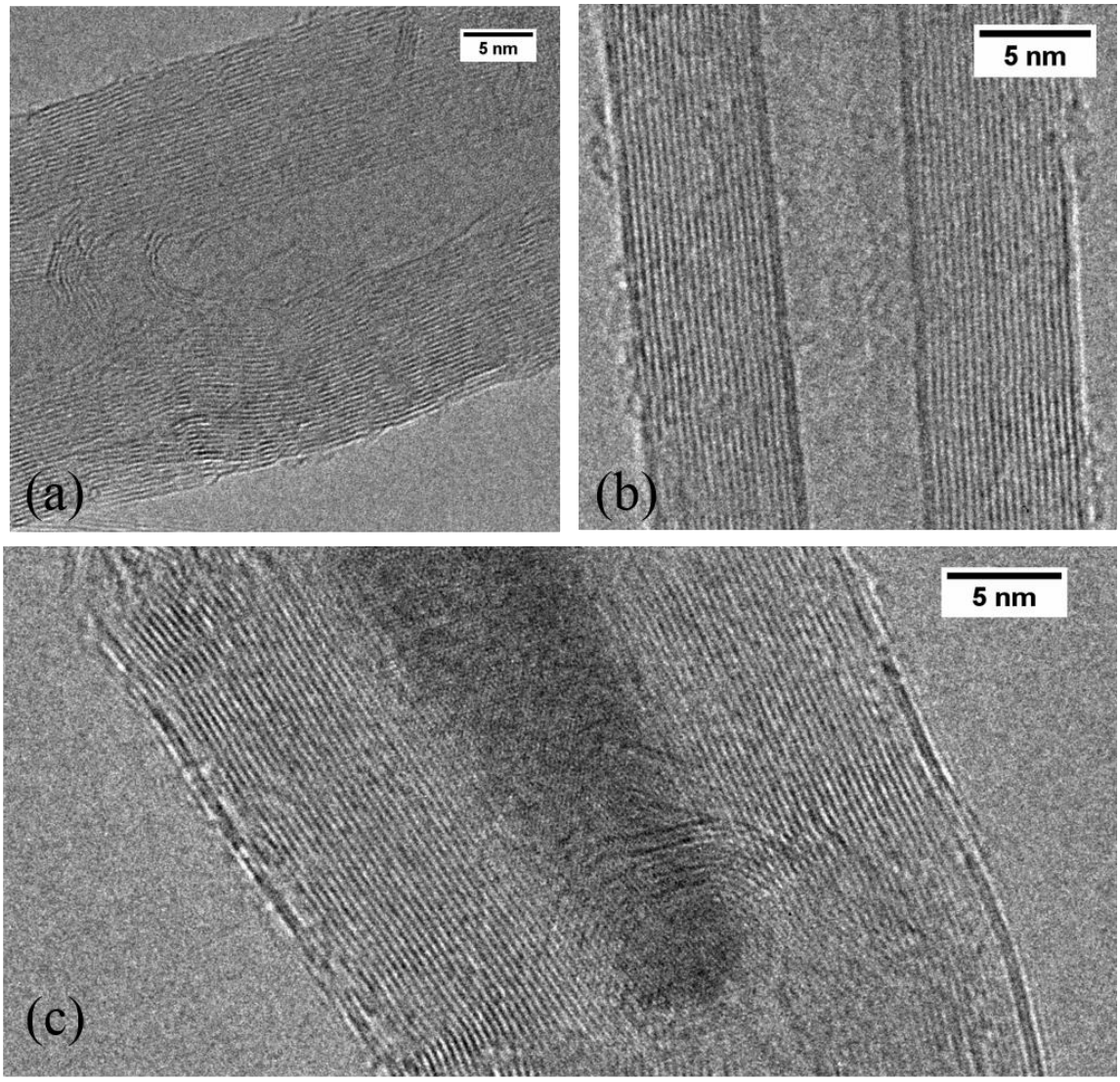

Fig 3.30 Representative high-resolution Bright field TEM images of 50 nm alumina-CNTs. (a-b) TEM images show the CNTs walls and details of the hollow structure, (c) High resolution TEM image show the iron catalyst inside the CNT and walls could be viewed .

Representative high-resolution TEM images of CNTs grown from 50 nm alumina particles are shown in Fig 3.30. Individual CNT walls could be viewed and counted. In Fig 3.30(a) this CNT has 34 walls and the average wall spacing is 0.323 nm, while in Fig

3,30(b) a 20 wall MWCNTs is shown. Fig 3.30(c) shows both the CNT walls and the iron catalyst inside of CNT. These high resolution TEM images gives information of CNT walls and provide the inside structure of CNTs synthesized on alumina particle as a support.

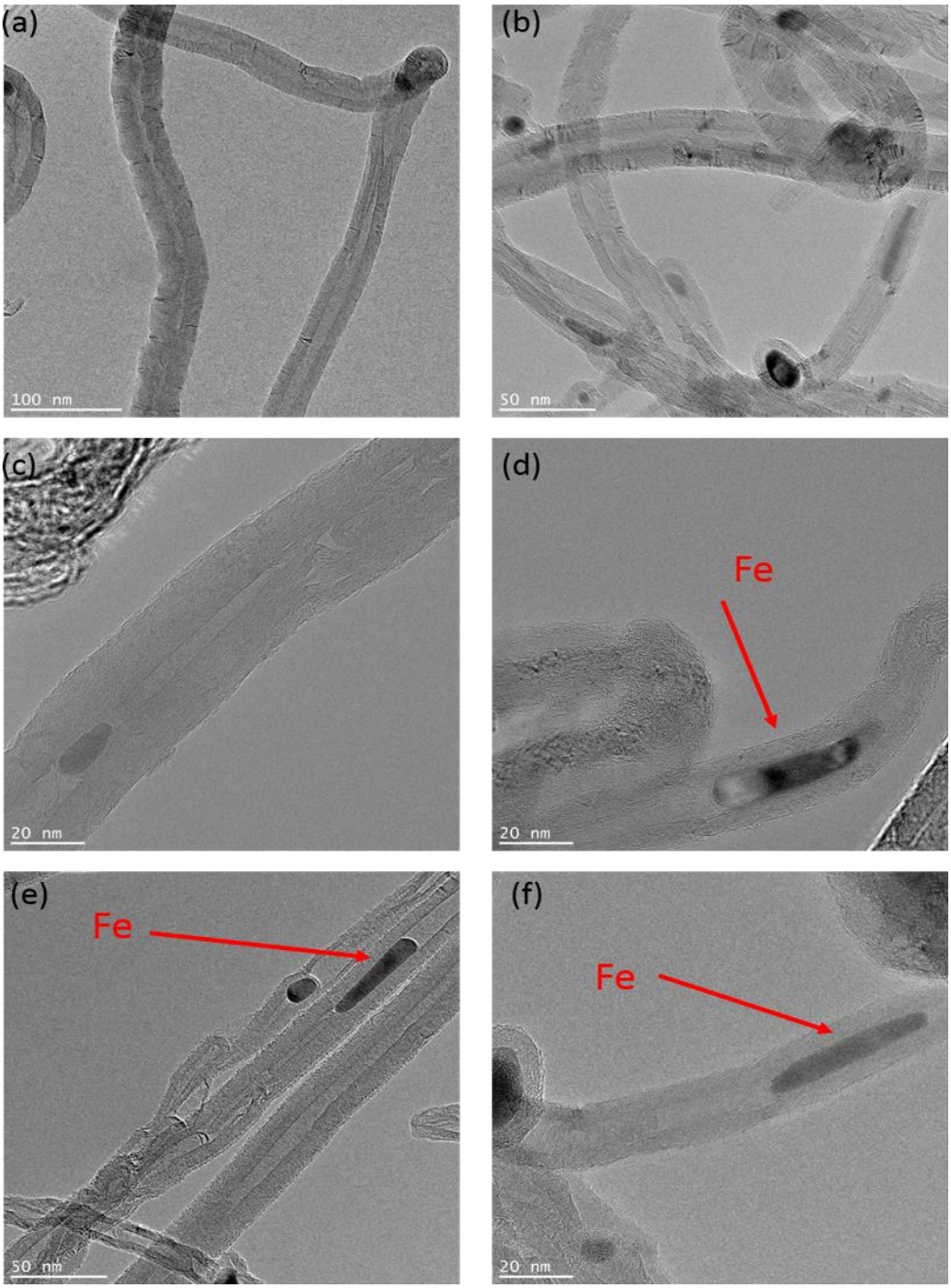

Fig 3.31 Representative high resolution TEM images of CNTs grown from 10 µm alumina particles. (a-b) show the CNTs bending when growth and its multi-walls structure. (c) The CNT walls and iron catalyst may readily be observed. (d-f) Further examples of iron catalyst inside CNTs.

Fig 3.31 shows the high resolution TEM images of CNTs grown from 10 µm alumina particles. The CNTs produced are similar to those produced using 50 nm alumina particles. No SWCNT or DMCNTs were found using TEM.

The diameter of multiple CNTs grown from both 50 nm and 10µm alumina particles are measured using TEM micrographs using ImageJ analysis software. Diameter distributions are obtained from both of them are shown below in Figures 3.32 & 3.33. The sample size of 46 measurements was obtained from the CNTs grown from 50 nm alumina particles. The average diameter is 29.03 nm with a standard deviation of 8.4 nm. A population of 68 measurements were obtained from CNTs originating from 10 µm alumina particles. The average diameter of these CNTs is 24.41 nm with a standard deviation is 8.5 nm. The data collected from the diameter distribution suggests that CNTs grown from 50 nm alumina particles have a slightly larger diameter than those grown from 10 µm particles.

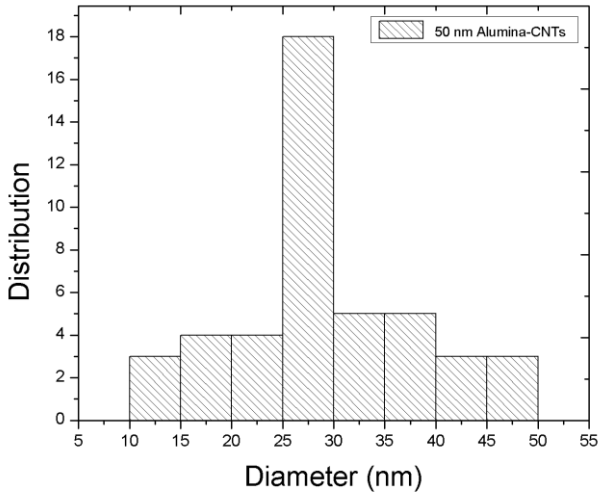

Fig 3.32 Diameter distribution of CNTs grown from 50 nm alumina particles.

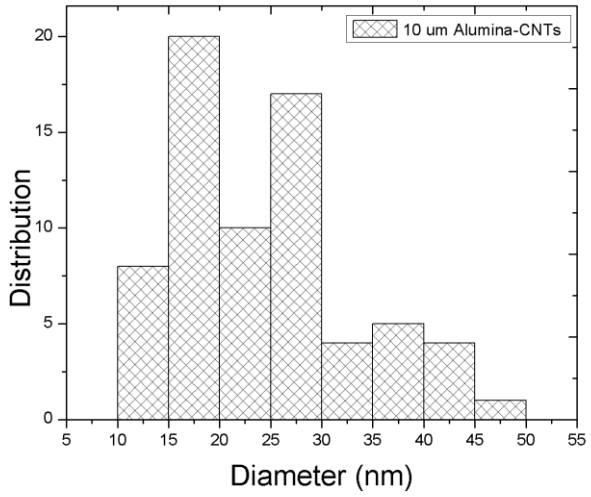

Fig 3.33 Diameter distribution of CNTs grown from 10 μm alumina particles.

Energy-dispersive X-ray spectroscopy (EDS) is an analytical technique used for the elemental analysis or chemical characterization of a sample. In TEM, EDS can be used to find the chemical composition of materials down to a spot size of a few nanometers and to create element composition maps over a much broader raster area. To fully prove the particle inside of CNTs hollow structure is the catalyst-iron, EDS is used to analysis the element of the material. In Figure 3.34 the particle inside CNTs is obviously proved to be iron—the catalyst we used for CNTs growth, and it was marked as red color in the elemental map shown in Figure 3.35(c). Element carbon is not marked since all the CNTs are put on the carbon grid mesh. Only strong iron peak presents (Fig. 3.34 (d)) on the spectrum images shows that the analysis area is the area where CNTs iron catalyst exists.

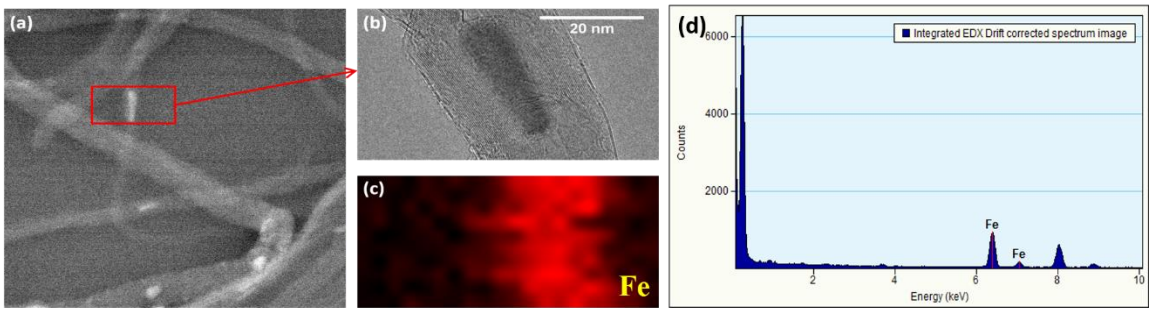

Fig 3.34 TEM-EDS of iron particles (a) STEM image of MWCNTs structure; (b) Bright field TEM image of the structure. (c) Experimental display of locations of various elements during EDS, iron is marked as red. (d) Elemental composition of electron dense using XEDS.

EDS is also used to analyze another area from which CNTs appear to originate. One single 50 nm alumina particle is chosen to be analysis by EDS. Corrected spectrum show the presence of the major elements in this area of aluminum, iron and carbon. Both strong aluminum and iron peaks are present (Fig. 3.34) in the spectrum images, suggesting that the region is a single alumina particle. In Figure 3.22 (b), (c), (d), (e), TEM-EDS color elemental mapping indicate the elements existing in this area as the aluminum is shown as green and iron is marked by red.

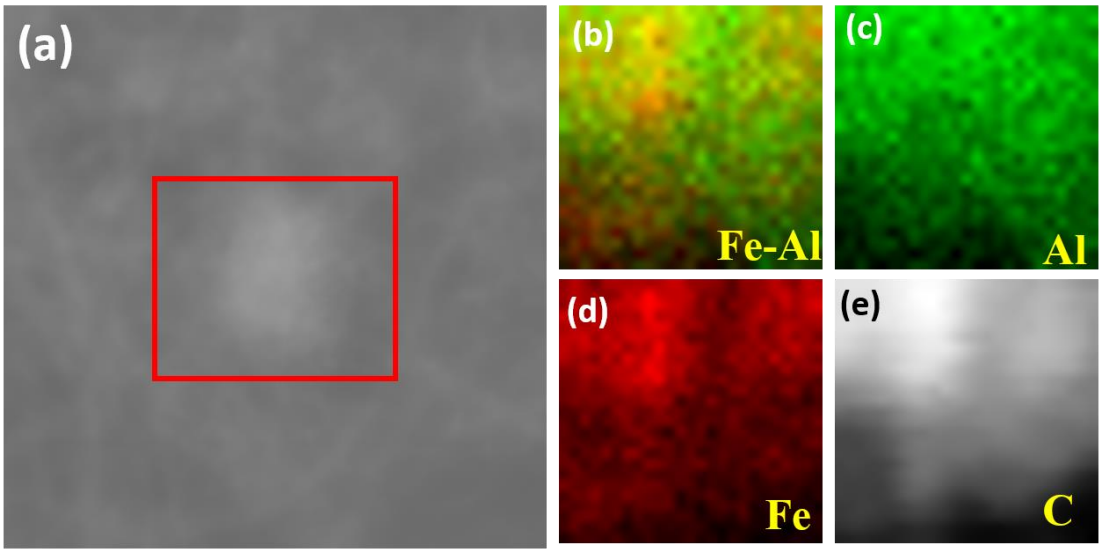

Fig 3.35 TEM-EDS of alumina particles (a) STEM image of the area using EDS; (b). (c). (d) (e) Elemental composition of electron dense using XEDS, (b) shows the distribution of aluminum and iron, (c) shows the distribution of aluminum, (d) shows the distribution of iron (e) shows the distribution of carbon.

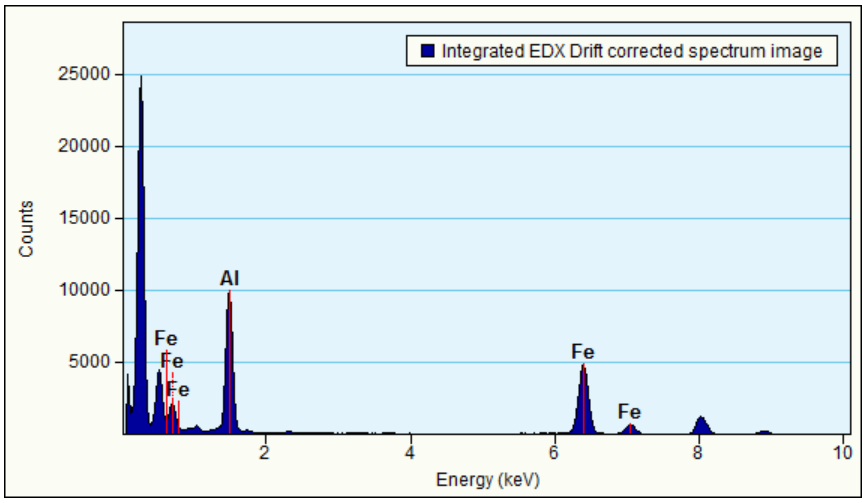

Fig 3.36 EDX drift corrected spectrum image of the area marked in Fig 3.35(a).

3.3 TGA results

Thermogravimetric analysis (TGA) is an analytical technique used to determine a material's thermal stability and its fraction of volatile components by monitoring the weight change that occurs as a specimen is heated. TGA is a common testing method to quantify the purity of carbon materials because different carbon material oxidize at different temperature. Disordered or amorphous carbons tends to be oxidized at around 350 °C because of their lower activation energies for oxidation or due to the presence of a large number of active sites [90]. On the other hand, a well graphitized structure starts to oxidize at a relatively higher temperature between 600 and 700 C, depending on type of CNTs [91].

Thermogravimetric analyses were performed on a TA Instruments Q50 thermogravimetric analyzer. Samples were analyzed in platinum pans at a heating rate of 1 °C/min to 750 °C in an atmosphere of air flowing at 180 mL/min. Sample masses range from 1-5 mg. Sample purification or other operation was not required, as alumina-CNTs samples were simply exfoliated from the silicon wafer. The rate of mass loss and percentage of mass loss will be examined to give qualitative assessments of CNT purity and to determine the mass fraction of CNTs relative to the alumina particle mass.

All the 8 different samples are tested in TGA, with results plotted in Fig.3.37 and 3.38.

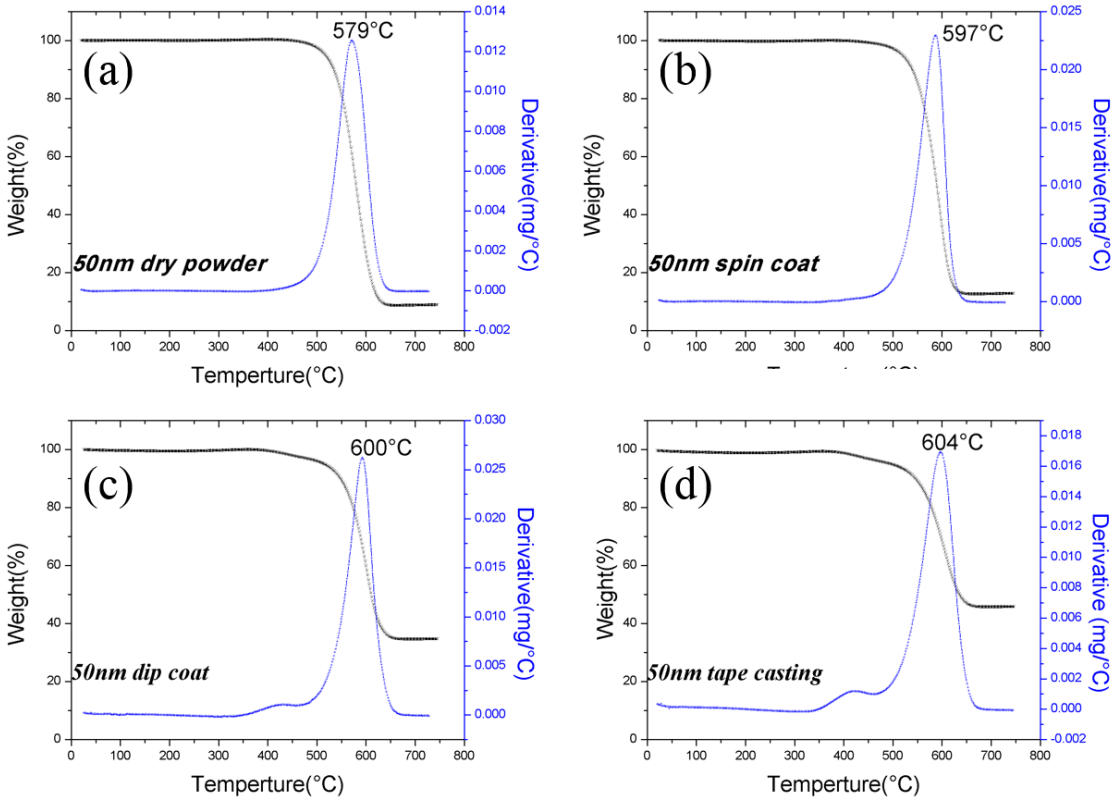

Fig 3.37. TGA tests of 50 nm alumina-CNTs of 4 different surfaces application. The weight percentage and mass loss rate are shown and the temperature of peak derivative are marked. The TGA results from CNTs grown from (a) the dry adhesion method, (b) spin coating method (c) dip coating method, and (d) tape casting method. Disorganized carbons were observed oxidized around 425°C for the dip coat and tape casting method, but the ratio is low.

TGA analysis of 50 nm alumina-CNTs are shown in Fig 3.37. The weight percentage and mass loss rate are shown and the temperature of peak derivative is marked. The residual mass after oxidation represents non-carbon species (alumina and iron). The oxidized mass represents the CNT yield from the alumina particles. Therefore, a large residual mass indicates a decreased CNT yield. From Fig 3.37, we could conclude that the dry powder adhesion surface application gives the highest CNT weight percentage, which means the highest weight ratio while tape casting application gives the lowest weight ratio. This trend is inversely related to the initial alumina particle density. The temperature of

peak derivative is ranging from 579°C to 604 ℃ which shows the CNT structures synthesized is a well graphitized structure as it oxidize at a relatively higher temperature. Disorganized carbon species were observed oxidized around 425°C for the dip coat and tape casting method, but the ratio is low.

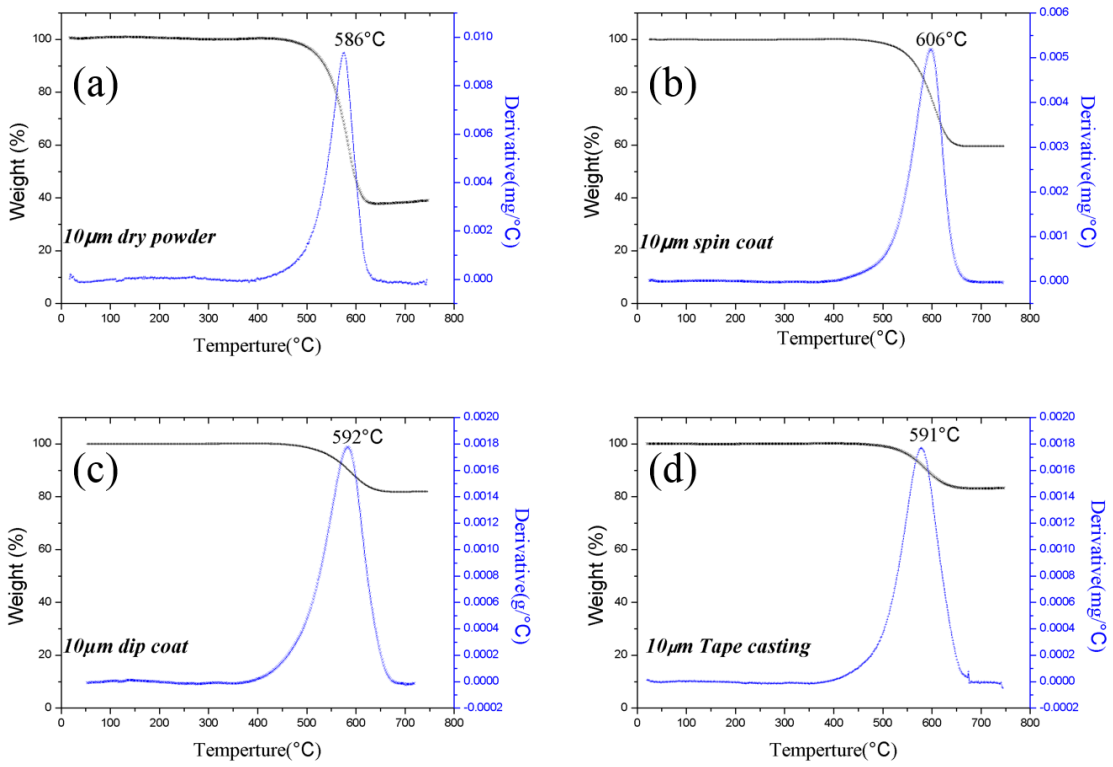

Fig 3.38. TGA tests of 10μm alumina-CNTs of 4 different surfaces application. The weight percentage and mass loss rate are shown and the temperature of peak derivative are marked. No appreciable amorphous carbon was observed for (a) the dry adhesion method, (b) the spin coat application method, (c) the dip coat application method, and (d) the tape casting application method.

TGA analysis of 10 μm alumina-CNTs are shown in Fig 3.38. The weight percentage and mass loss rate are shown and the temperature of peak derivative is marked. As seen from the plots, the CNT weight ratio changes from 17% to 60%. The dry powder adhesion surface application gives the highest CNTs weight ratio, which also indicates that the alumina particles of dry adhesion are fully used as the support in CNT growth. Similar

to the CNTs prepared on the 50 nm alumina particles, the powder density of 10 μm dry powder is the lowest among the 4 different surface application techniques. The mass loss derivative by temperature is also shown in the images. The temperature of maximum mass rate loss (586 – 606°C) indicate the structure is a well graphitized structure.

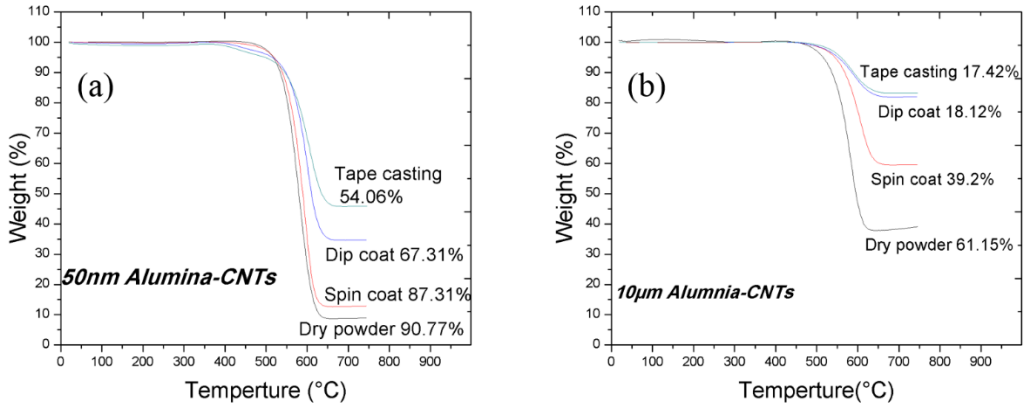

Fig 3.39. TGA mass loss percentage for CNTs grown on (a) 50 nm alumina particles and (b) 10 μm alumina particles. The weight percentage lost during oxidation is denoted by the text in each figure. This mass loss is ascribed to the oxidation of the CNT constituent. Note that the greatest mass percentage of CNTs for each powder size is the dry adhesion technique, followed by the spin coating, dip coating, and tape casting methods.

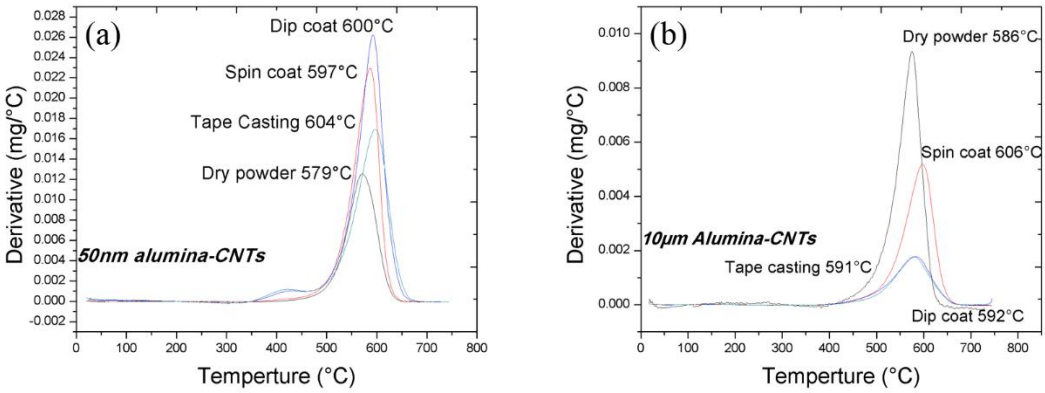

Fig 3.40. TGA mass loss rate for CNTs grown on (a) 50 nm alumina particles and (b) 10μm alumina powder. Peak temperature are marked.

Table3.1 TGA test results showing CNT weight percentage and peak mass loss temperature summary

Powder size	Surface application	Weight Percentage (%)	CNTs Weight Percentage (%)	Peak Weight Derivative Temperature (℃)
50nm	Dry powder	9.23	90.77	579
	Spin coat	12.69	87.31	597
	Dip coat	32.7	67.3	600
	Tape Casting	45.94	54.06	604
10μm	Dry powder	38.95	61.05	586
	Spin coat	60.8	39.2	606
	Dip coat	81.88	18.12	592
	Tape Casting	82.58	17.42	591

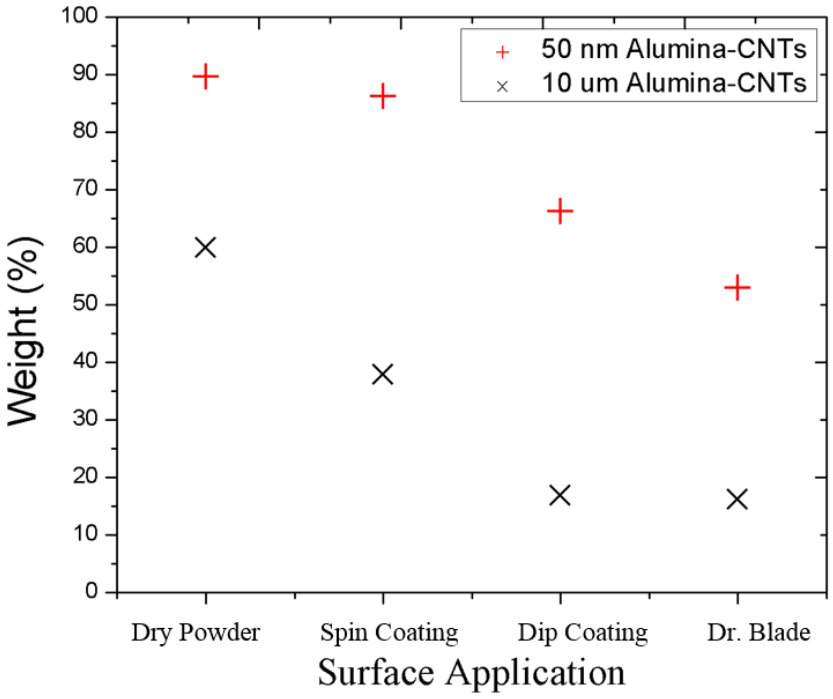

Fig 3.41 Comparison of the CNT weight percentage based on TGA. Both particle sizes are similarly sensitive to particle deposition technique.

Figures 3.39 and 3.40 show the complete set of TGA test results for all 8 sample types. The mass and mass loss rate are plotted as a function of temperature. The mass loss is due to the oxidation of carbon materials. The CNTs weight ratio have the same tendency for both particle sizes, as shown as Figure 3.28. Dry powder application has the lowest powder density but have a highest CNTs weight ratio. Tape casting produces the highest powder density but a lowest CNTs weight ratio. Based on this observation, it is believed that the competition for carbon among the growing CNTs may limit the growth rate of CNTs when a high density of particles exists. In other words, the growth of CNTs on alumina powder is hypothesized to be a diffusion-limited reaction.

The temperature associated with the maximum mass rate loss is similar for all cases at approximately 600°C. The temperature of peak mass loss indicates the strength of c=c carbon bonds. In well graphitized materials, the oxidation temperature is relatively high (600°C) while disorganized carbon oxidizes at a reduced temperature 350°C. Little difference between the peak oxidation temperatures for all samples indicates similar graphitization for all samples. Disordered or amorphous carbons were observed around 425°C only in sample of 50nm dip coat and 50 nm tape casting.

To confirm the results, TGA tests were repeated for all the 8 different samples at least twice. Results are shown below and the percent difference between two different tests for every samples is computed, with differences in results of less than 5%.

Table3.2 TGA repeat test result

Powder size	Surface application	TGA test 1/ Weight left over (%)	TGA test 2/ Weight left over (%)	Error
50nm	Dry powder	90.264	91.278	-1.014
	Spin coat	87.31	87.31	0
	Dip coat	69.31	65.3	4.01
	Tape Casting	54.06	54	0.06
10μm	Dry powder	60.06	62.24	-2.18
	Spin coat	40.46	37.94	2.52
	Dip coat	18.12	18.08	0.04
	Tape Casting	18.08	16.76	1.32

Evidence of alumina particles not supporting CNT synthesis

The TGA data suggests that different surface application techniques will result in a different weight percentage of CNTs. We hypothesize that the alumina particle density on the silicon surface is the main driver of the CNT to particle mass ratio. With a relatively low density of alumina particles, the competition for available carbon is decreased, and each alumina particle may support a greater growth rate of CNTs. Particularly for application techniques that result in numerous layers of particles stacked upon each other, some of the buried alumina particles may have limited access to carbon and catalyst iron, and may not fully support CNT growth. Although as CNTs grow on the top-most particle layer(s), the growing force will lift the alumina particles up and hydrocarbon gas may become more available to bottom alumina particles that may then be used to support CNT synthesis. Using TGA alone, it is not possible to ascertain if the particles on bottom ones are fully support CNT synthesis like those particles located on the top surface of the particle layer. The bottom surface of the CNT-alumina clusters were examined by SEM after delaminating the CNT product from the silicon support substrate. The 10 μm tape casting

alumina-CNTs sample is examined in SEM since it was proved to be the lowest weight ratio of CNTs, with representative images shown below.

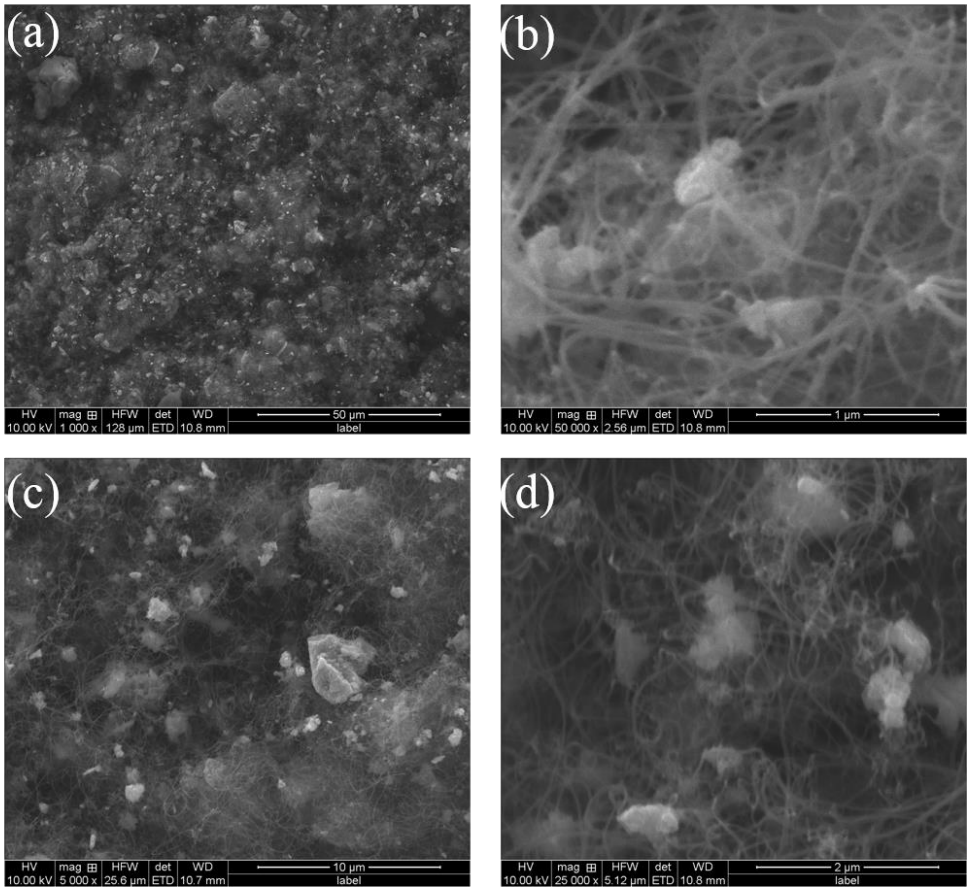

Fig 3.42 SEM images of the bottom surface of 10 μm alumina-CNT clusters. (a) Low magnification images show many alumina particles (b-d) higher magnification images show that many alumina particles on bottom surface of the CNT structure are not fully utilized to support CNT growth. In fact, some particles seem to support no CNT growth, unlike particles found on the top surface of the CNT-alumina clusters.

As seen in Fig 3.42, many alumina particles that resided on the silicon surface at the bottom of the CNT-alumina product supported a relatively low density of CNTs. CNTs are not fully covering alumina as is observed from the top surface of the CNT-alumina product. These images support the hypothesis that inadequate hydrocarbon and catalyst transport to the bottom layers of alumina particles leads to a gradient in CNT population

density from the top to the bottom of the CNT-alumina product. To obtain the maximum CNT yield from alumina particles, therefore, a relatively low application density of alumina support particles is recommended to reduce to overall competition for the available hydrocarbon and catalyst.

3.4 Raman Spectroscopy

Carbon nanotubes have proven to be a unique system for the study of Raman spectra in one-dimensional systems, and at the same time Raman spectroscopy has provided an exceedingly powerful tool for the characterization of carbon nanotubes, particularly SWCNTs. Raman spectroscopy may provide vibrational properties and electronic structures of SWCNT, particularly for characterization of SWCNT diameters, and quality of the samples. The most prominent Raman features in CNTs are the radial breathing modes (RBMs) of single and double-walled CNTs, the higher frequency D (disordered), G (graphite), and G' (second-order Raman scattering from D-band variation) modes. The D band indicates the defects in the graphitic structure and disordered carbon deposits. The D/G intensity ratio presents the relative CNT purity by relating the Raman intensity of less ordered carbon species to that of highly graphitized carbon species. Therefore, a low D/G intensity ratio is desired for highly graphitized samples. The RBM peaks are present only for single-walled or few-walled CNT samples. These Raman shift of these peaks are indicative of the CNT diameter. Because the RBM peaks are resonant only at discrete energies, multiple laser frequencies are required to create a full mapping

of all RBMs. Nevertheless, the presence of RBM peaks (at wavenumbers generally less than 250 cm^{-1}, indicate the presence of single or few-walled CNTs.

A D/G intensity ratio of greater than unity indicates a high quantity of structural defects. MWCNT D/G intensity ratio is frequently close to a value of 1, indicating a relatively high quantity of structural defects due to multiple graphite layers. Both SWCNT and DWCNT generally show lower intensities of D and G intensity ratios.

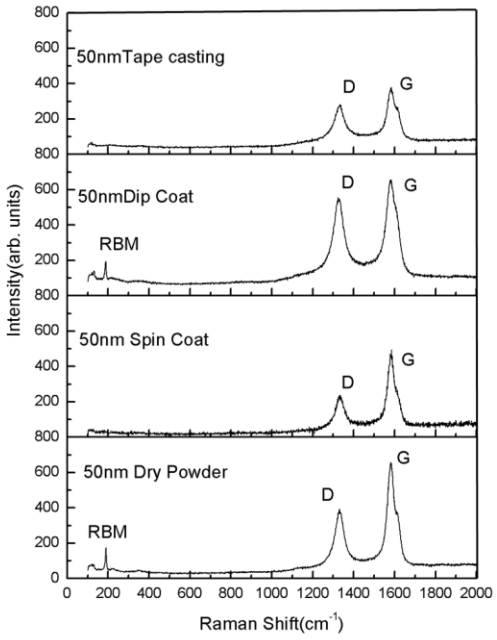

50nm Tape Casting	RBM1	RBM2	D	G	ID/IG
Peak Potion	-------	------	1335.227	1581.838	
Intensity	------	------	281.9316	376.9805	0.75

50nm Dip Coat	RBM1	RBM2	D	G	ID/IG
Peak Potion	131.12812	189.8627	1331.537	1581.838	
Intensity	140.64782	167.2507	546.1787	656.7486	0.83

50nm Spin Coat	RBM1	RBM2	D	G	ID/IG
Peak Potion	-------	-------	1330.615	1580.069	
Intensity	-------	-------	234.3184	470.4437	0.50

50nm Dry Powder	RBM1	RBM2	D	G	ID/IG
Peak Potion	131.128128	175.4	1330.615	1581.838	
Intensity	79.985022	175.4093	393.3183	656.7486	0.60

Fig 3.43. Raman spectra for all 50nm alumina-CNTs

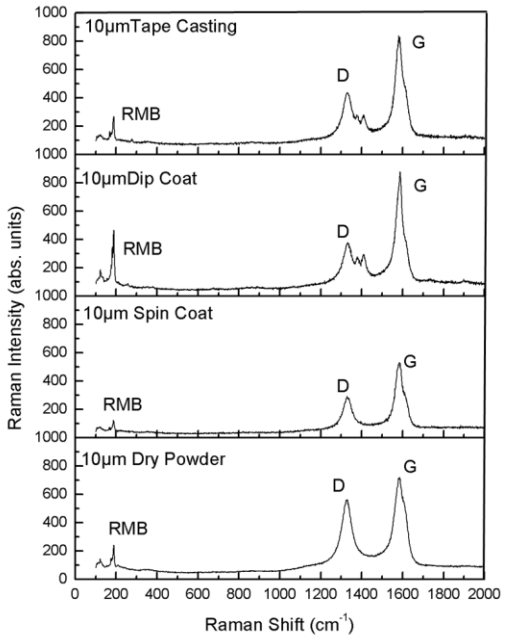

10µm tape casting	RBM1	RBM2	D	G	I_D/I_G
Peak Potion	123.334183	188.749	1331.54	1580.95	
Intensity	143.2549605	271.153	437.53	841.061	0.52

10µm Dip Coat	RBM1	RBM2	D	G	I_D/I_G
Peak Potion	123.334183	188.749	1331.54	1588.03	
Intensity	188.7935809	468.475	380.645	880.86	0.43

10µm Spin Coat	RBM1	RBM2	D	G	I_D/I_G
Peak Potion	123.334183	187.646	1337.07	1585.38	
Intensity	80.2302558	124.491	283.374	531.74	0.53

10µm Dry Powder	RBM1	RBM2	D	G	I_D/I_G
Peak Potion	122.219925	188.749	1325.07	1584.49	
Intensity	144.951833	243.358	559.936	716.136	0.78

Fig 3.44. Raman spectra for all 10 µm alumina-CNTs

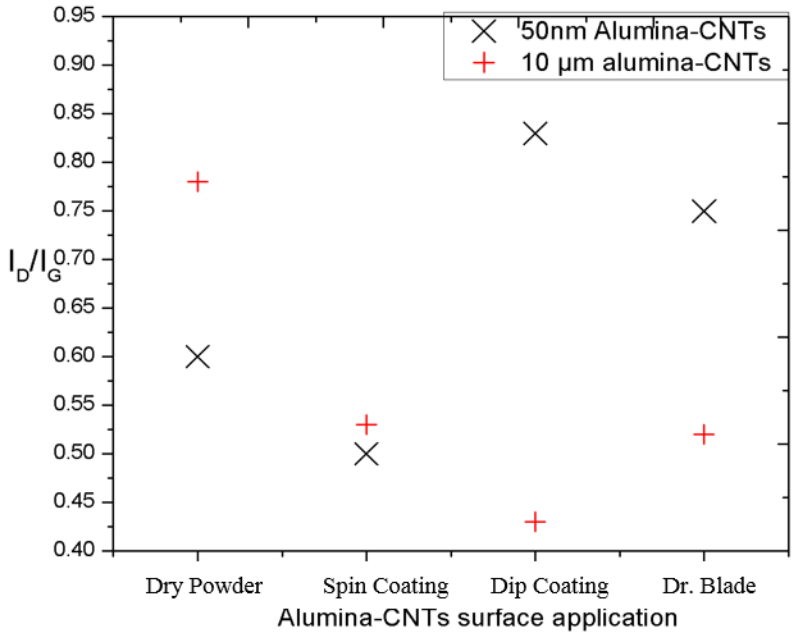

Fig 3.45. I_D/I_G distribution by surface application

The analysis of RBM peaks also allows one to distinguish the diameter of few-walled CNTs. If SWCNTs are present, the RBM frequency may be directly related to the CNT diameter. For DWNTs, one or both CNT walls may produce an RBM signal, each indicative of their respective diameter. However, it may be difficult to distinguish if multiple RBM peaks originate from SWCNTs of different diameters or from inner and outer shells of a DWCNT. RBMs of various intensity are found on many of the CNT samples produced on the CNT powders. The diameter associated with each RBM peak may be estimate according to equation below[92].

$$\omega_r(\mathrm{cm}^{-1}) = 224(\mathrm{cm}^{-1}) / d_t(\mathrm{nm})$$

For double wall CNTs, the inner and outer diameters should be separated by approximately 0.68 nm, or twice the interatomic displacement between graphite layers (0.34 nm). Based upon diameter calculations, the RBM peaks observed may originate from DWCNTs.

Table 3.3 Inner and outer CNT tube diameter of MWCNTs

Powder size	Surface Application	RBM1	RBM2	Diameter 1 (nm)	Diameter 2 (nm)
50nm	Dry Powder	131.1281	175.4	1.71	1.28
	Spin Coat	-------	------	-------	------
	Dip Coat	131.1281	189.8627	1.71	1.18
	Tape casting	-------	------	-------	------
10µm	Dry Powder	122.22	188.749	1.83	1.19
	Spin Coat	123.334	187.646	1.82	1.19
	Dip Coat	123.334	188.749	1.82	1.19
	Tape casting	123.334	188.749	1.82	1.19

To ensure that the alumina particles themselves were not contributing to the observed Raman signal, alumina particles of both size are also analyzed by Raman spectroscopy. Results are shown in Figure 3.30. The Raman scattering result from alumina particles shows no peaks in the bad anticipated for RBMs, indicating that the alumina particles themselves did not contribute to the observed RBM peaks observed. The peak shown around 528 cm^{-1} is the Raman intensity for pure silicon wafer.

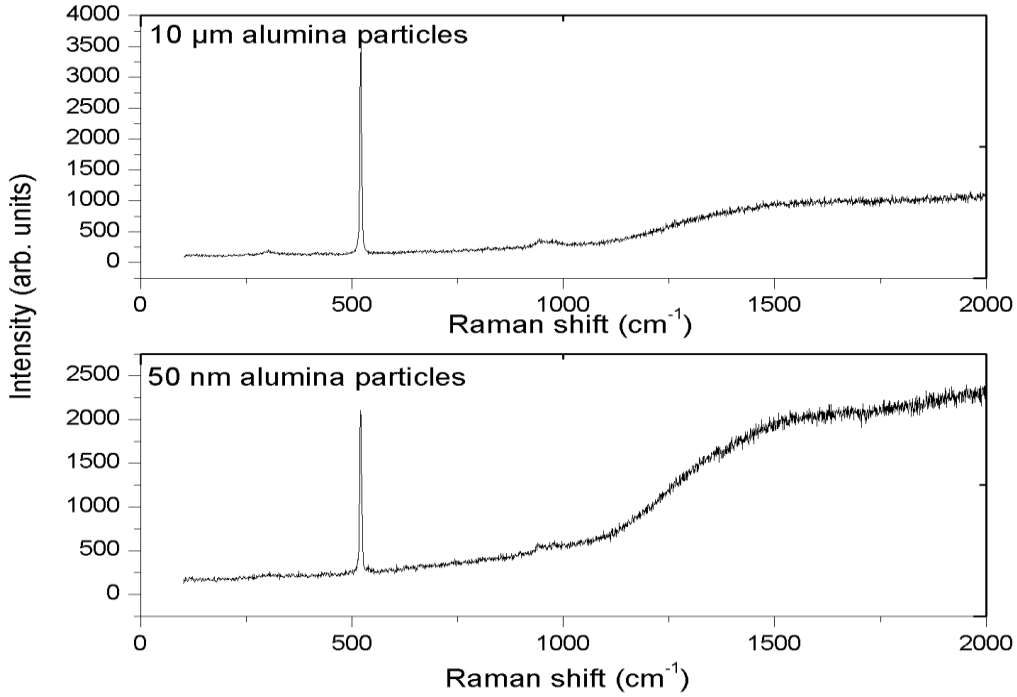

Fig 3.46. Raman scattering of 50nm & 10µm alumina particles

3.5 Applications of Alumina-CNTs

3.51 Strain sensor of CNTs

Using alumina particles as a support substrate for CNT production generates high volume and mass fraction of CNTs that are readily liberated from their growth substrate. The alumina-CNT material has potential for use in many areas. Among all of potential applications, CNT forests offer a significant piezo resistance making them an excellent material for strain sensors. CNTs are currently of interest in the building of advanced sensors [93] and actuators [94] for applications that require self-sensing of motion. CNT forests may undergo significant strain without fraction and can be bent to large angles

without breaking. Structural and electrical characteristics of CNTs include a large surface area, piezo resistivity and electrochemical properties that make them a promising smart sensor material. The electronic properties of nanotubes are interestingly a strong function of their atomic structure. Furthermore, mechanical deformation or chemical functionalization of the surface can induce changes in the conductance [95] of a nanotube. For relatively dense CNT forests, the transfer of electrical charge often must include cooperative transport across many CNTs and CNT-CNT interfaces. Application of mechanical strain to CNT forests alters the number of CNT-CNT contacts and the nature of the charge transfer across interfaces. Their small size allows CNTs to be used as extremely small sensors that are sensitive to the chemical and mechanical environments of the nanotubes. These great properties represent a potential for developing sensors high strain and low operating voltage and for developing multifunctional sensory materials.

In particular, using the piezoresistivity of CNT forests (change in resistance with strain) may be exploited with the alumina-CNT material because charge must be transferred across many CNT clusters. The alumina particles may be deposited in a desired geometry to produce a band of CNTs of desired size. Further, the van der Waals forces that bind the CNT clusters may allow for significant mechanical strain to be accommodated without producing a short circuit. The low mass and mechanical stiffness of the alumina-CNT material are additional advantageous properties relative to mechanical strain sensing. Such a sensor could measure large strain and form a grid over a large area of a structure for structural health monitoring applications[96] or human-motion detection[97]

A CNT strain sensor based on alumina-CNT material is relatively easy to fabricate, as shown below. Alumina particles are fist deposited in a ribbon across a silicon substrate using a felt pen and an ethanol suspension. After synthesis, the alumina-CNTs are removed from the silicon substrate and placed on a thin plastic membrane with high ductility and low electrical conductivity. Copper tape is used at the edge of the CNTs ribbon to serve as an electrode and to adhere the CNT ribbon to the PVC substrate.

Fig 3.47 CNTs strain sensor fabricate outline process chart

The electrical resistance of the CNTs strain sensor is tested with a data collect system—Keithley M2701 Digital Multimeter Data Acquisition and Data logging System, as shown below. Mechanical strain is applied to the sensor in by stretching the plastic membrane. The sensor is stretched with the help of a vice and an average speed of 0.5mm/s. The original sensor length is 24.3mm and measured by a Vernier caliper.

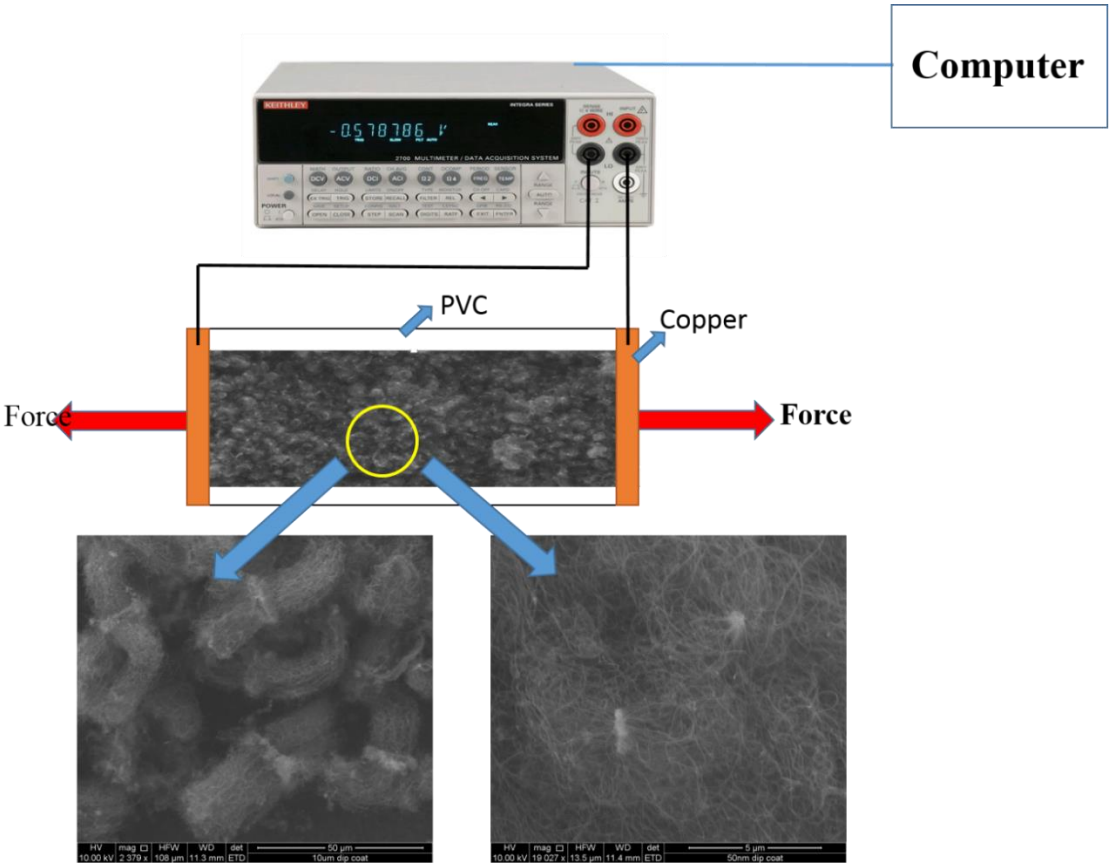

Fig 3.48 Schematic of the CNTs strain sensor data acquisition system.

The resistance change in the strain sensor Rs is

$$Rs = R0 + \Delta R$$

where R0 is original resistance of the strain sensor without any strain and ΔR is the change of resistance due to expand of the CNTs film. With the strain applied to the CNTs, the strain will reduce the connection between CNTs colonies and raise the resistance. The result is tested and plot shown below

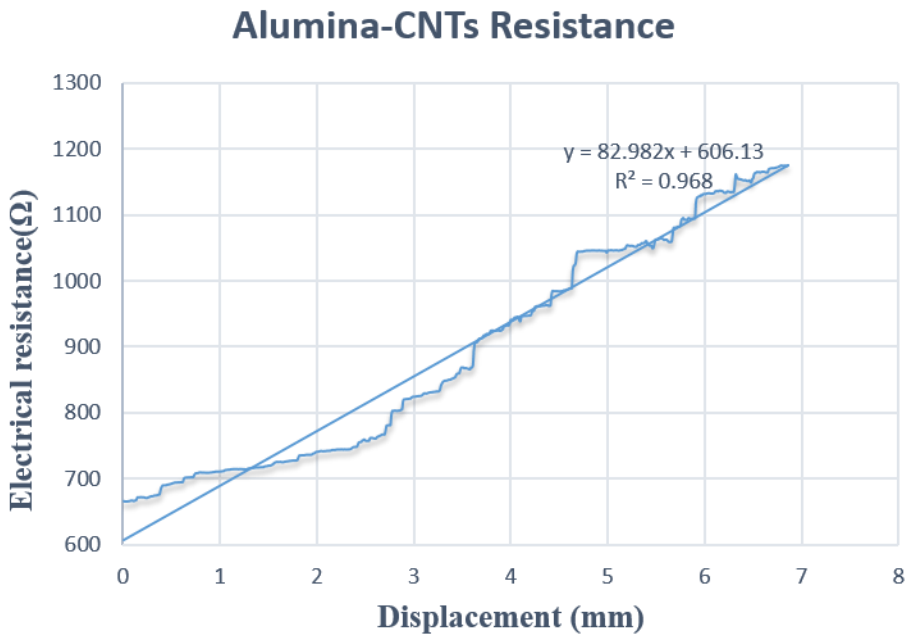

Fig 3.49 Stress and normalized change in CNTs resistivity plotted against applied strain.

The electrical resistance of the CNT-alumina sensor with applied axial tension is shown in Fig 3.49. The electrical resistance increases proportionally with increasing tensile strain from CNTs strain sensor. The increase in resistance can be explained by noting that for the CNT sensor to be electrically conductive, adjacent CNTs must either touch to form conductive paths, or be sufficiently close to each other to enable conductance via "tunneling effect" [98] and [99]. Conductivity (or resistivity) of the alumina and CNTs system, therefore is dictated by the number of contact points and the distances between neighboring particles. Since applied tensile strain likely causes loss of contact and widening of the inter-particle distances, it reduces the current-carrying ability of conductive network, resulting in higher electrical resistance.

A fundamental parameter of the strain gage is its sensitivity to strain, expressed quantitatively as the gage factor (GF). Gage factor is defined as the ratio of fractional change in electrical resistance to the fractional change in length (strain):

$$\mathrm{GF} = \frac{\Delta R/R}{\Delta L/L}$$

Where ΔR is resistance change in strain gauge resistance, R is unstrained resistance of strain gauge; ΔL is absolute change in length, L is original length. In this CNT strain sensor, ΔR=509Ω, R=666Ω; ΔL is 6.86 mm, L is 24.3 mm. GF here is calculated as 2.71.

Cycling response of the CNT strain sensor was also measured. By repeating loading-unloading strain cycles, the repeatability response of CNT sensors is collect as below. CNTs sensor is stretched to the same position and return to the same position. Due to the position change is small, only 0.3 mm, resistance error exists in data collect and plotted. After multiple strain cycles, the sensor returns to a similar unstrained resistance. The delay time of the electrical response was quite low, although the experimental setup was not conducive to accurately measure the delay time. This preliminary data indicates that the production of high-sensitivity CNT mechanical sensors may be easily produced using powder-based substrates. The sensor we tested is another different from the one used for liner test, which is also shows that resistance is different.

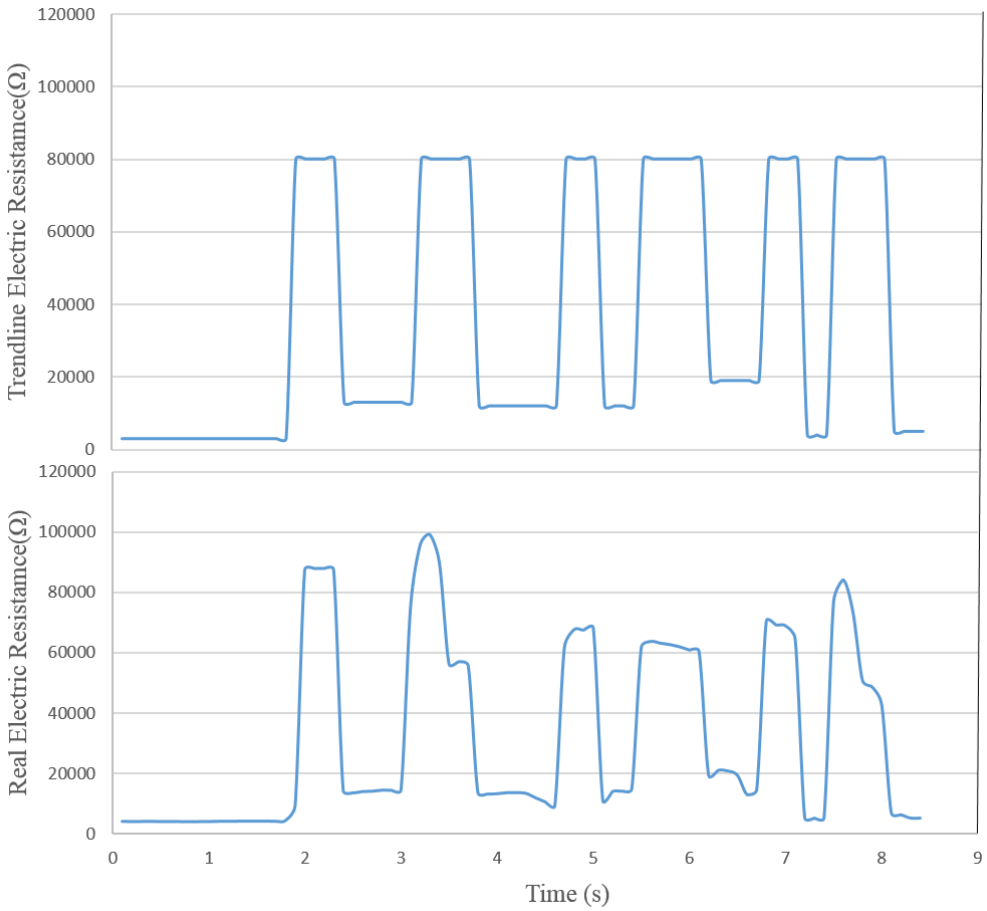

Fig 3.50 Cycling response of strain sensor with loading and unloading response.

3.52 Alumina-CNTs for water treatment

The U.S. Geological Survey [100] found that 96.5% of Earth's water is located in seas and oceans and 1.7% of Earth's water is located in the ice caps. Approximately 0.8% is considered to be fresh water. Fresh and clean water is especially important nowadays for human survival, in particular in fields such as agriculture, energy production, and the manufacture of essential goods. Today, the production of potable water has become a worldwide concern; with the development of human society, water demand is growing

rapidly as a result of increasing population and rapid urbanization. Furthermore, (i) chemical farming techniques (i.e. application of fertilizers, pesticides, and insecticides) and (ii) manufacturers of certain chemicals and pharmaceuticals generate effluent streams, which contribute to fresh water contamination, so exacerbating water shortage concerns. These streams generally contain trace amounts of aromatic and chlorinated hydrocarbons. Among them, chlorobenzenes, owing to their chemical stability and limited photochemical degradation in soil as well as in the aquatic environment, are identified as priority pollutants by the US Environmental Protection Agency [100, 101]. In addition, oil and fuel spills released during industrial accidents or by oil tankers and ships sinking can be catastrophic for marine and aquatic ecosystems. Therefore, much effort has been focused on developing new materials, more effective in removing contaminants from fresh water as well as seawater.

Carbon nanotubes (CNTs), owing to their large specific area and high mechanical and chemical properties, are considered excellent candidates for wastewater cleanup [102, 103]. Significant work has been done Gui et al in 2010 to synthesize such a material consisting of a self-assembled, interconnected CNT skeleton [104] for this purpose. The authors found that this material exhibits interesting absorption capabilities towards organic solvents (i.e. ethanol, chloroform, and hexane) as well as vegetable oil and gasoline. L. Camilli [105] and his group synthesized a freestanding carbon nanotube (CNT) frameworks through a sulfur addition strategy during an ambient pressure chemical vapor deposition process, with ferrocene used as the catalyst precursor. They claim that a three dimensional structure selectively uptakes from water a mass of toxic organic solvent (i.e. dichlorobenzene) about 3.5 times higher than that absorbed by individual CNTs. Our CNT-

alumina samples exhibit an oil absorption capacity higher than that reported in the literature for similar CNT sponges.

Carbon nanotubes are excellent candidate material for water treatment industries for multiple reasons. First, the properties of CNTs' large specific area and high mechanical and chemical properties equips CNTs great absorption ability. CNTs' structure of light weight and super hydrophobicity ensure itself easily floats on the water surface, the lyophilic character enables the CNTs to efficiently separate water from oil contaminants. Second, iron catalyst based CNTs are easily driven by a magnet [18] , CNTs used for water treatment or oil absorption would be easily collected and concentrated, which allows for easy retrieval of the material. Thirdly, CNTs are reusable in these progress - the stripping process (i.e. burning) will not oxidize the CNTs. Using low temperature catalytic oxidation method decompose the oil-absorbed or other organic materials. The CNTs themselves oxidize at a relatively higher temperature between 600 and 700 °C, depending on type of CNTs [101]. Finally, mass production of CNTs has taken a step closer towards commercialization and utilization of CNT technology for large scale applications such as water treatment and desalination. Our method of synthesizing CNTs from alumina powder substrates may be another methodology for high-volume production of CNTs.

The alumina-CNTs we synthesized is a relatively cheap material with a potential commercial appeal applications such as mechanical sensing and oil absorption. The oil absorption capacity was evaluated by measuring the mass of the dry CNTs and the mass after oil absorption. Before being weighed after oil absorption, the sample was removed with sharp needle tweezers and immediately placed onto a weight paper to be measured by

a mass balance. Vegetable oil is used here as the organic matter pollutant to be removed from the water. The CNTs-oil mixture after the adsorption was easily removed from the water by a magnet without any direct contact. Weight of the CNT material is measured before and after oil scavenging. Comparison of weight difference and the absorption capacity are shown below. 50 nm spin coating alumina-CNTs are used for this experiment.

Table3.4 CNTs Oil absorption data

	Experiment 1	Experiment 2	Experiment 3	Experiment 4	Experiment 5
CNTs Weight	0.004	0.006	0.015	0.06	0.026
CNT-Oil Weight	0.154	0.518	0.783	4.032	1.206
Absorption capacity	38.5	86.33	52.2	67.2	46.38

As we could see from the table, the CNTs oil absorption capacity changes in different experiment, ranging from 36.5 to 86.33. Although the absorption capacity is not higher as other literature [98], it absorbs an average of 50 times its original weight. This data proves the high absorption capacity of Alumina-CNTs we synthesized by taking advantage of its hydrophobic and oleophilic properties as well as its microporous features. It is also shows this alumina-CNTs may be an ideal candidate for use as an absorbent for oil/water separation and the removal of toxic organic solvents (i.e. odichlorobenzene) from water.

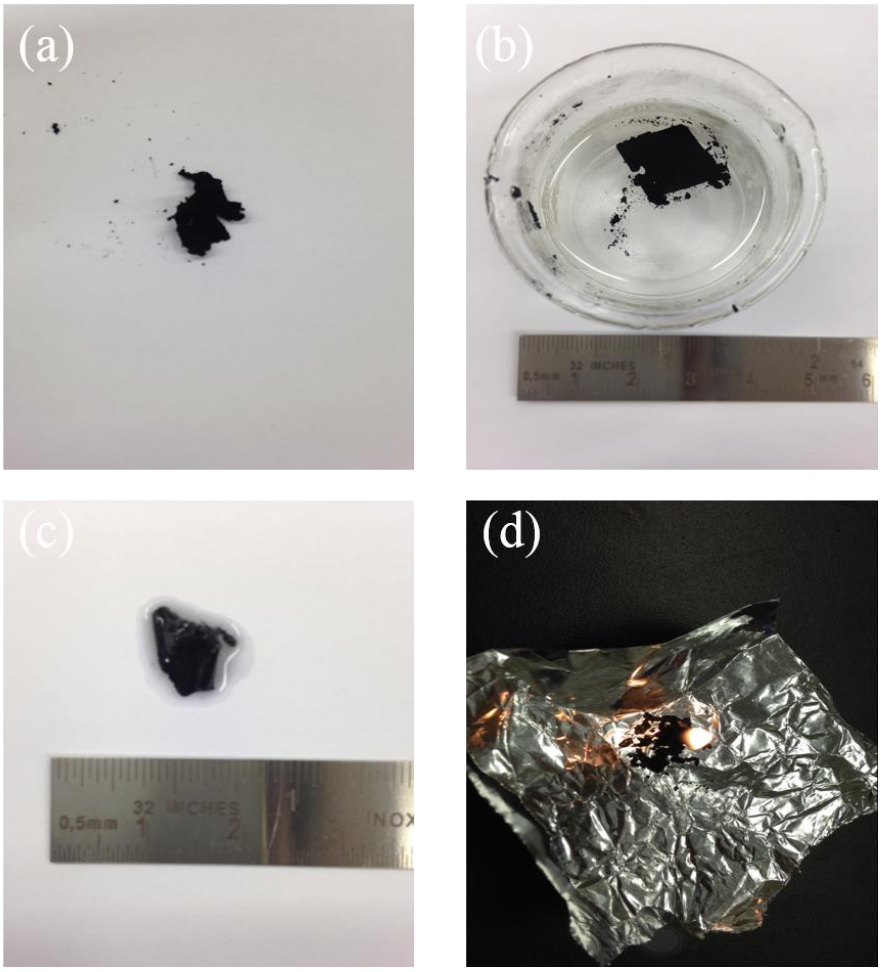

Fig 3.51 Progress of CNT absorption of oil and burning of the oil to reconstitute the CNT material. (a) CNT before oil absorption. (b) CNT is absorbing oil from the water. (c) The CNT after the oil absorption. (d) Burning of the absorbed oil. The CNT block is not consumed during burning, and may b reused.

After CNTs absorbed oil, the oil may be removed by a burning process. The CNT-oil material is easily removed and separated from water by a tweezers or magnet. The oil content is ignited and burned as seen in the Fig3.51. SEM is utilized to analyze the CNT material after the burning process. The CNTs show little oil residue or capillary densification. The CNT material after the burning process is reusable in this oil absorption and desorption progress. SEM images of CNTs after burning are shown blow.

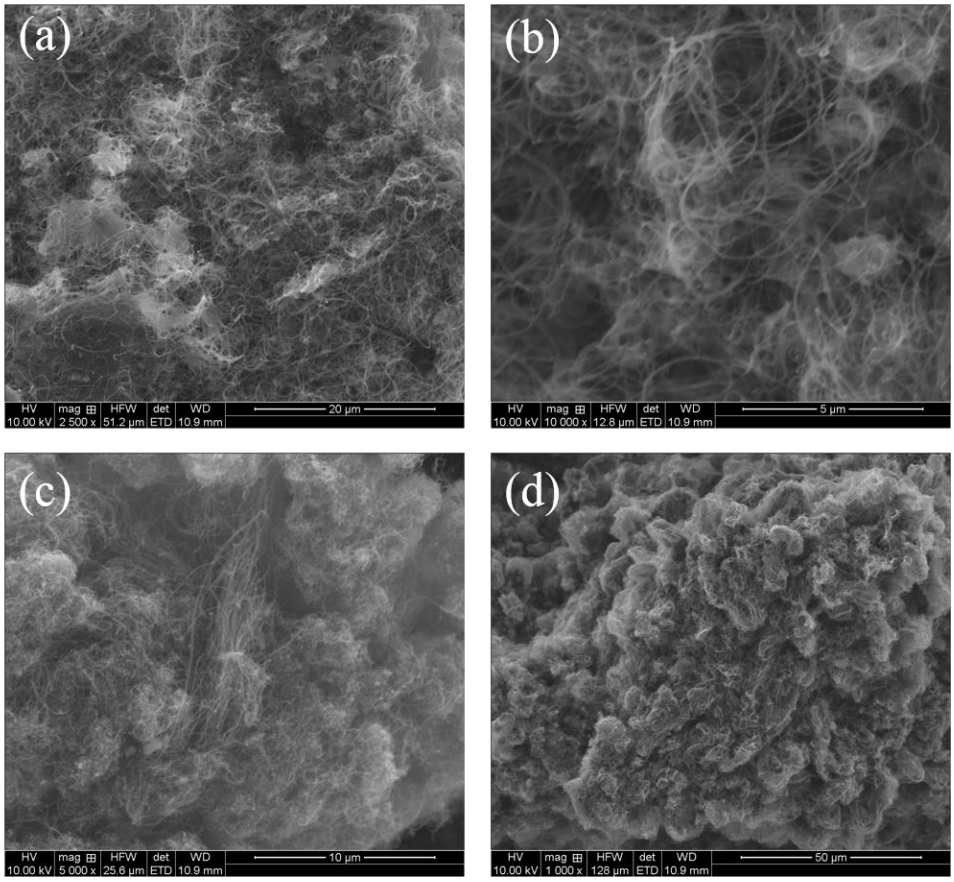

Fig 3.52 SEM images of CNTs after absorbed oil is burned away. (a-d) High resolution SEM images of CNTs after burning shows little residue and a CNT morphology similar to the original material.

The reusable feature makes CNTs oil absorption technology more attractive comparing with other absorb material. Although the toxicity of CNTs is still under research [106], the practical applications in filtration and water treatment keeps CNTs an attractive material which needs more attention and research.

Chapter 4 Conclusions and Future Work

4.1 Summary and Conclusions

Carbon nanotubes (CNTs) are synthesized on alumina particles using floating catalyst CVD. Each of the 8 different alumina-CNTs sample configurations (4 catalyst deposition techniques and 2 nominal particle sizes) were subjected to multiple analysis techniques to characterize the CNT yield with respect to CNT morphology, density, and diameter distribution. The techniques used include scanning electron microscopy (SEM), transmission electron microscopy (TEM), thermo gravimetric analysis (TGA) and Raman spectroscopy.

By the comparing we could found that, the surface application will not influence the morphology of CNTs on alumina particles. However, the density of alumina particles will have a deep influence on CNTs weight ratio. Not all alumina particles support CNT growth higher alumina particle density samples. Smaller diameter distribution of CNTs were gained in 10 μm particles. MWCNTs are found in all the 8 samples and comprise the significant majority of the CNTs produced. Small diameter CNTs which may be DWCNTs or SWCNT were found by Raman spectroscopy.

The alumina-CNTs we synthesized is a relatively inexpensive material with a potential commercial appeal for applications such as mechanical sensing and oil absorption. The demonstrations of using CNTs grown on alumina particles proves the alumina-CNTs great potential for sensing with its excellent performance in terms of linearity, selectivity, stability and fast response. The reusable CNTs oil capture CNTs provide a new

environment-friendly nature oil capture device with great capture capacity by weight which maybe also create a new area where high-volume CNTs are greatly welcomed.

4.2 Future Work

As we summarized before, the CNTs synthesized on alumina particles have different properties due to the size difference and surface applications. More work could be put on this research since great advantages have been discovered using the alumina-CNTs in applications. A more detailed parametric study could be performed by synthesizing CNTs on alumina particles of intermediate particle sizes. Further, synthesis from other powder compositions such as SiN or SiO2 may offer still greater parametric variations. By the advantages of modern nanotechnology, especially with the help of scanning electron microscopy (SEM), transmission electron microscopy (TEM), thermo gravimetric analysis (TGA) and Raman spectroscopy, a better understanding of synthesizing CNTs on alumina particles could be gained. Surface area test and nanoindentation test would also be desired on alumina-CNTs to determine the local mechanical behavior of each type of CNT-alumina variation. In the area of real application of alumina-CNTs, the limit of strain sensors and oil capture especially the limitation differences of different alumina-CNTs could be fruitful. More controllable deposition techniques (such as aerosol direct writing) of fine-scale particles could further enhance the application space by creating controlled and small-scale devices.

Bibliography

[1] Iijima, Sumio. "Helical microtubules of graphitic carbon." nature 354, no. 6348 (1991): 56-58.

[2] Peng, Bei, Mark Locascio, Peter Zapol, Shuyou Li, Steven L. Mielke, George C. Schatz, and Horacio D. Espinosa. "Measurements of near-ultimate strength for multiwalled carbon nanotubes and irradiation-induced crosslinking improvements." Nature nanotechnology 3, no. 10 (2008): 626-631.

[3] Wei, B. Q., R. Vajtai, and P. M. Ajayan. "Reliability and current carrying capacity of carbon nanotubes." Applied Physics Letters 79, no. 8 (2001): 1172-1174.

[4] Hong, Byung Hee, Ju Young Lee, Tobias Beetz, Yimei Zhu, Philip Kim, and Kwang S. Kim. "Quasi-continuous growth of ultralong carbon nanotube arrays."Journal of the American Chemical Society 127, no. 44 (2005): 15336-15337.

[5] Kam, Nadine Wong Shi, Michael O'Connell, Jeffrey A. Wisdom, and Hongjie Dai. "Carbon nanotubes as multifunctional biological transporters and near-infrared agents for selective cancer cell destruction." Proceedings of the National Academy of Sciences of the United States of America 102, no. 33 (2005): 11600-11605.

[6] van der Veen, Marleen H., Bart Vereecke, Masahito Sugiura, Yusaku Kashiwagi, Xiaoxing Ke, Daire J. Cott, Johannes KM Vanpaemel et al. "Electrical and structural characterization of 150 nm CNT contacts with Cu damascene top metallization."

In Interconnect Technology Conference (IITC), 2012 IEEE International, pp. 1-3. IEEE, 2012.

[7] Star, Alexander, Eugene Tu, Joseph Niemann, Jean-Christophe P. Gabriel, C. Steve Joiner, and Christian Valcke. "Label-free detection of DNA hybridization using carbon nanotube network field-effect transistors." Proceedings of the National Academy of Sciences of the United States of America 103, no. 4 (2006): 921-926.

[8] Vidu, Ruxandra, Masoud Rahman, Morteza Mahmoudi, Marius Enachescu, Teodor D. Poteca, and Ioan Opris. "Nanostructures: a platform for brain repair and augmentation." Frontiers in systems neuroscience 8 (2014).

[9] Collins, Philip G., Keith Bradley, Masa Ishigami, and A. Zettl. "Extreme oxygen sensitivity of electronic properties of carbon nanotubes." science 287, no. 5459 (2000): 1801-1804.

[10] Bekyarova, Elena, Irina Kalinina, Mikhail E. Itkis, Leanne Beer, Nelson Cabrera, and Robert C. Haddon. "Mechanism of ammonia detection by chemically functionalized single-walled carbon nanotubes: In situ electrical and optical study of gas analyte detection." Journal of the American Chemical Society 129, no. 35 (2007): 10700-10706.

[11] Qi, Pengfei, Ophir Vermesh, Mihai Grecu, Ali Javey, Qian Wang, Hongjie Dai, Shu Peng, and K. J. Cho. "Toward large arrays of multiplex functionalized carbon nanotube sensors for highly sensitive and selective molecular detection." Nano letters 3, no. 3 (2003): 347-351.

[12] Kong, Jing, Nathan R. Franklin, Chongwu Zhou, Michael G. Chapline, Shu Peng, Kyeongjae Cho, and Hongjie Dai. "Nanotube molecular wires as chemical sensors." science 287, no. 5453 (2000): 622-625.

[13] Britto, P. J., K. S. V. Santhanam, and P. M. Ajayan. "Carbon nanotube electrode for oxidation of dopamine." Bioelectrochemistry and Bioenergetics 41, no. 1 (1996): 121-125.

[14] Wang, Jianxiu, Meixian Li, Zujin Shi, Nanqiang Li, and Zhennan Gu. "Electrocatalytic oxidation of norepinephrine at a glassy carbon electrode modified with single wall carbon nanotubes." Electroanalysis 14, no. 3 (2002): 225-230.

[15] Nguyen, Cattien V., Lance Delzeit, Alan M. Cassell, Jun Li, Jie Han, and M. Meyyappan. "Preparation of nucleic acid functionalized carbon nanotube arrays." nano Letters 2, no. 10 (2002): 1079-1081.

[16] Nakayama, Yoshikazu. "Plasticity of carbon nanotubes: aiming at their use in nanosized devices." Japanese Journal of Applied Physics 46, no. 8R (2007): 5005.

[17] Treacy, M. M. J., T. W. Ebbesen, and J. M. Gibson. "Exceptionally high Young's modulus observed for individual carbon nanotubes." (1996): 678-680.

[18] Lukić, B., Jin Won Seo, E. Couteau, Kyumin Lee, Silvija Gradečak, R. Berkecz, K. Hernadi et al. "Elastic modulus of multi-walled carbon nanotubes produced by catalytic chemical vapour deposition." Applied Physics A 80, no. 4 (2005): 695-700.

[19] Xie, Sishen, Wenzhi Li, Zhengwei Pan, Baohe Chang, and Lianfeng Sun. "Mechanical and physical properties on carbon nanotube." Journal of Physics and Chemistry of solids 61, no. 7 (2000): 1153-1158.

[20] Lepro, Xavier, Marcio D. Lima, and Ray H. Baughman. "Spinnable carbon nanotube forests grown on thin, flexible metallic substrates." Carbon 48, no. 12 (2010): 3621-3627.

[21] Wang, Xueshen, Qunqing Li, Jing Xie, Zhong Jin, Jinyong Wang, Yan Li, Kaili Jiang, and Shoushan Fan. "Fabrication of ultralong and electrically uniform single-walled carbon nanotubes on clean substrates." Nano letters 9, no. 9 (2009): 3137-3141.

[22] Can, Roberto J., Brian W. Grimsley, Michael W. Czabaj, Emilie J. Siochi, and Brandon Hull. "Processing and Characterization of Carbon Nanotube Composites." (2014).

[23] Chae, Han Gi, and Satish Kumar. "Rigid-rod polymeric fibers." Journal of Applied Polymer Science 100, no. 1 (2006): 791-802.

[24] Can, Roberto J., Brian W. Grimsley, Michael W. Czabaj, Emilie J. Siochi, and Brandon Hull. "Processing and Characterization of Carbon Nanotube Composites." (2014).

[26]Shulz, M.J.; Kelkar, M.D.; Sundareson, M.J. ; (2005). Boca Raton: CRC Press; 2005.

[25] Can, Roberto J., Brian W. Grimsley, Michael W. Czabaj, Emilie J. Siochi, and Brandon Hull. "Processing and Characterization of Carbon Nanotube Composites." (2014).

[26] Hutchison, J. L., N. A. Kiselev, E. P. Krinichnaya, A. V. Krestinin, R. O. Loutfy, A. P. Morawsky, V. E. Muradyan et al. "Double-walled carbon nanotubes fabricated by a hydrogen arc discharge method." Carbon 39, no. 5 (2001): 761-770.

[27] Chen, Changxin, Wenzhe Chen, and Yafei Zhang. "Synthesis of carbon nano-tubes by pulsed laser ablation at normal pressure in metal nano-sol." Physica E: Low-dimensional Systems and Nanostructures 28, no. 2 (2005): 121-127.

[28] Che, G., B. B. Lakshmi, C. R. Martin, E. R. Fisher, and Rodney S. Ruoff. "Chemical vapor deposition based synthesis of carbon nanotubes and nanofibers using a template method." Chemistry of Materials 10, no. 1 (1998): 260-267.

[29] Cheng, H. M., Feng Li, Ge Su, H. Y. Pan, L. L. He, X. Sun, and M. S. Dresselhaus. "Large-scale and low-cost synthesis of single-walled carbon nanotubes by the catalytic pyrolysis of hydrocarbons." Applied Physics Letters72, no. 25 (1998): 3282-3284.

[30] Hata, Kenji, Don N. Futaba, Kohei Mizuno, Tatsunori Namai, Motoo Yumura, and Sumio Iijima. "Water-assisted highly efficient synthesis of impurity-free single-walled carbon nanotubes." Science 306, no. 5700 (2004): 1362-1364.

[31] Byon, Hye Ryung, Hyunseob Lim, Hyun Jae Song, and Hee Cheul Choi. "A synthesis of high purity single-walled carbon nanotubes from small diameters of cobalt nanoparticles by using oxygen-assisted chemical vapor deposition process." Bulletin-Korean Chemical Society 28, no. 11 (2007): 2056.

[32] Huang, Z. P., J. W. Xu, Z. F. Ren, J. H. Wang, M. P. Siegal, and P. N. Provencio. "Growth of highly oriented carbon nanotubes by plasma-enhanced hot filament chemical vapor deposition." Applied Physics Letters 73, no. 26 (1998): 3845-3847.

[33] Bower, Chris, Otto Zhou, Wei Zhu, D. J. Werder, and Sungho Jin. "Nucleation and growth of carbon nanotubes by microwave plasma chemical vapor deposition." Applied Physics Letters 77, no. 17 (2000): 2767-2769.

[34] Wang, Jianjun, Mingyao Zhu, Ron A. Outlaw, Xin Zhao, Dennis M. Manos, and Brian C. Holloway. "Synthesis of carbon nanosheets by inductively coupled radio-frequency plasma enhanced chemical vapor deposition." Carbon 42, no. 14 (2004): 2867-2872.

[35] Kumar, Mukul, and Yoshinori Ando. "Chemical vapor deposition of carbon nanotubes: a review on growth mechanism and mass production." Journal of nanoscience and nanotechnology 10, no. 6 (2010): 3739-3758.

[36] Huang, Shaoming, Mike Woodson, Richard Smalley, and Jie Liu. "Growth mechanism of oriented long single walled carbon nanotubes using “fast-heating” chemical vapor deposition process." Nano Letters 4, no. 6 (2004): 1025-1028.

[37] Nagy, G., M. Levy, R. Scarmozzino, R. M. Osgood Jr, H. Dai, R. E. Smalley, C. A. Michaels, G. W. Flynn, and G. F. McLane. "Carbon nanotube tipped atomic force microscopy for measurement of< 100 nm etch morphology on semiconductors." Applied physics letters 73, no. 4 (1998): 529-531.

[38] Wong, Eric W., Paul E. Sheehan, and Charles M. Lieber. "Nanobeam mechanics: elasticity, strength, and toughness of nanorods and nanotubes."Science 277, no. 5334 (1997): 1971-1975.

[39] Wilson, Neil R., David H. Cobden, and Julie V. Macpherson. "Single-wall carbon nanotube conducting probe tips." The Journal of Physical Chemistry B106, no. 51 (2002): 13102-13105.

[40] Kim, Young Lae, Bo Li, Xiaohong An, Myung Gwan Hahm, Li Chen, Morris Washington, P. M. Ajayan et al. "Highly aligned scalable platinum-decorated single-wall carbon nanotube arrays for nanoscale electrical interconnects." Acs Nano 3, no. 9 (2009): 2818-2826.

[41] Sinha, Niraj, Jiazhi Ma, and John TW Yeow. "Carbon nanotube-based sensors."Journal of nanoscience and nanotechnology 6, no. 3 (2006): 573-590.

[42] Claussen, Jonathan C., Aaron D. Franklin, Aeraj ul Haque, D. Marshall Porterfield, and Timothy S. Fisher. "Electrochemical biosensor of nanocube-augmented carbon nanotube networks." Acs Nano 3, no. 1 (2009): 37-44.

[43] Kong, Jing, Nathan R. Franklin, Chongwu Zhou, Michael G. Chapline, Shu Peng, Kyeongjae Cho, and Hongjie Dai. "Nanotube molecular wires as chemical sensors." science 287, no. 5453 (2000): 622-625.

[44] Roschier, Leif, Jari Penttilä, Michel Martin, Pertti Hakonen, Mikko Paalanen, Unto Tapper, Esko I. Kauppinen, Catherine Journet, and Patrick Bernier. "Single-electron transistor made of multiwalled carbon nanotube using scanning probe manipulation." Applied physics letters 75, no. 5 (1999): 728.

[45] Lambin, Ph, A. Fonseca, J. P. Vigneron, J. B. Nagy, and A. A. Lucas. "Structural and electronic properties of bent carbon nanotubes." Chemical Physics Letters 245, no. 1 (1995): 85-89.

[46] Ahn, Y. H., A. W. Tsen, Bio Kim, Yung Woo Park, and Jiwoong Park. "Photocurrent imaging of pn junctions in ambipolar carbon nanotube transistors." Nano letters 7, no. 11 (2007): 3320-3323.

[47] Gooding, J. Justin. "Nanostructuring electrodes with carbon nanotubes: A review on electrochemistry and applications for sensing." Electrochimica Acta50, no. 15 (2005): 3049-3060.

[48] Britto, P. J., K. S. V. Santhanam, and P. M. Ajayan. "Carbon nanotube electrode for oxidation of dopamine." Bioelectrochemistry and Bioenergetics 41, no. 1 (1996): 121-125.

[49] Wang, Jianxiu, Meixian Li, Zujin Shi, Nanqiang Li, and Zhennan Gu. "Electrocatalytic oxidation of norepinephrine at a glassy carbon electrode modified with single wall carbon nanotubes." Electroanalysis 14, no. 3 (2002): 225-230.

[50] Nguyen, Cattien V., Lance Delzeit, Alan M. Cassell, Jun Li, Jie Han, and M. Meyyappan. "Preparation of nucleic acid functionalized carbon nanotube arrays." nano Letters 2, no. 10 (2002): 1079-1081.

[51] Valentini, Federica, Aziz Amine, Silvia Orlanducci, Maria Letizia Terranova, and Giuseppe Palleschi. "Carbon nanotube purification: preparation and characterization of carbon nanotube paste electrodes." Analytical chemistry 75, no. 20 (2003): 5413-5421.

[52] Král, Petr, and Moshe Shapiro. "Nanotube electron drag in flowing liquids." Physical review letters 86, no. 1 (2001): 131.

[53] Ghosh, Shankar, A. K. Sood, and N. Kumar. "Carbon nanotube flow sensors."Science 299, no. 5609 (2003): 1042-1044.

[54] Engel, Jonathan M., Jack Chen, Chang Liu, and David Bullen. "Polyurethane rubber all-polymer artificial hair cell sensor." Microelectromechanical Systems, Journal of 15, no. 4 (2006): 729-736.

[55] Ozaki, Yoshihiro, Tomoyuki Ohyama, Takashi Yasuda, and Isao Shimoyama. "An air flow sensor modeled on wind receptor hairs of insects." In Micro Electro Mechanical Systems, 2000. MEMS 2000. The Thirteenth Annual International Conference on, pp. 531-536. IEEE, 2000.

[56] Peleshanko, Sergiy, Michael D. Julian, Maryna Ornatska, Michael E. McConney, Melbourne C. LeMieux, Nannan Chen, Craig Tucker et al. "Hydrogel-Encapsulated Microfabricated Haircells Mimicking Fish Cupula Neuromast." Advanced materials 19, no. 19 (2007): 2903-2909.

[57] Kim, Chi Yeon, Hyun Sup Lee, Yo Han Cho, Cheeyoung Joh, Pyung Choi, and Seong Jin Park. "Fabrication and characterization of artificial hair cell sensor based on MWCNT-PDMS composite." In SPIE Microtechnologies, pp. 80662F-80662F. International Society for Optics and Photonics, 2011

[58] Maschmann, Matthew R., Ben Dickinson, Gregory J. Ehlert, and Jeffery W. Baur. "Force sensitive carbon nanotube arrays for biologically inspired airflow sensing." Smart Materials and Structures 21, no. 9 (2012): 094024.

[59]Yamada, Takeo, Yuhei Hayamizu, Yuki Yamamoto, Yoshiki Yomogida, Ali Izadi-Najafabadi, Don N. Futaba, and Kenji Hata. "A stretchable carbon nanotube strain sensor for human-motion detection." Nature nanotechnology 6, no. 5 (2011): 296-301.

[60]Kaempgen, Martti, and Siegmar Roth. "Transparent and flexible carbon nanotube/polyaniline pH sensors." Journal of Electroanalytical Chemistry 586, no. 1 (2006): 72-76.

[61]Cheng, Jipeng, Xiaobin Zhang, Zhiqiang Luo, Fu Liu, Ying Ye, Wanzhong Yin, Wei Liu, and Yuexin Han. "Carbon nanotube synthesis and parametric study using CaCO 3 nanocrystals as catalyst support by CVD." Materials chemistry and physics 95, no. 1 (2006): 5-11.

[62]Hernadi, K., Z. Konya, A. Siska, J. Kiss, A. Oszko, J. B. Nagy, and I. Kiricsi. "On the role of catalyst, catalyst support and their interaction in synthesis of carbon nanotubes by CCVD." Materials chemistry and physics 77, no. 2 (2003): 536-541.

[63] Soneda, Yasushi, Laurent Duclaux, and François Béguin. "Synthesis of high quality multi-walled carbon nanotubes from the decomposition of acetylene on iron-group metal catalysts supported on MgO." Carbon 40, no. 6 (2002): 965-969.

[64] Colomer, J-F., C. Stephan, Serge Lefrant, Gustaaf Van Tendeloo, Isabelle Willems, Z. Konya, Antonio Fonseca, Ch Laurent, and Janos B. Nagy. "Large-scale synthesis of single-wall carbon nanotubes by catalytic chemical vapor deposition (CCVD) method." Chemical Physics Letters 317, no. 1 (2000): 83-89.

[65] Hernadi, K., Z. Konya, A. Siska, J. Kiss, A. Oszko, J. B. Nagy, and I. Kiricsi. "On the role of catalyst, catalyst support and their interaction in synthesis of carbon nanotubes by CCVD." Materials chemistry and physics 77, no. 2 (2003): 536-541.

[66] Lyu, S. C., B. C. Liu, T. J. Lee, Z. Y. Liu, C. W. Yang, C. Y. Park, and C. J. Lee. "Synthesis of high-quality single-walled carbon nanotubes by catalytic decomposition of C 2 H 2." Chemical Communications 6 (2003): 734-735.

[67] Klionsky, Daniel J., Fabio C. Abdalla, Hagai Abeliovich, Robert T. Abraham, Abraham Acevedo-Arozena, Khosrow Adeli, Lotta Agholme et al. "Guidelines for the use and interpretation of assays for monitoring autophagy." Autophagy8, no. 4 (2012): 445-544.

[68] Hernadi, K., A. Fonseca, J. B. Nagy, D. Bernaerts, and A. A. Lucas. "Fe-catalyzed carbon nanotube formation." Carbon 34, no. 10 (1996): 1249-1257.

[69] Yang, Y., Z. Hu, Y. N. Lü, and Y. Chen. "Growth of carbon nanotubes with metal-loading mesoporous molecular sieves catalysts." Materials chemistry and physics 82, no. 2 (2003): 440-443.

[70] Cheng, J. P., X. B. Zhang, Y. Ye, J. P. Tu, F. Liu, X. Y. Tao, H. J. Geise, and G. Van Tendeloo. "Production of carbon nanotubes with marine manganese nodule as a versatile catalyst." Microporous and mesoporous materials 81, no. 1 (2005): 73-78.

[71] An, Lei, Jessica M. Owens, Laurie E. McNeil, and Jie Liu. "Synthesis of nearly uniform single-walled carbon nanotubes using identical metal-containing molecular nanoclusters as catalysts." Journal of the American Chemical Society 124, no. 46 (2002): 13688-13689.

[72] Hernadi, K., Z. Konya, A. Siska, J. Kiss, A. Oszko, J. B. Nagy, and I. Kiricsi. "On the role of catalyst, catalyst support and their interaction in synthesis of carbon nanotubes by CCVD." Materials chemistry and physics 77, no. 2 (2003): 536-541.

[73]Cheng, Jipeng, Xiaobin Zhang, Zhiqiang Luo, Fu Liu, Ying Ye, Wanzhong Yin, Wei Liu, and Yuexin Han. "Carbon nanotube synthesis and parametric study using CaCO 3 nanocrystals as catalyst support by CVD." Materials chemistry and physics 95, no. 1 (2006): 5-11.

[74] Fan, Shoushan, Michael G. Chapline, Nathan R. Franklin, Thomas W. Tombler, Alan M. Cassell, and Hongjie Dai. "Self-oriented regular arrays of carbon nanotubes and their field emission properties." Science 283, no. 5401 (1999): 512-514.

[75]Cassell, Alan M., Jeffrey A. Raymakers, Jing Kong, and Hongjie Dai. "Large scale CVD synthesis of single-walled carbon nanotubes." The Journal of Physical Chemistry B 103, no. 31 (1999): 6484-6492.

[76] He, Delong, Michael Bozlar, Maxime Genestoux, and Jinbo Bai. "Diameter-and length-dependent self-organizations of multi-walled carbon nanotubes on spherical alumina microparticles." *Carbon* 48, no. 4 (2010): 1159-1170.

[77] Maschmann, Matthew R., Placidus B. Amama, Amit Goyal, Zafar Iqbal, Roy Gat, and Timothy S. Fisher. "Parametric study of synthesis conditions in plasma-enhanced CVD of high-quality single-walled carbon nanotubes." *Carbon*44, no. 1 (2006): 10-18.

[78] Cheng, H. M., Feng Li, Ge Su, H. Y. Pan, L. L. He, X. Sun, and M. S. Dresselhaus. "Large-scale and low-cost synthesis of single-walled carbon nanotubes by the catalytic pyrolysis of hydrocarbons." *Applied Physics Letters*72, no. 25 (1998): 3282-3284.

[79] http://en.wikipedia.org/wiki/Xylene

[80] http://en.wikipedia.org/wiki/Ferrocene

[81] http://www.emc.missouri.edu/F30.html

[82] McKee, Gregg SB, and Kenneth S. Vecchio. "Thermogravimetric analysis of synthesis variation effects on CVD generated multiwalled carbon nanotubes."*The Journal of Physical Chemistry B* 110, no. 3 (2006): 1179-1186.

[83] Costa, S., E. Borowiak-Palen, M. Kruszynska, A. Bachmatiuk, and R. J. Kalenczuk. "Characterization of carbon nanotubes by Raman spectroscopy."*Mater Sci-Poland* 26, no. 2 (2008): 433-441.

[84] Wang, Yan, Daniel C. Alsmeyer, and Richard L. McCreery. "Raman spectroscopy of carbon materials: structural basis of observed spectra."*Chemistry of Materials* 2, no. 5 (1990): 557-563.

[85] Ferrari, A. C., and J. Robertson. "Resonant Raman spectroscopy of disordered, amorphous, and diamondlike carbon." *Physical Review B* 64, no. 7 (2001): 075414.

[86] Ferrari, Andrea Carlo. "Determination of bonding in diamond-like carbon by Raman spectroscopy." *Diamond and Related Materials* 11, no. 3 (2002): 1053-1061.

[87] [c] Jorio, A., M. A. Pimenta, A. G. Souza Filho, R. Saito, G. Dresselhaus, and M. S. Dresselhaus. "Characterizing carbon nanotube samples with resonance Raman scattering." *New Journal of Physics* 5, no. 1 (2003): 139.

[88] Ferrari, A. C., J. C. Meyer, V. Scardaci, C. Casiraghi, Michele Lazzeri, Francesco Mauri, S. Piscanec et al. "Raman spectrum of graphene and graphene layers." *Physical review letters* 97, no. 18 (2006): 187401.

[89] Argento, C., and R. H. French. "Parametric tip model and force–distance relation for Hamaker constant determination from atomic force microscopy."*Journal of Applied Physics* 80, no. 11 (1996): 6081-6090.

[90] Hou P, Liu C, Tong Y, Xu S, Liu M, Cheng H. Purification of single-walled carbon nanotubes synthesized by the hydrogen arc-discharge method. J Mater Res 2001;16:2526–9.

[91] Rinzler AG, Liu J, Dai H, Nikolaev P, Huffman CB, Macias FJR, et al. Large-scale purification of single-wall carbon nanotubes: process, product, and characterization. Appl Phys A 1998;67:29–37.

[92] Jorio, A., M. A. Pimenta, A. G. Souza Filho, R. Saito, G. Dresselhaus, and M. S. Dresselhaus. "Characterizing carbon nanotube samples with resonance Raman scattering." *New Journal of Physics* 5, no. 1 (2003): 139.

[93] Kong, Jing, Nathan R. Franklin, Chongwu Zhou, Michael G. Chapline, Shu Peng, Kyeongjae Cho, and Hongjie Dai. "Nanotube molecular wires as chemical sensors." *science* 287, no. 5453 (2000): 622-625.

[94] Tahhan, May, Van-Tan Truong, Geoffrey M. Spinks, and Gordon G. Wallace. "Carbon nanotube and polyaniline composite actuators*." *Smart materials and structures* 12, no. 4 (2003): 626.

[95] Wood, Jonathan R., Qing Zhao, Mark D. Frogley, Erwin R. Meurs, Andrew D. Prins, Ton Peijs, David J. Dunstan, and H. Daniel Wagner. "Carbon nanotubes: from molecular to macroscopic sensors." *Physical Review B* 62, no. 11 (2000): 7571.

[96] Kang, Inpil, Mark J. Schulz, Jay H. Kim, Vesselin Shanov, and Donglu Shi. "A carbon nanotube strain sensor for structural health monitoring." *Smart materials and structures* 15, no. 3 (2006): 737.

[97]Yamada, Takeo, Yuhei Hayamizu, Yuki Yamamoto, Yoshiki Yomogida, Ali Izadi-Najafabadi, Don N. Futaba, and Kenji Hata. "A stretchable carbon nanotube strain sensor for human-motion detection." *Nature nanotechnology* 6, no. 5 (2011): 296-301.

[98] Simmons, John G. "Generalized formula for the electric tunnel effect between similar electrodes separated by a thin insulating film." *Journal of Applied Physics* 34, no. 6 (1963): 1793-1803.

[99] Sheng, Ping, E. K. Sichel, and J. I. Gittleman. "Fluctuation-induced tunneling conduction in carbon-polyvinylchloride composites." *Physical Review Letters* 40, no. 18 (1978): 1197.

[100] Banta, Edward R., Mary C. Hill, and Michael G. McDonald. *MODFLOW-2000, the US Geological Survey modular ground-water model: User guide to modularization concepts and the ground-water flow process*. Reston, VA: US Geological Survey, 2000.

[101] Hill, G. A., M. E. Tomusiak, B. Quail, and K. M. Van Cleave. "Bioreactor design effects on biodegradation capabilities of VOCs in wastewater." *Environmental progress* 10, no. 2 (1991): 147-153.

[102] Upadhyayula, Venkata KK, Jayesh P. Ruparelia, and Abinash Agrawal. "Use of carbon nanotubes in water treatment." *Nanoscale Multifunctional Materials: Science and Applications* (2011): 321-68.

[103] De Volder, Michael FL, Sameh H. Tawfick, Ray H. Baughman, and A. John Hart. "Carbon nanotubes: present and future commercial applications." *Science*339, no. 6119 (2013): 535-539.

[104] Gui, Xuchun, Anyuan Cao, Jinquan Wei, Hongbian Li, Yi Jia, Zhen Li, Lili Fan, Kunlin Wang, Hongwei Zhu, and Dehai Wu. "Soft, highly conductive nanotube sponges and composites with controlled compressibility." ACS nano 4, no. 4 (2010): 2320-2326.

[105] Camilli, L., C. Pisani, E. Gautron, M. Scarselli, P. Castrucci, F. D'Orazio, M. Passacantando, D. Moscone, and M. De Crescenzi. "A three-dimensional carbon nanotube network for water treatment." *Nanotechnology* 25, no. 6 (2014): 065701.

[106] Islam, M. F., D. E. Milkie, O. N. Torrens, A. G. Yodh, and J. M. Kikkawa. "Magnetic heterogeneity and alignment of single wall carbon nanotubes."*Physical Review B* 71, no. 20 (2005): 201401.